THE UNIVERSITY OF QUEENSLAND

AUSTRALIA

Biomass-Derived Carbon Materials as Anodes for Rechargeable Batteries

Rohit Ranganathan Gaddam

Master of Technology

A thesis submitted for the degree of Doctor of Philosophy at

The University of Queensland in 2018

School of Chemical Engineering

Abstract

Lithium-ion batteries (LIBs) power most of the portable electronic devices nowadays. However, the geographically limited lithium resources have led to the rapid rise of the battery price. Therefore, new battery technologies that do not rely on lithium must be developed.

Sodium-ion batteries (NIBs) are one of the promising alternatives that can replace LIBs, because of not only the abundance of sodium resources but also the significantly lower cost of sodium than lithium. To develop the NIB technology, it is imperative to find a suitable anode material that can reversibly interact with sodium ions. Amongst the available anode materials reported in the literature, carbonaceous materials are promising. While graphite has been successfully used as the anode for LIBs, it shows very poor performance for NIBs owing to the larger ionic radius of sodium than lithium, making the former difficult to intercalate into graphite. Therefore, carbon materials with an enlarged interplanar separation that can accommodate larger sodium ions would make it a suitable candidate as anodes for NIBs. Hard carbon materials derived from biomass have been shown to hold a great promise for NIBs in this regard. Biomass is a widely available resource, especially in Australia. Utilising such naturally abundant biomass precursors for producing carbon material lowers the reliance on non-renewable fossil fuel resources, thus making material production sustainable and economic. In addition, such hard carbons derived from biomass have larger interlayer spacing and defects which allow efficient sodium-ion storage. Therefore, this PhD project aims to develop such biomass-based hard carbon anode materials for NIBs.

Research results collected in this thesis project have shown that biomass-derived carbon materials display promising electrochemical properties in both LIB and NIB cells. It was found in this project that flame deposited carbon nanoparticles from coconut oil exhibited a second-cycle discharge capacity of about 277 mA h g^{-1} in NIBs and of about 741 mA h g^{-1} in LIBs at a current density of 100 mA g^{-1}. Good cycling stability, rate performance, and high coulombic efficiency are the key properties of the carbon nanoparticles. In another work, binder-free carbon electrodes with a three-dimensional architecture prepared by using a one-step fabrication protocol delivered a specific discharge capacity of 764 mA h g^{-1} at a current density of 50 mA g^{-1} with an exceptional cycling stability in a LIB cell. In a NIB cell, the electrode exhibited a discharge capacity of 241 mA h g^{-1} in the second cycle at a current density of 50 mA g^{-1} and remained stable over prolonged cycling.

Further, the focus of the thesis was laid on improving the performance of such carbon materials for NIBs. Spinifex nanocellulose derived hard carbons were prepared and used as anodes for NIBs. This carbon produced by using a low-temperature carbonization protocol delivered a superior performance as an anode for NIBs with a specific capacity of 386 mA h g^{-1} at 20 mA g^{-1} on par with graphite-based anodes for LIBs. To further enhance the performance of such carbon anodes for NIBs, a raw mango powder derived carbon material enriched with nitrogen-containing functional groups was developed for NIBs. A reversible specific capacity of ~520 mA h g^{-1} at a current density of 20 mA g^{-1} along with an excellent rate performance were obtained. When cycled at a high current density of 1 A g^{-1}, the nitrogen-rich carbon was stable for over 1000 cycles delivering a capacity of ~204 mA h g^{-1}. In all, the thesis brings out the importance of biomass-derived carbons for rechargeable batteries and puts forth synthesis and optimisation strategies for improving the electrochemical properties of such carbons for NIBs.

In summary, this thesis successfully demonstrates different synthesis strategies to prepare biomass derived hard carbon materials as anodes for rechargeable batteries. Such carbon materials produced from biomass are cost-effective and sustainable. Novel strategies like flame-deposition methods have been implemented in the present thesis project to prepare carbon nanoparticles with superior electrochemical performance in LIBs and NIBs. In addition, a scalable carbon production from native Australian biomass spinifex was demonstrated as superior anodes for NIBs. The microstructure of hard carbons reported in the thesis revealed that larger interlayer spacing and defects enhance the sodium-ion storage. Strategies to further improve the performance of such carbon materials by introducing heteroatoms like nitrogen was successfully demonstrated in the thesis. The works presented in the thesis could inspire future research in exploring such hard carbon material with tunable surface chemistries for sodium-ion storage.

Declaration by author

This thesis *is composed of my original work, and contains* no material previously published or written by another person except where due reference has been made in the text. I have clearly stated the contribution by others to jointly-authored works that I have included in my thesis.

I have clearly stated the contribution of others to my thesis as a whole, including statistical assistance, survey design, data analysis, significant technical procedures, professional editorial advice, financial support and any other original research work used or reported in my thesis. The content of my thesis is the result of work I have carried out since the commencement of my higher degree by research candidature and does not include a substantial part of work that has been submitted *to qualify for the award of any* other degree or diploma in any university or other tertiary institution. I have clearly stated which parts of my thesis, if any, have been submitted to qualify for another award.

I acknowledge that an electronic copy of my thesis must be lodged with the University Library and, subject to the policy and procedures of The University of Queensland, the thesis be made available for research and study in accordance with the Copyright Act 1968 unless a period of embargo has been approved by the Dean of the Graduate School.

I acknowledge that copyright of all material contained in my thesis resides with the copyright holder(s) of that material. Where appropriate I have obtained copyright permission from the copyright holder to reproduce material in this thesis and have sought permission from co-authors for any jointly authored works included in the thesis.

Publications included in this thesis

1. **Rohit Ranganathan Gaddam**, Nanjundan Ashok Kumar, Ramanuj Narayan, KVSN Raju and X S Zhao, book chapter titled **'**Advanced carbon materials for electrochemical energy storage' for a book on 'Nanomaterials Synthesis: Design, Fabrication and Applications'**,** *Elsevier*, 2018 (**In press)**. (Included in chapter 1 and chapter 2)

Contributor	Statement of Contribution
Rohit Ranganathan Gaddam	Wrote and edited the chapter (80 %)
Nanjundan Ashok Kumar	Edited the chapter (5%)
Ramanuj Narayan	Edited the chapter (5%)
KVSN Raju	Edited the chapter (5%)
X.S. Zhao	Edited the chapter (5%)

2. **Rohit Ranganathan Gaddam**, Dongfang Yang, Ramanuj Narayan, KVSN Raju, Nanjundan Ashok Kumar and X.S. Zhao, Biomass Derived Carbon Nanoparticle as anodes for High Performance Sodium and Lithium Ion Batteries, *Nano-Energy*, 2016, 26, 346-352. (Included as chapter 4)

Contributor	Statement of Contribution
Rohit Ranganathan Gaddam	Designed the experiments (90%) Wrote and edited the paper (80%)
Dongfang Yang	Material characterization (20%)
Ramanuj Narayan	Wrote and edited the paper (5%)
KVSN Raju	Wrote and edited the paper (5%)
Nanjundan Ashok Kumar	Wrote and edited the paper (5%) Designed experiments (5%)
X.S. Zhao	Wrote and edited the paper (5%) Designed experiments (5%)

3. **Rohit Ranganathan Gaddam**, Nanjundan Ashok Kumar and X.S. Zhao, Carbon nanoparticle-based three-dimensional binder-free anode for rechargeable alkali-ion batteries, *Materials Today Energy*, 2018, 8, 29-36. (Included as chapter 5)

Contributor	Statement of Contribution
Rohit Ranganathan Gaddam	Designed the experiments (90 %) Wrote and edited the paper (80 %)
Nanjundan Ashok Kumar	Wrote and edited paper (10 %) Designed the experiments (5 %)
X.S. Zhao	Wrote and edited the paper (10 %) Designed the experiments (5 %)

4. **Rohit Ranganathan Gaddam**, Edward Jiang, Nasim Amiralian, Pratheep K. Annamalai, Darren Martin, Nanjundan Ashok Kumar and X. S. Zhao, Spinifex Nanocellulose Derived Hard Carbon as Anodes for High-Performance Sodium-Ion Batteries, *Sustainable Energy and Fuels*, 2017,1, 1090-1097. (Listed in the 2017 Sustainable Energy and Fuels HOT Articles) (Included as chapter 6)

Contributor	Statement of Contribution
Rohit Ranganathan Gaddam	Designed the experiments (80%) Wrote the paper (70%)
Edward Jiang	Designed the experiments (10%) Wrote the paper (5%)
Nasim Amiralian	Wrote and edited the paper (5%)
Pratheep K. Annamalai	Wrote and edited the paper (5%)
Darren Martin	Wrote and edited the paper (5%)
Nanjundan Ashok Kumar	Wrote and edited the paper (5%) Designed experiments (5%)
X.S. Zhao	Wrote and edited the paper (5%) Designed experiments (5%)

5. **<u>Rohit Ranganathan Gaddam</u>**, A. H. F. Niaei, Marlies Henkel, Debra Searles, Nanjundan Ashok Kumar and X.S. Zhao, Capacitance enhanced sodium-ion storage in nitrogen-rich hard carbons, *Journal of Materials Chemistry A*, 2017, 5, 22186-22192 (Included as chapter 7)

Contributor	Statement of Contribution
Rohit Ranganathan Gaddam	Designed the experiments (90%) Wrote the paper (75%)
A. H. F. Niaei	Density functional theory calculation (80%) Wrote the paper (5%)
Marlies Henkel	Density functional theory calculation (10%) Wrote the paper (5%)
Debra Searles	Density functional theory calculation (10%) Wrote the paper (5%)
Nanjundan Ashok Kumar	Edited the paper (15%) Designed experiments (5%)
X.S. Zhao	Wrote and edited the paper (15%) Designed experiments (5%)

Submitted manuscripts included in this thesis

"No manuscripts submitted for publication".

Other publications during candidature

1. X Sun, H Lu, Peng Liu, T E Rufford, **Rohit Ranganathan Gaddam**; X Fan and X S Zhao
   A reduced graphene oxide-NiO composite electrode with a high and stable capacitance, *Sustainable Energy and Fuels*, 2017, 2, 7673-678

2. D Yang, X Sun, K Lim, **Rohit Ranganathan Gaddam**, NA Kumar, K Kang, XS Zhao
   Pre-sodiated nickel cobaltite for high-performance sodium-ion capacitors, *Journal of Power Sources*, 2017, 362, 358-365.

3. H Lu, X Sun, **Rohit Ranganathan Gaddam**, N A Kumar and X.S. Zhao
   Electrocapacitive properties of nitrogen-containing porous carbon derived from cellulose, *Journal of Power Sources*, 2017, 360, 634-641.

4. Xin Fan, **Rohit Ranganathan Gaddam**, Nanjundan Ashok Kumar and X.S. Zhao
   A Hybrid Mg^{2+}/Li^{+} Battery Based on Interlayer-Expanded MoS_2/Graphene Cathode, *Advanced Energy Materials*, 2017 (DOI: 10.1002/aenm.201700317).

5. Nanjundan Ashok Kumar, **Rohit Ranganathan Gaddam**, Moorthy Suresh, Srinivasa Rao Varanasi, Suresh Kumar Bhatia and X S Zhao
   Porphyrin-based Graphene Oxide Frameworks for Long Life Sodium Ion Batteries, *Journal of Materials Chemistry A*, 2017, 5, 13204-13211.

6. NA Kumar, † **Rohit Ranganathan Gaddam**, † SR Varanasi, Dongfang Yang, SK Bhatia and X.S. Zhao
   Sodium ion storage in reduced graphene oxide, *Electrochimica Acta*, 2016, 214, 319-325. († equally contributing first authors)

7. Wu, Yilan, Xin Fan, **Rohit Ranaganathan Gaddam**, Qinglan Zhao, Dongfang Yang, Xiaoming Sun, Chao Wang, and X. S. Zhao.
   Mesoporous niobium pentoxide/carbon composite electrodes for sodium-ion capacitors, *Journal of Power Sources*, 2018, 408, 82-90.

Conference proceedings

1. **Rohit Ranganathan Gaddam**, Nanjundan Ashok Kumar and X.S. Zhao
   Hard carbon-based anodes for sodium-ion storage at the Asia Pacific-Energy Storage and Conversion conference-2018 held at Nanyang Technological University from July 18-20th, 2018.

Contributions by others to the thesis

Prof George Zhao and Dr Ashok Kumar Nanjundan helped with the preparation of the thesis and provided suggestions on the draft.

Statement of parts of the thesis submitted to qualify for the award of another degree

"No works submitted towards another degree have been included in this thesis".

Research Involving Human or Animal Subjects

"No animal or human subjects were involved in this research".

Acknowledgements

I express my deep sense of gratitude and heartfelt thanks to my supervisors Prof George Zhao and Dr Ashok Kumar Nanjundan. I would like to thank Prof. George Zhao for his intensive suggestions, valuable guidance and vital help throughout this research. I consider it a great opportunity to do my PhD under Prof George Zhao's guidance and to learn from his research expertise. I would like to also thank my co-advisor Dr Ashok Kumar Nanjundan, for his support and advice. He teaches me how to approach difficult research topics with simple, neat ways; he creates every opportunity to help me to connect, learn, and benefit from other researchers in the field.

I would like to thank Dr KVSN Raju and Dr Ramanuj Narayan, scientists at CSIR- Indian Institute of Chemical Technology for their support. I would also like to thank Dr D Vasudevan from the Central Electrochemical Research Institute for his support. I greatly appreciate the conversations with my colleagues, Dr Peng Liu, Dr Luhong Zhang, Dr Xiaoming Sun, Ms Dongfang Yang, Mr Hao Lu, Ms Qinlan Zhao, Ms Yilan Wu, Mr Yverick Rangom and Ms Xin Fan

I would like to acknowledge the facilities, and the scientific and technical assistance, of the Australian Microscopy & Microanalysis Research Facility at the Centre for Microscopy and Microanalysis, The University of Queensland

I would like to express my sincere heartfelt gratitude to my parents, my teachers without whose help and support my continuance in education would have been difficult.

Financial support

This research was supported by the Australian Government Research Training Program Scholarship (International Postgraduate Research Scholarship and the UQ Centennial Scholarship).

This research was also supported by the Australian Research Council (ARC) under the ARC projects of DP 103101870 and LF 170110101.

Keywords

Hard carbon, rechargeable battery, biomass, sodium-ion, lithium-ion, electrochemistry, energy storage

Australian and New Zealand Standard Research Classifications (ANZSRC)

ANZSRC code: 090403, Chemical Engineering Design, 80%

ANZSRC code: 091205, Functional Materials, 20%

Fields of Research (FoR) Classification

FoR code: 0904, Chemical Engineering, 60%

FoR code: 0912, Materials Engineering, 40%

Dedicated to

H.H. SRI RANGARAMAANUJA MAHA DESIKAN

Table of Contents

List of Figures

List of Tables

List of Abbreviations

BET	Brunauer–Emmett–Teller
BJH	Barrett-Joyner-Halenda
CNP	Carbon nanoparticle
c-CNP	Carboxylated carbon nanoparticles
CNT	Carbon nanotube
CV	Cyclic Voltammetry
DC	Dimethyl carbonate
EIS	Electrochemical impedance spectroscopy
EDLC	Electrical double layer capacitor
EC	Ethylene carbonate
FESEM	Field-emission scanning electron microscope
FEC	Fluoroethylene carbonate
FTIR	Fourier transform infrared spectroscopy
GCD	Galvanostatic charge-discharge
HCS	Hard carbons
HRTEM	High-resolution transmission electron microscope
LIB	Lithium-ion battery
NIB	Sodium-ion battery
N-HCS	Nitrogen-rich hard carbons
PC	Propylene carbonate
NDC	Nanocellulose derived carbon
XRD	X ray-diffraction
XPS	X-ray photoelectron spectroscopy

Chapter 1. Introduction

1.1 Background

Energy management and climate change are one of the greatest challenges faced in the present millennia. Sustainable routes to generate energy (*via* wind, water and solar), though abundant are intermittent, which require proper storage for efficient management [1]. Hence, affordable and sustainable energy storage technologies are quintessential to cater the future societal energy needs. It is estimated that around 2 billion people in the world do not have access to electricity and might not be able to procure power supply through grids [1]. Hence, for both on-grid and off-grid electricity supply, energy storage is quite essential. It is not feasible to develop a single energy storage system to cater to today's technological needs. Therefore, the integration of various technologies like batteries, supercapacitors, magnetic and kinetic energy storage systems are being considered [1].

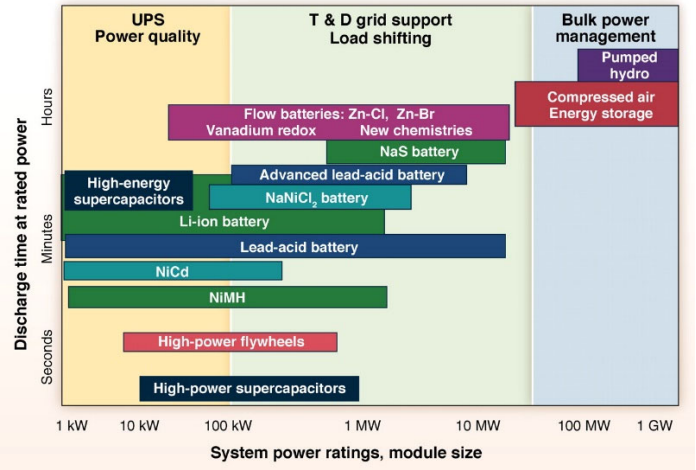

Figure 1.1 A general comparative chart of discharge time and power ratings for different energy storage technologies [2].

The energy storage technologies used in large-scale storage are subdivided into electrical, mechanical, chemical and electrochemical (**Figure 1.1**) [3]. Amongst them, electrochemical energy storage, in particular, have captured larger interests due to their low carbon footprint, high efficiency, the flexible power-energy regime for grid operations, high shelf-life and low costs associated with their upkeep. The principles of electrochemical energy storage were known much before 200 years. Such electrochemical systems convert the electrical energy into chemical energy (and vice versa) *via* redox reaction at the interface of active electrode mass and electrolyte [4]. In general, an electrochemical cell consists of a negative electrode, a positive electrode and an electrolyte (which is electronically insulating and conductive to ions).

Batteries are at the forefront of these electrochemical energy storage systems for portable electronics as well for grid-level energy storage.

Rechargeable batteries generate electricity from the chemical energy of active materials and can reversibly convert the generated electric energy into chemical energy. The most common rechargeable batteries are the lithium-ion, nickel-cadmium (Ni-Cd), nickel-metal hydride (Ni-MH) and lead-acid batteries [5]. Among them, lithium-ion batteries (LIB) is a good choice for portable electronic devices because they possess an upright balance between specific energies and power densities [6]. LIBs are also an essential energy storage device for alternative power sources, such as solar and wind. However, such large-scale application of LIBs might face certain constraints associated with the geographical limitations of lithium ore. This might increase the battery price in near future and also lead to political fluxes [6]. Sodium-ion battery (NIB) is a promising alternative to LIBs. This is because sodium has a practically unlimited reserve making it cheap to procure. Also, similarities of sodium with the lithium chemistries make it easier to build NIBs based on prior knowledge obtained on lithium-ion based battery systems (**Table 1.1**) [7].

Table 1.1 Comparison of the characteristic of lithium and sodium **[7]**

Category	Sodium	Lithium
Cation Radius (Å)	1.06	0.76
Atomic Weight	23 g mol^{-1}	6.9 g mol^{-1}
E^o (SHE)	-2.71 V	-3.04 V
Cost, carbonates	$ 150 per ton	$ 1500 per ton
Capacity (mA h g^{-1}), metal	1165	3829
Coordinate preference	Octahedral and Prismatic	Octahedral and tetrahedral

Further, improvement in the performance of NIBs largely depends on the design and development of new electrode materials. Several cathode materials have already been successfully investigated for NIBs [8]. Discovery of suitable anode materials for NIB form the bottleneck for commercialisation of NIBs. Graphite that has been successfully used as an anode material for LIBs seldom show good performance in NIBs owing to larger ionic radius of sodium (0.102 nm for sodium-ion *vs.* 0.076 nm for lithium-ion) and failure to form graphite intercalation compounds [9]. Transitional metal oxides, metal nitrides, metal sulphides and other carbonaceous materials have been investigated as anode materials for NIBs [10].

Amongst them, non-graphitic hard carbon anodes owing to their larger interlayer spacing, defective structure and turbostratic nanodomains provide a conducive environment for sodium-ion storage [9, 11]. Such hard carbon materials have good electrical conductivity, are economical to produce and easy to synthesise [12]. Hard carbons can easily be sourced from biomass which reduces the dependence on fossil fuel based precursors making its production sustainable. Such biomass-derived carbon materials have recently captured the research interest owing to its superior electrochemical performance in both LIBs and NIBs [13-17].It is to be noted that NIB is still in its infancy. Until NIBs are commercialised, it is understood that LIBs will keep playing a pivotal role in the energy storage market. Consequently, technological advancements in both LIBs and NIBs are of crucial importance.

1.2 Objectives of the present thesis

LIB has been successfully commercialised for application in portable electronics as well to power hybrid electric vehicles[6]. However, rarity of lithium resources has made researchers to look for alternative battery systems like that of NIBs, which are promising for large-scale energy storage systems. However, graphite that has been commercialised as anodes for LIBs cannot be used in NIBs due to larger ionic radius of sodium and the inability of sodium to form graphite intercalation compounds. On the other hand, biomass-derived hard carbon materials have shown promise as anodes for NIBs and also perform well in LIBs. Simple methodologies can be adapted to engineer such high-performance carbon anodes from biomass. The present thesis aims at producing such carbon materials for use as anodes in LIBs and NIBs.

The specific aims of the present thesis are:

1. To synthesize carbon materials from biomass using cost-effective and simple approaches.
2. To study the obtained material characteristics using qualitative and quantitative characterisation techniques
3. To utilise the derived carbon material as anodes for lithium and/or sodium-ion batteries.
4. To enhance the specific capacity and cycling stability of biomass-derived carbon for sodium-ion batteries.

1.3 Outline of the thesis

Chapter 1 provides a brief description of research problems and objectives. This chapter deals with the background of the thesis showcasing the importance of batteries and provides, in brief, the advantages of using NIBs. **Chapter 2** introduces various types of carbon-based materials

and also provides, in brief, the synthesis of carbon materials from biomass. The allotropes of carbons like carbon nanotubes, graphene, fullerene are discussed. Biomass-derived carbon materials and its advantages over the mentioned allotropic forms of carbon for battery application is described in brief. The working principle of LIBs and NIBs are discussed along with anode materials available for the batteries. **Chapter 3,** deals with materials and methods. The materials, precursors and characterization techniques used for the development of battery anodes are discussed. In **chapter 4,** a novel flame deposition method to prepare carbon nanoparticles from coconut oil is reported. The carbon nanoparticles were studied as potential anodes for LIBs and NIBs. Further, in **chapter 5** a simple and effective method for the fabrication of three-dimensional (3D) binder-free carbon anode using camphor as a carbon source is described. The anode, when tested against lithium and sodium, showed good electrochemical performance.

In **chapter 6,** an Australian native arid grass 'spinifex' derived carbon with superior performance as an anode for NIBs with a specific capacity of 386 mA h g^{-1} at 20 mA g^{-1} current density. **Chapter 7** deals with a raw mango powder derived carbon material enriched with nitrogen-containing functional groups as anodes for NIBs. This chapter showed that nitrogen doping enhanced the interaction of sodium ions with the carbon, leading to a significantly improved storage capacity. In **chapter 8,** conclusions drawn from the thesis and possible future directions for research are discussed.

1.3 References

[1] P.J. Hall, E.J. Bain, Energy Policy, 36 (2008) 4352-4355.

[2] A.A. Akhil, G. Huff, A.B. Currier, B.C. Kaun, D.M. Rastler, S.B. Chen, A.L. Cotter, D.T. Bradshaw, W.D. Gauntlett, DOE/EPRI 2013 electricity storage handbook in collaboration with NRECA, Sandia National Laboratories Albuquerque, NM2013.

[3] G.L. Soloveichik, Annual Review of Chemical and Biomolecular Engineering, 2 (2011) 503-527.

[4] O. Haas, E.J. Cairns, Annual Reports Section" C"(Physical Chemistry), 95 (1999) 163-198.

[5] B. Dunn, H. Kamath, J.-M. Tarascon, Science, 334 (2011) 928-935.

[6] R.R. Gaddam, D. Yang, R. Narayan, K. Raju, N.A. Kumar, X.S. Zhao, Nano Energy, 26 (2016) 346-352.

[7] M.D. Slater, D. Kim, E. Lee, C.S. Johnson, Adv. Funct. Mater., 23 (2013) 947-958.

[8] H. Hou, X. Qiu, W. Wei, Y. Zhang, X. Ji, Adv. Energy Mater., 7 (2017).

[9] Z. Zhu, F. Liang, Z. Zhou, X. Zeng, D. Wang, P. Dong, J. Zhao, S. Sun, Y. Zhang, X. Li, J. Mater. Chem. A, 6 (2018) 1513-1522.

[10] W. Wang, W. Li, S. Wang, Z. Miao, H.K. Liu, S. Chou, J. Mater. Chem. A, (2018).

[11] C. Bommier, X. Ji, Isr. J. Chem., 55 (2015) 486-507.

[12] Y. Bai, Z. Wang, C. Wu, R. Xu, F. Wu, Y. Liu, H. Li, Y. Li, J. Lu, K. Amine, ACS Appl. Mater. Inter., 7 (2015) 5598-5604.

[13] E. Frackowiak, F. Béguin, Carbon, 39 (2001) 937-950.

[14] L.L. Zhang, X.S. Zhao, Chem. Soc. Rev., 38 (2009) 2520-2531.

[15] L.L. Zhang, R. Zhou, X.S. Zhao, J. Mater. Chem., 20 (2010) 5983-5992.

[16] C. Xu, B. Xu, Y. Gu, Z. Xiong, J. Sun, X.S. Zhao, Energy Environ. Sci., 6 (2013) 1388-1414.

[17] L.L. Zhang, Y. Gu, X.S. Zhao, J. Mater. Chem. A, 1 (2013) 9395-9408.

Chapter 2. Literature review

-To be published as a book chapter by *R.R. Gaddam et al.* titled ‘Advanced carbon materials for electrochemical energy storage’, in Elsevier 2018 (In press).

2.1 Carbon materials: types and sources

Carbon has a prominent role to play in the advancement of sustainable clean energy technologies. Carbon naturally assumes various allotropic forms like graphene, fullerenes, carbon nanotubes etc. The forms of carbon depending on their degree of graphitisation can be classified into two categories: (1) 'hard carbons', that cannot be easily graphitised and contain turbostratic nanodomains and (2) an easily graphitisable 'soft carbons' (**Figure 2.1**) [1, 2]. The microstructure of carbon dictates their electrochemical performance. Therefore, precursors, synthesis strategies and surface modifications play a major role. This section describes some traditional carbon allotropes like graphene, carbon nanotubes and fullerene. In addition, hard carbons from biomass precursors have been discussed as they have gained significant research interests in recent years and utilisation of such biomass derived carbon materials for battery application is also the focus of the present thesis. Biomass-derived carbon materials are promising as a high-performance material for lithium and sodium-ion storage [3]. Even when compared with the electrochemical performance of traditional carbon allotropes, such biomass-derived carbon materials more promising for electrochemical energy storage [1].

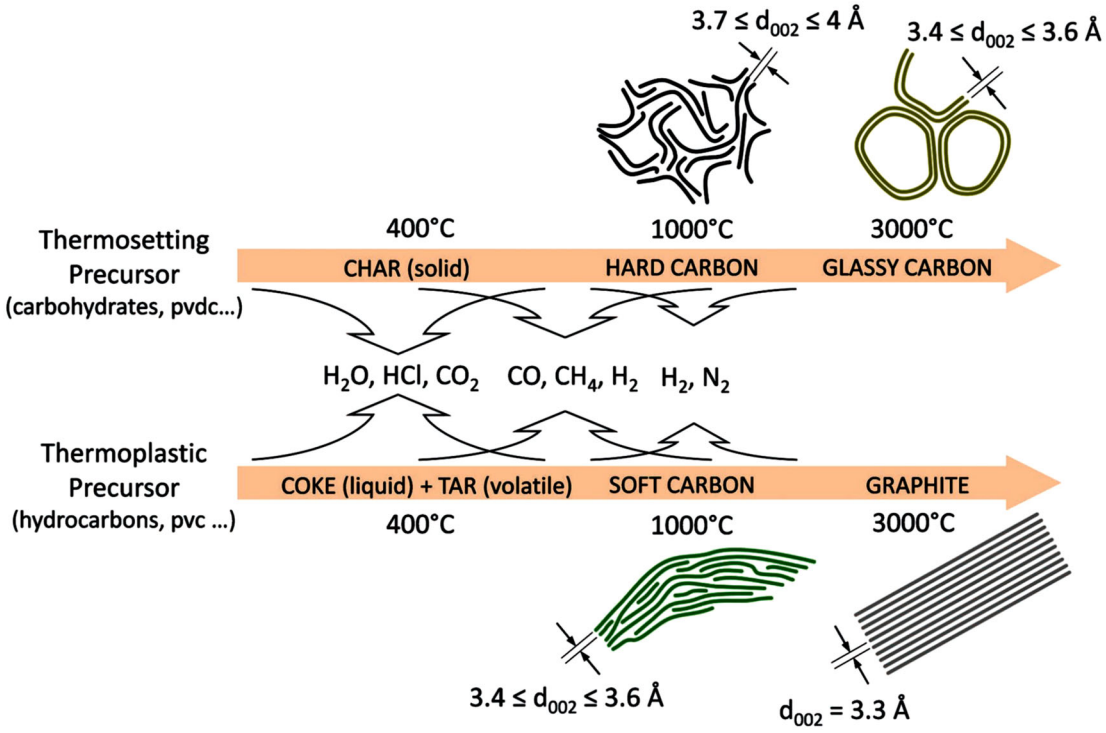

Figure 2.1 Illustration of soft carbon and hard carbon production *via* pyrolysis of thermoplastic and thermosetting precursors [1].

2.1.1 Graphene

Graphene is a monolayered carpet of sp^2 hybridised carbon network packed into a honeycomb-like lattice, that provides tremendous opportunities for surface design. It was initially thought to be non-existent until the first discovery of graphene made by mechanical peeling of graphite galleries using scotch tape till a single layer of graphite was obtained. This earned Geim and Novoselov a Nobel prize in 2004 [4]. Since then, there has been a significant amount of research interest invested in the production of graphene. The method used for producing graphene determines the properties of the final material. Generally, graphene is prepared either by top-down or bottom-up approaches (**Figure 2.2**). A bottom-up approach to graphene synthesis involves chemical vapour deposition or other chemical synthesis techniques [5]. Exfoliation of graphite using chemical, thermal and electrical methods to form a graphene-oxide is a typical top-down approach.

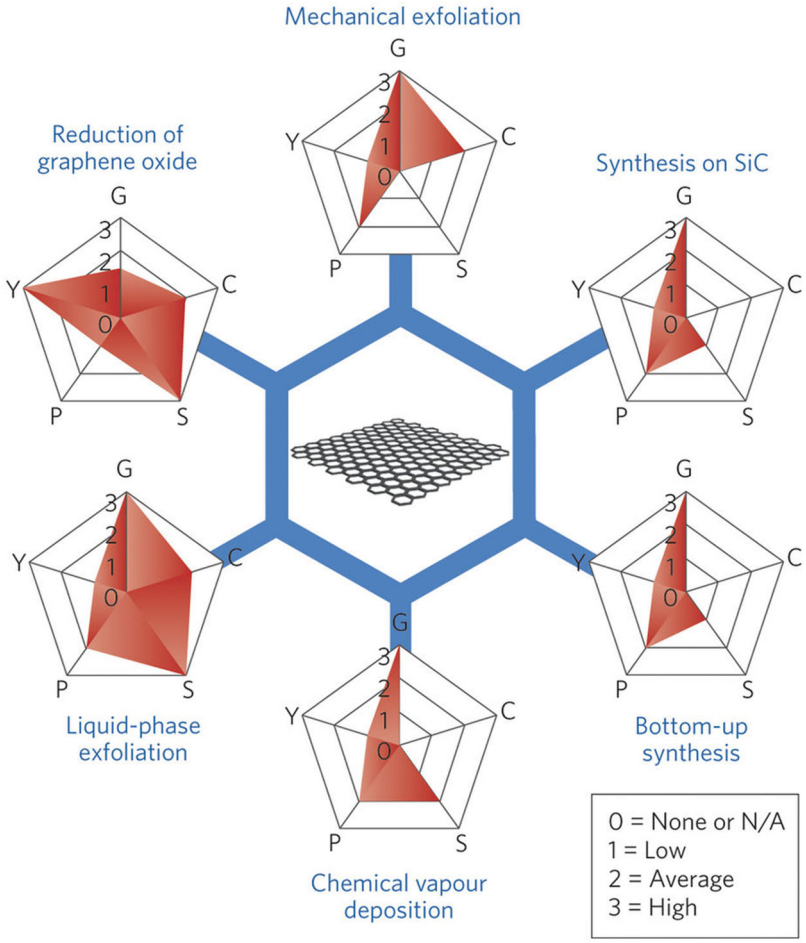

Figure 2.2 Graphene preparation methods in terms of its quality (G), cost (C), large-scale production capabilities (S), yield (Y) and purity (P) [6].

Reduction of graphene oxide and liquid-phase exfoliation are the most common methods to generate graphene in bulk. In a liquid phase exfoliation, an expanded graphite (usually by thermal means) is dispersed into a solvent. This eventually helps in the reduction of van der Waals forces between the graphene layers followed by application of an external stimulus (ultrasonication, electric field etc.) to exfoliate graphite into individual sheets [6]. However, this method leaves behind some unexfoliated graphite which needs to be isolated. Nevertheless, the ease of synthesis makes this method most suitable for the bulk production of graphene. In the other method [5], graphite is strongly oxidized to produce a highly defective graphene called the graphene oxide. Graphene oxide offers a wide variety of carbonyl and epoxy groups, which can be selectively transformed into other functionalities depending on its application. The alternation of carboxyl groups into other functionalities require activation, which can then form covalent linkages with nucleophiles. In general, carboxyl groups are transformed into amide or ester groups by reaction with an amine or hydroxyl containing nucleophiles. Similarly, alteration of GO through epoxy is believed to happen *via* a ring opening reaction [5]. Such alternations restore the π-conjugations of such reduced graphene oxide with properties similar to that of graphene. Graphene and related materials have been widely investigated for use in the state-of-art energy storage devices owing to their unique properties. They are promising to improve the energy density and power density of the existing energy storage systems.

2.1.2 Fullerene

Fullerene discovery was initially made amongst the gas phase carbon-ions produced by the laser ablation of graphite [7], and macroscopic quantities of fullerenes were obtained from graphite using the arc-discharge technique. The first fullerene discovered was buckminsterfullerene (C_{60}) in 1985 [7], which is a zero-dimensional carbon with 60 carbon atoms forming a spherical configuration (called truncated icosahedron). These carbons are made up of both pentagonal and hexagonal carbon atoms, where the pentagonal carbon atoms provide curvature to the material. Smalley et al. [8] suggested, that during C_{60} synthesis, the carbon atoms come close to each other to form a linear carbon species which would add carbon atoms until it reaches a few dozen carbons. They postulated that a more thermodynamically favourable open graphene sheet-like structure is formed as there are higher reactive sites than the cyclic or linear counterparts given their dangling bonds. These graphene sheets gather enough pentagons and finally form fullerene [8]. Several types of fullerenes can be realised

mathematically; with the increasing number of carbon atoms, the curvature is small because of a lower strain.

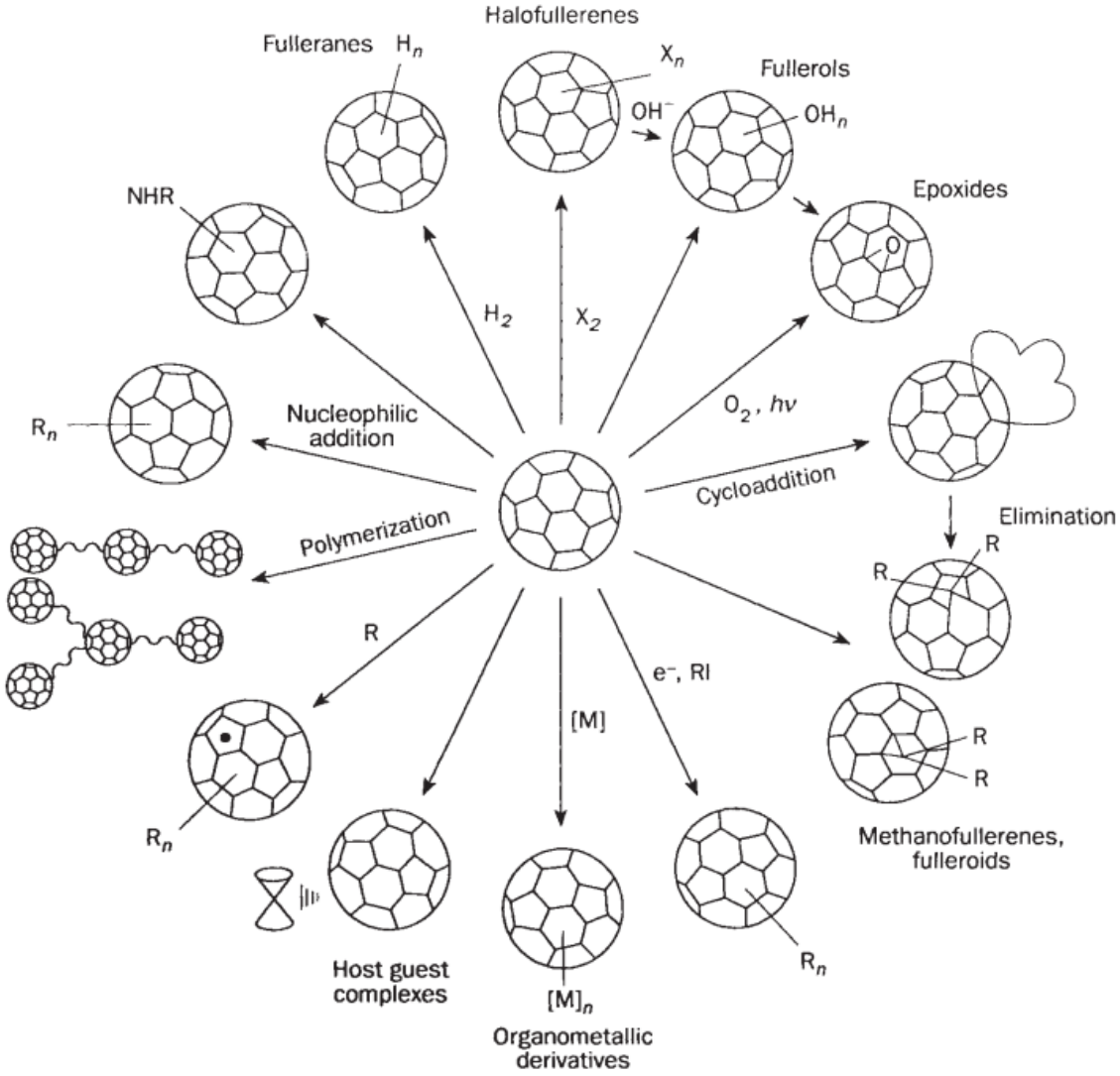

Figure 2.3 Some general reactions that occur with buckminsterfullerene [9].

The discovery of fullerene paved way for the synthesis of many advanced carbon materials like graphene and carbon nanotubes. Their unique carbon arrangement leads to good electronic conductivity, large specific surface area and superior absorption capacities. They mainly enhance the conductivity and do not provide good mechanical properties owing to their aspect ratio. Alteration of fullerene chemistry via functionalisation allows easy tuning of properties via addition, polymerisation and substitution reactions (**Figure 2.3**) [9]. The functionalised fullerene could be of two types namely (1) exohedral fullerene (where the functional moieties are attached to the exterior of the cage) and (2) endohedral fullerene (moieties is within the

cage). Another interesting arrangement of the fullerene is as a peapod, where the fullerene is encapsulated within a nanotube [10]. Modified fullerenes have been used as potential electrode materials in lithium-ion batteries (LIB) [11] and magnesium batteries [12].

2.1.3 Carbon nanotubes

Carbon nanotubes (CNT) can be visualised as the wrapping of graphene sheet into the form of a cylinder. These nanotubes are essentially made of sp^2 carbon atoms which are many times stronger than the sp^3 hybridised carbons in diamond. CNTs exhibit excellent stability against chemicals, possess a unique aspect ratio, high surface area (~1500 m^2 g^{-1}), superior tensile strength, high electrical and thermal conductivity [13]. CNTs could be metallic or semiconducting depending on their arrangement depending on how the graphene gets rolled [13]. The rolling of graphene sheet could be carried out in many ways which could break the symmetry of the graphene plane and create a distinct direction along the hexagonal lattice. For a single-walled nanotube formation (**Figure 2.4**), the rolling of the graphene sheet is carried out along a lattice vector (m, n), which dominates the chirality of nanotube. An armchair type carbon nanotube is formed when 'n' and 'm' are equal. If either 'm' or 'n' equals to zero a zigzag type nanotube is formed. When an inequality exists between 'n' and'm' a "chiral" tube formation takes place [14]. The parameters of (m, n) are quite important in determining the chirality and in turn the optical, mechanical and electronic properties of CNTs.

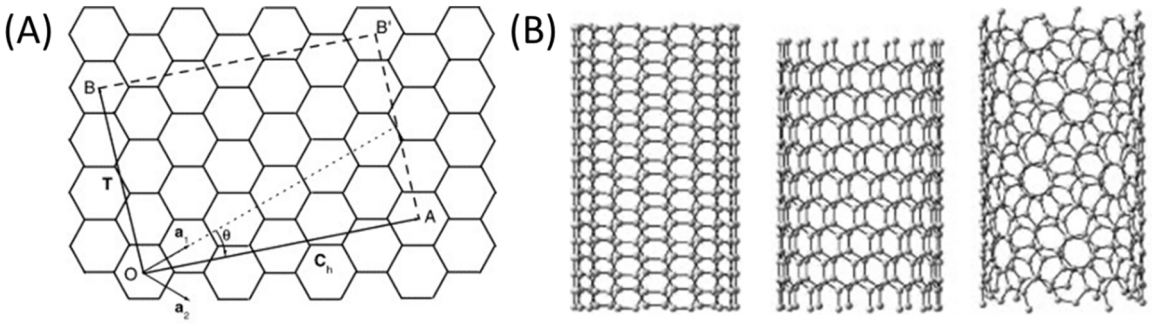

Figure 2.4 (a) Chiral vectors defining the SWNT unit cell; (b) armchair, zigzag and chiral SWNTs [15].

Ballistic transport of electrons could be observed in defect-free single-walled carbon nanotubes, where no scattering or migration of electrons could be observed. Both single-walled (SWNTs) and multiwalled carbon nanotubes (MWNTs) can be prepared by (1) laser ablation (2) arc discharge and (3) chemical vapour deposition [16]. Most of the major synthesis methods used in the preparation of SWNTs introduce some impurities that could be eradicated by treatment with acids. However, such treatments reduce the length of the nanotubes, create

imperfections and add to the cost. In addition, such synthesis methods produce a mixture of semiconductor and metallic nanotube which could be an important aspect to consider for an electronic device. Though the metallic nanotubes can be selectively removed by electrical heating, still no large-scale synthesis of ultra-high purity SWNTs exist [17].

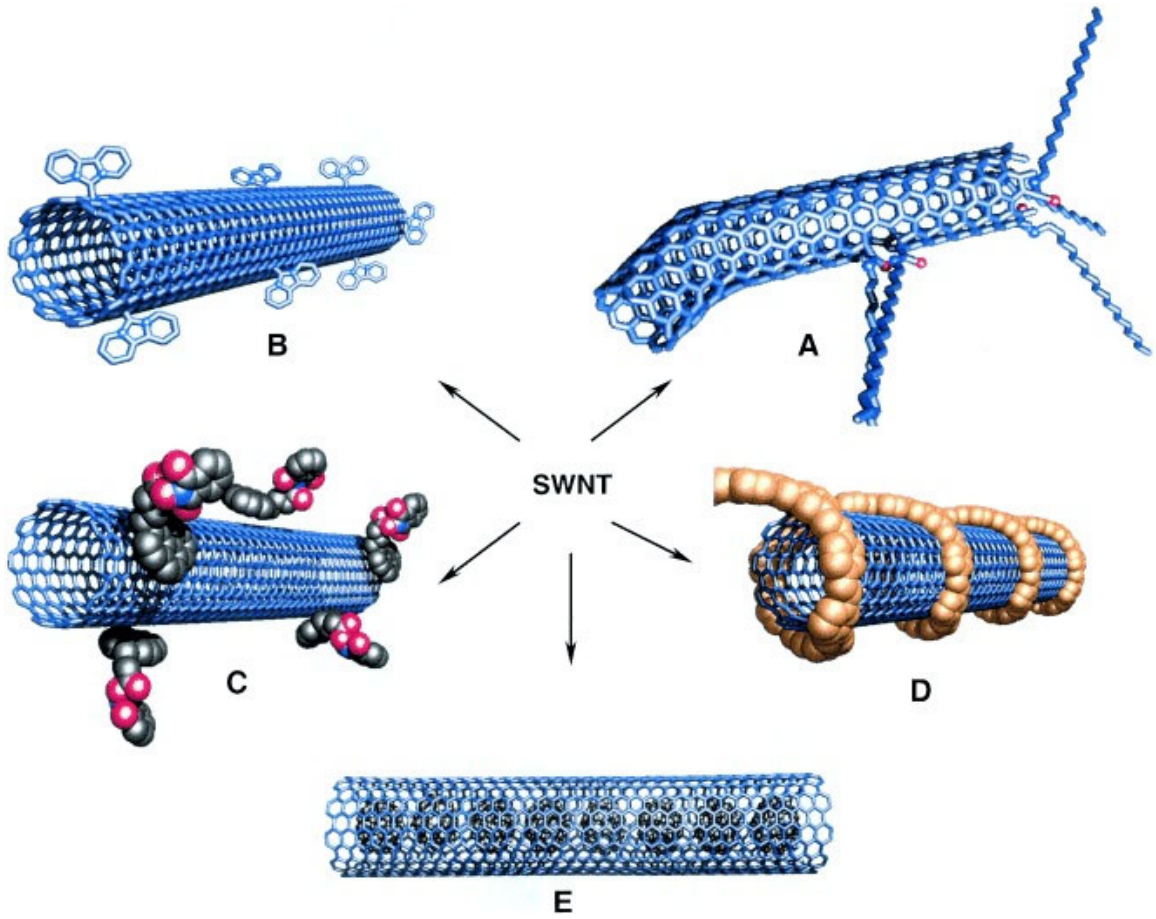

Figure 2.5 Schematic representation of CNT functionalisation. (A) Functionalization at the defect site, (B) attaching moieties onto the sidewall, (C) exohedral functionalization using surfactants, (D) attaching polymer moieties using non-covalent means, and (E) pea-pod like CNT-fullerene structure [17].

In general, CNTs find their commercial application as a composite. The low density of functional groups available on the surface makes it difficult for the CNTs to disperse in a given matrix. Therefore, functionalisation by covalent (chemical) and non-covalent (physical) means is carried out for CNTs (**Figure 2.5**). CNTs, in general, possess a high surface area of porous nanotube arrays which makes it electrochemically active for applications involving supercapacitors and batteries. CNT based supercapacitors higher power densities and storage capabilities as compared to ordinary capacitors. Even in the case of lithium-ion batteries, high discharge capacities at larger current densities were observed [16]. However certain limitations

with respect to the absence of a voltage plateau and voltage hysteresis exist which could be overcome by making composite materials. CNT based composites have found use as potential anode materials for lithium-ion batteries.

2.1.4 Biomass-derived carbon materials

Biomass has recently gained tremendous interest to produce carbon materials for energy storage applications. Several synthesis strategies have been employed for the preparation of carbon materials with tailored physicochemical properties. However, scalability issues and inherent toxicity involved in the production methods using fossil-fuel derived precursors increase their production costs. Biomass has the potential to be a sustainable source for producing several carbon allotropes (**Figure 2.6**). Precursors like carbohydrates, cellulose, protein, amino acids, *etc.*, have been widely used to synthesize carbon materials [18].

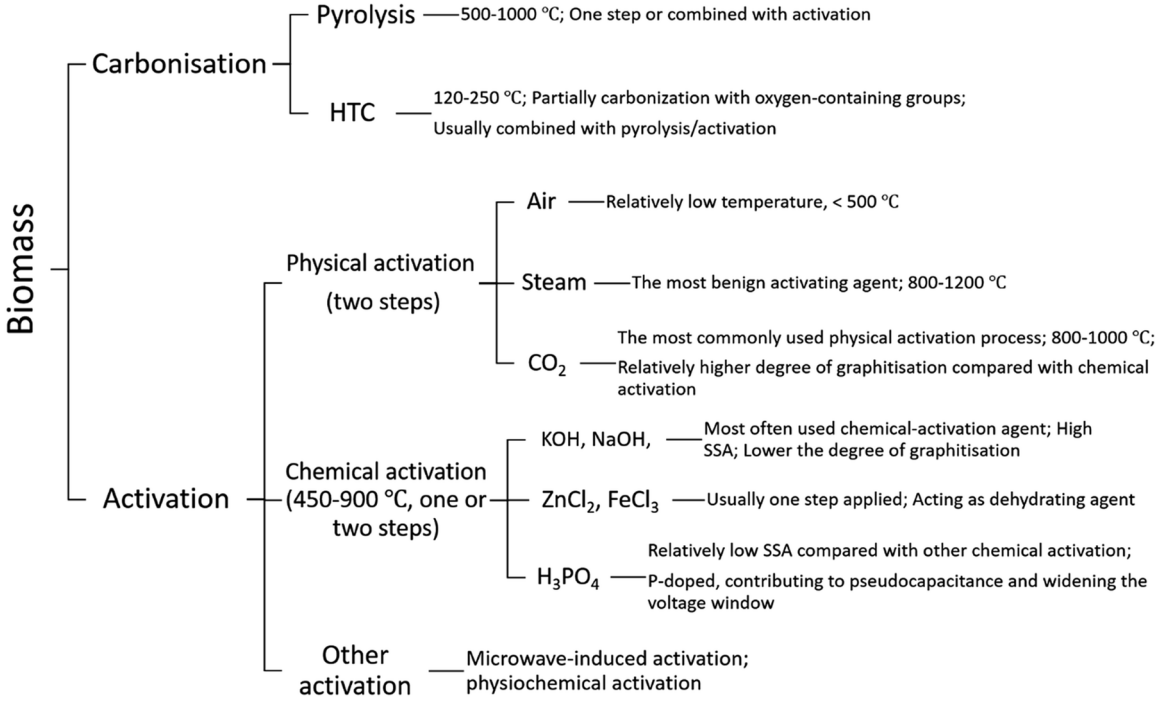

Figure 2.6 Methods commonly used for obtaining carbon materials from biomass [18].

To improve the performance of biomass-derived carbon materials like porosity, electrolyte wettability, conductivity and strength, several activation processes are carried out using physical and chemical means [19]. Procuring carbon materials from natural sources sometimes can involve pyrolysis at temperatures ranging from ~400-1300 °C and in-situ activation during this process by introduction of gases like oxygen, carbon dioxide, water vapour or other gas mixture. Pre-treatment of biomass or post-treatment of obtained carbon material with agents like KOH, NaOH, H_3PO_4, H_2SO_4 could also be carried out so as to activate the surface. A combination of both ex-situ or in-

situ activation methods is also a generally used method to obtain carbon materials from biomass precursors [19].

In some cases, hydrothermal carbonisation is also employed to obtain carbon materials. This thermo-chemical treatment initially yields a hydrochar that has high-density of oxygen-containing functional groups which sometimes are directly used or further processed to serve as electrode materials in batteries. The hydrochar could be subjected to further pyrolysis with or without chemical or physical activation. The process utilised for the generation of carbon materials significantly affect its physicochemical and thermo-mechanical properties [18].

Apart from pyrolysis and hydrothermal process several unconventional methods have also been employed to generate carbon materials like carbon nanoparticles from biomass. There have been recent reports on carbon nanoparticles from the soot with sizes ranging from 40-50 nm with tuneable surface chemistries [20]. In another work [21], highly fluorescent carbon nanodots were also prepared from such flame deposition route where the obtained carbon nanoparticles were disintegrated into smaller particles by using strong oxidising agents. The carbon nanodots showed a blue-green fluorescence and were used for sensing the presence of heavy metal ions in water (**Figure 2.7**).

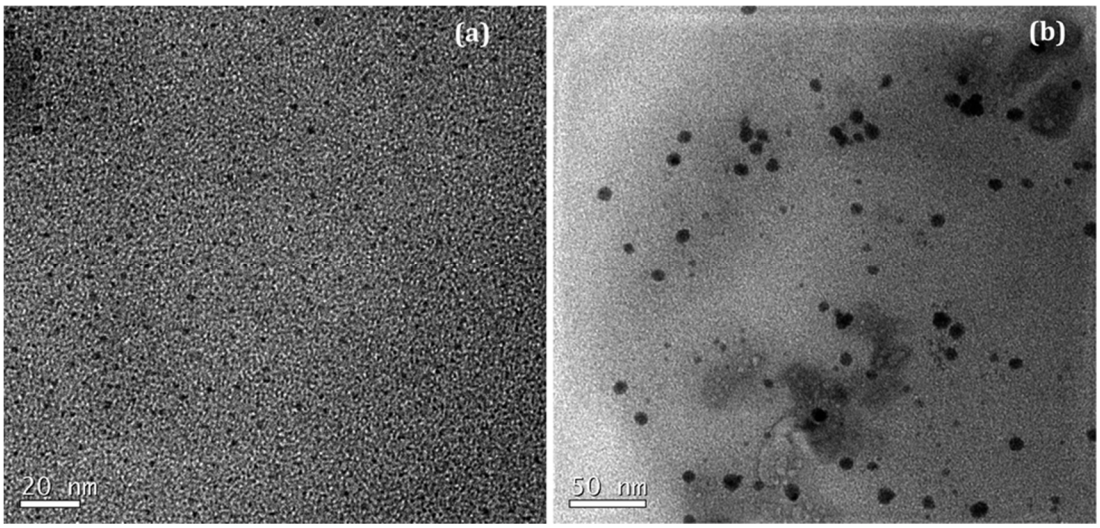

Figure 2.7 TEM images of carbon nanodots (a) before and (b) after dialysis [21].

Biomass as a precursor for carbon material synthesis also generates hard carbons with larger *d*-spacing and defects. Such structures are more advantages for the larger sodium-ion to reversibly store in such carbon material. Therefore, biomass-derived precursors provide much better electrochemical performance than the aforementioned allotropes of carbon like CNT,

graphene or fullerene for sodium-ion batteries (NIBs) [22]. The electrochemical performance of such biomass-derived hard carbon materials for LIBs and NIBs are discussed in the sessions below while describing the respective battery systems.

2.1.5 Heteroatom-doped carbon materials

Doping is a form of replacing a carbon atom with a heteroatom in the graphitic plane (**Figure 2.8**). Doping of carbon materials enables alterations to their electrochemical and thermo-mechanical properties. The doping of heteroatoms in carbon materials can be done either during the synthesis or even after the synthesis has been carried out. Doping after synthesizing the carbon will help to maintain the bulk properties. However, the even distribution of functional groups can be achieved when the carbon material is doped with heteroatom in-situ. Although structural deformations take place while doping, heteroatoms like sulphur, nitrogen, boron or dual-doping offer properties beneficial for the state-of-art energy applications. Such a doping might help enhance the energy state at the Fermi level and therefore overcome capacitance limitations of carbons and improve the specific capacity leading to superior battery performance [23]. Recent investigations have shown that the electrochemical performance arises from a change in the charge distribution caused by the differences in the electron negativities between carbon and heteroatoms [24].

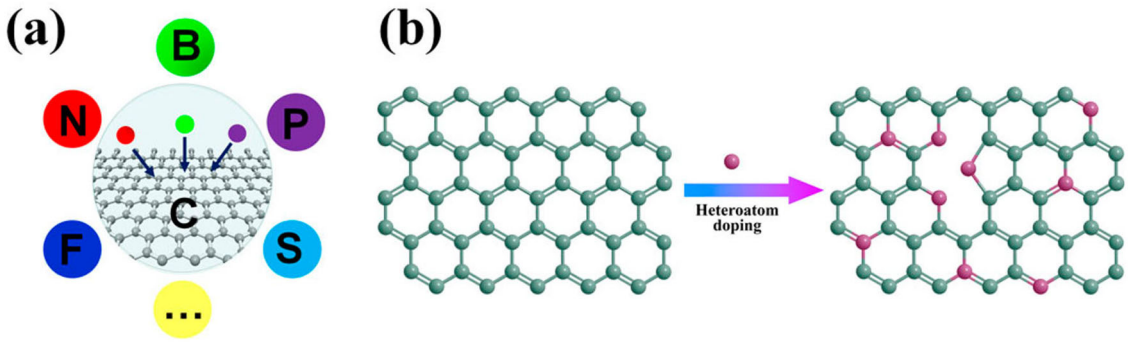

Figure 2.8 (a) Heteroatom dopants for graphite [25]. (b) Post-treatment doping of heteroatom [26].

2.2 Carbon materials for energy storage

2.2.1 Lithium-ion batteries

LIB has conquered the market of portable energy storage technology owing to their high energy storage capabilities, endorsed by the small size of lithium-ion which can readily afford an efficient intercalation and de-intercalation profile [27]. A typical LIB consists of a cathode, an anode, a separator and an ion-conducting electrolyte. The electrolyte should be conducting ions and inert to the electron transport. The anode and cathode materials are generally isolated onto the current collector that help in the transport of electrons originating from the redox reactions to the external load [28]. When a battery is discharged the lithium-ions from the anode gets inserted into the cathode and vice versa occurs during charge. The discharge process in the battery reduces the cathode as it accepts electrons and oxidises the anode. This lithiation and delithation process indicate the reversibility of the battery. Superior conduction of electrons, low cost, stability during prolonged cycling and reversible insertion and de-insertion of ions are some of the characteristics required for an active material.

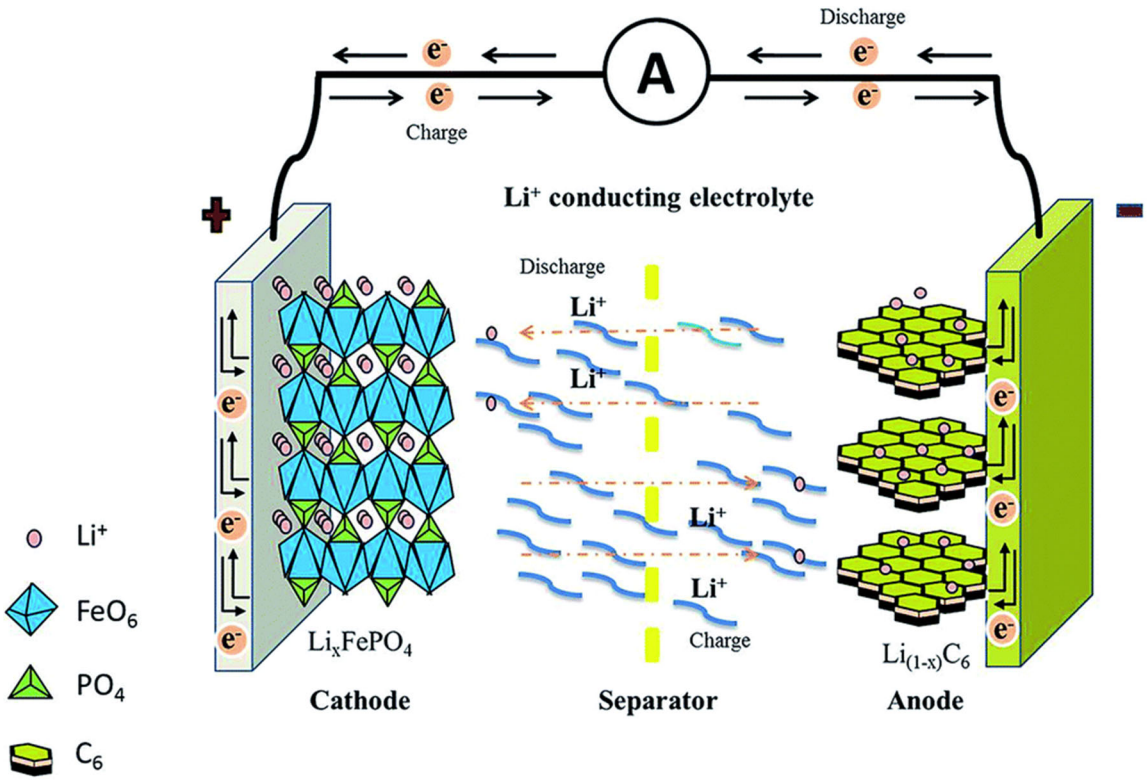

Figure 2.9 Schematic illustration of the working principle of the LIB system [28].

In addition, an electrolyte chosen should be non-aqueous as lithium undergoes an exothermic reaction with water and might cause safety concerns. In general, organic liquids like ethylene carbonate, dimethyl carbonate or diethyl carbonate which are compatible with lithium salts are

used as electrolytes. The most commonly used state of the art cathodes in LIBs are $LiCoO_2$, $LiMn_2O_4$, $LiFePO_4$ etc., while graphite is the most commonly used anode material [29]. In general, carbon materials are used in the anode component of the LIB. **Figure 2.9** represents the operation of the lithium-ion based battery system.

2.2.1.1 Carbon-based anodes for lithium-ion batteries

Anode materials for LIBs have received much attention in the past decade. Selection of anode materials is generally based on the material's working potential, electrical conductivity, cost, and stability. Pristine lithium metal was considered a suitable candidate as anode owing to its redox potential and a very high theoretical capacity of ~3860 mA h g^{-1} [29]. Nevertheless, upon repeated cycling, the lithium metal form dendrites, causing thermal runaway and thus hinder the practical application of lithium metal as an anode in LIB [30]. Hence, researchers have focused on other carbonaceous materials broadly classified into (i) graphitizable carbons (soft carbons) where an orderly arrangement of graphitic crystallites are present and (ii) non-graphitizable carbons (hard carbons) where a disordered arrangement of crystallites are present [29]. Soft carbons are quite often used in commercial batteries owing to their cycling stability, significantly reversible specific capacity, cycle life and coulombic efficiency (>90%) [31]. The mechanism of lithium interaction with such carbon systems, especially graphite has been subject to extensive study. Graphite is amongst the most commonly used anode material in LIB with a theoretical capacity of 372 mA h g^{-1} [32]. This is established on the consideration that a lithium atom reacts with six carbon atoms in a completely reversible intercalation and de-intercalation process [32].

Despite the immense production of graphite, it shows low specific capacity especially for applications involving hybrid electric vehicles, making its use confined to low-power portable electronic devices like laptops and mobile phones. Hence, amongst carbon materials CNTs were investigated as anodes in LIBs owing to its highest specific theoretical capacity (1116 mA h g^{-1} for single-walled nanotubes) achievable for any carbon material [33, 34]. Such high capacities could be achieved by lithium intercalation with pseudo-graphitic layers and carbons present inside the hollow tubes [29]. Dileo *et al*. [35] reported single-walled carbon nanotubes electrodes with titanium contacts as anodes in LIBs with an exceptionally high specific capacity of 1050 mA h g^{-1}, representing a dramatic improvement in capacity over the conventional graphite electrode. Nevertheless, the electrodes had a relatively low coulombic efficiency owing to its architecture and high voltage hysteresis [29]. Hence, overcoming such issues Oktaviano *et al*. [36] proposed an effective strategy for energy nanoscale porosity (4nm sized

holes) onto carbon nanotubes by anchoring cobalt-oxide nanoparticles and etching them out using an acid wash (**Figure 2.10**). A superior performing anode with improved cycling stability, rate capability and efficiency were obtained.

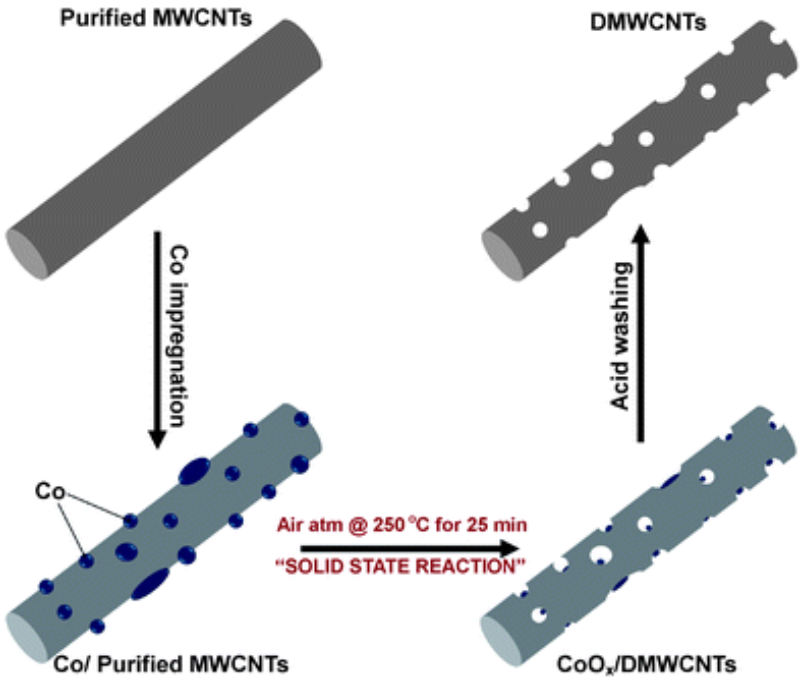

Figure 2.10 Schematic representation of the strategy for nanopore creation on carbon nanotubes [36].

In addition, other strategies like carbon-alloy composites are used to further enhance the capacity of carbon. For instance, carbon nanotubes and few-layered graphene combined with a variety of metal oxides or transition metals have been reported. In a study by Ramaprabhu *et al*. [37] SnO_2 nanoparticle dispersed in nitrogen-doped graphene anode material showed a very good rate capability and reversible capacity of 1220 mA h g^{-1} after 100 cycles in LIBs. Similarly, silicon nanowire, graphene sheaths and reduced graphene oxide derived free-standing electrode showed an excellent performance with a specific capacity retention of 1600 mA h g^{-1} at 2.1 A g^{-1} after 100 cycles (~80% capacity retention) [38].

Though alloyed carbon nanotubes have shown high specific capacity, their high-cost and low-cycle file restrict their affordability for commercial LIBs. Hence,biomass-derived hard carbons that show superior capacity (> 500 mA h g^{-1}) were researched as an alternative anode to the available soft carbons [29]. Hard carbons are made up of carbons with a high level of disorders arising from the random arrangement of graphene sheets making lithium insertion more feasible but with dawdling lithium diffusion. Their high specific capacity has attracted industries to target such carbons for use in electric vehicles. Hard carbons have poor rate

capability, high loss in initial capacity and low tap density. As a result, many methods like surface oxidation, fluorination or alloying have been used to overcome this problem [39, 40]. It is interesting to note that, such treatments have resulted in higher coulombic efficiencies and specific capacity. Hu *et al*.[41] observed that porous hard carbons generated a capacity of more than 400 mA h g^{-1}. In another work (**Figure 2.11**), sucrose derived hard carbons with nanoscale porosity show a good cycling stability, rate capability and reversible specific capacity of 503 mA h g^{-1} [42].

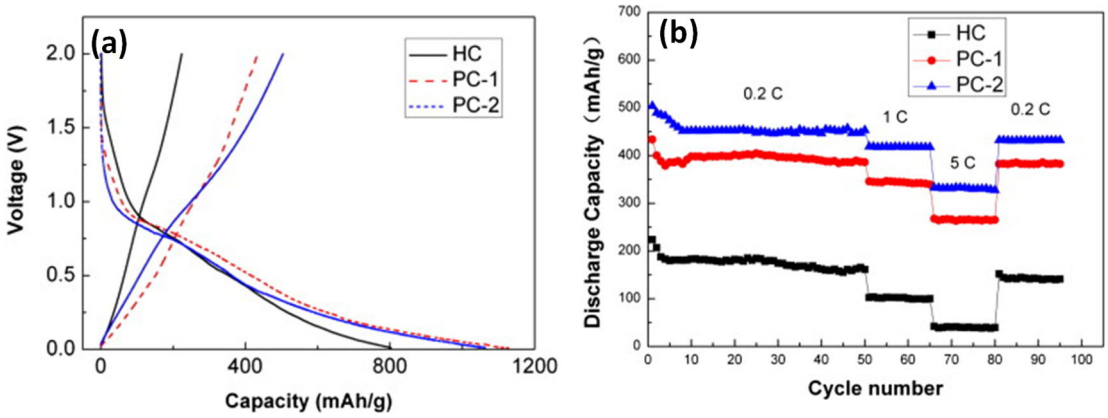

Figure 2.11 (a) First cycle charge-discharge curve (at 0.2 C) and (b) rate capability studies of sucrose derived carbon as anodes in LIB [42].

In another interesting work, binder and collector free anodes were tested in batteries Campbell *et al.* [43] reported a mushroom-derived free-standing electrode for LIB (**Figure 2.12**). Here, the mushroom peel was subjected to treatment at elevated temperature (>900 ºC) to obtain heteroatom-doped, hierarchically porous carbons. A specific capacity of 260 mA h g^{-1} was retained after 700 cycles as an indication of the exceptional cycling stability provided by such carbon materials.

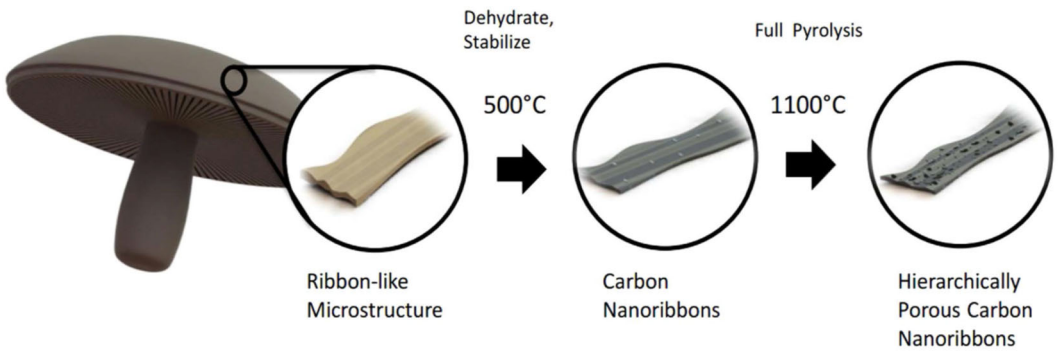

Figure 2.12 Schematic representation of mushroom skin-derived hierarchically porous carbon ribbons **[43]**.

2.2.2 Sodium-ion batteries

Although LIBs are presently used in portable electronics and electric vehicles, it is necessary to consider the availability of lithium precursors on earth's crust [44]. Only 20 ppm of lithium is present in the earth's crust making, which is geographically limited and might cause political fluxes in future [45]. Hence, sodium-ion battery (NIB) is an effective technology not only because of its unlimited presence on the earth's crust but also because of its similarities with lithium in terms of chemical interaction. The NIB design is similar to that of LIB comprising an anode, cathode, a separator and an ion-conducting electrolyte (**Figure 2.13**).

The commercialised sodium based technologies like Na/S and $Na/NiCl_2$ is only operable at a temperature of ~300°C for maintaining the electrodes in a liquid state [46, 47]. Such systems cause safety hazards. In contrast, NIBs use insertion materials making it free from metallic sodium. Room-temperature operable NIBs can find potential applications for electrical grid storage where specific volumetric and gravimetric energy density are not stringent [44]. Using such renewable resources derived NIBs can significantly reduce the cost involved and can penetrate the energy market as a rival to LIB technology. During the process of discharge, sodium ions from the anode get inserted into the cathode and vice-versa during charge. The reversible insertion and de-insertion of sodium ion indicate reversible charging/discharging of the battery.

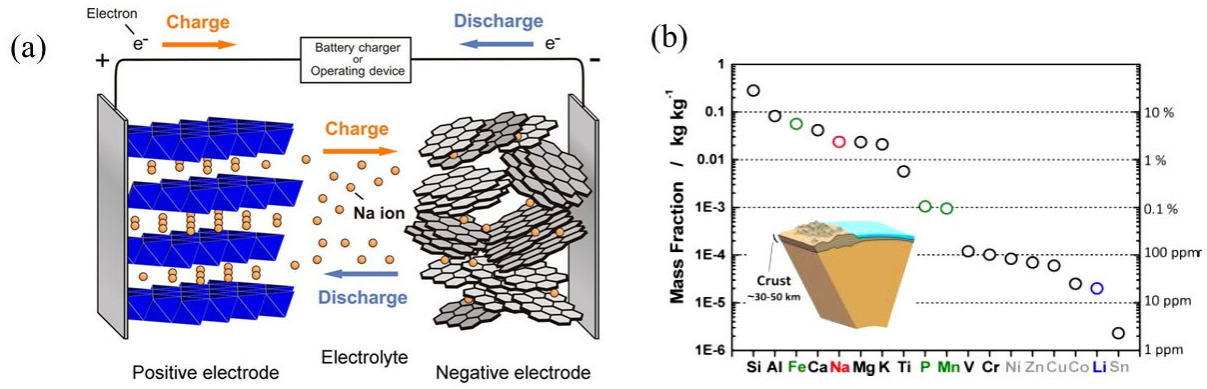

Figure 2.13 (a) Schematic for the working principle of Sodium-ion battery and (b) resource availability of lithium and sodium in the earth's crust **[44]**.

Although NIBs cannot be compared with LIB counterpart as a leading technology, they should not be marginalized. In fact, NIBs were researched on par with that of LIBs in the late 1970's [48]. However, the successful application of LIBs diverted the research focus from NIBs [48, 49]. An important aspect of a battery is to enhance the energy density. In the case of commercial

LIBs, the energy density is largely dependent on graphite as anode and $LiCoO_2$ as a cathode material. As a result, the research on NIBs is focused on increasing the energy density of secondary batteries by finding suitable electrode material. It is important to underline the fact that sodium ions have a relatively large ionic radius (0.102 nm) as compared to that of the lithium (0.076 nm) and preferably coordinate in the octahedral or prismatic sites [50].

The larger ionic radius of sodium-ion demand larger channels and interstitial sites for sodium-ion intercalation [51]. Consequently, the important factor is to identify and develop suitable electrode materials with high interlayer *d*-spacing for easy transport of sodium-ions. The has been significant research progress in cathode materials for NIBs [52, 53], whilst only a few anode materials are found suitable for NIBs. Though a specific capacity of ~ 1165 mA h g^{-1} can be obtained while using pristine sodium metal as anode it wit eventually lead to the formation of dendrites causing catastrophic failure of battery [54]. Thus other anodes like carbon materials [48], metal oxides [55-57], metal nitrides [58] and alloyed materials [59, 60] were investigated. Amongst the limited number of anode materials for NIBs, carbon nanomaterials are promising due to their abundance, ease of production, conductivity, corrosion resistance and low cost[48, 61]. Nevertheless, sodium insertion into the commonly-used commercial anode for LIBs i.e., graphite shows a low reversible capacity of 35 mA h g^{-1} because of its lower interlayer spacing [62]. Therefore, it was concluded that an increased *d*-spacing for carbon materials provide better sodium-ion transport [63]. Therefore, the key factor to store sodium-ions is to increase the interlayer spacing in graphite/graphene lattice, introduce turbostratic disorders or generate vacancies.

2.2.2.1 Carbon-based anodes for sodium-ion batteries

The main reason for choosing carbon as a potential anode material is due to its cost-effectiveness, high abundance, excellent corrosion resistance, conductivity and high surface area. However, graphitic carbons seldom show good performance in NIBs, unlike LIB. This is because of the larger ionic radius of sodium rendering such insertion thermodynamically unfavourable. Hence, hard carbons (carbons with turbostratic disorders) have been studied as anode materials for NIB. Such carbon materials possess edge/ defect sites at vacancies, the enhanced interlayer spacing in the turbostratic domains and empty pores for sodium interaction. Such a structure achieves a reversible capacity up to 300 mA h g^{-1} for a stoichiometry of $NaC_{7.4}$ [64]. The morphology of carbon material also seems to affect the performance. Doeff *et al*. [65] used petroleum coke of different sizes and inferred that the reversibility of hard carbon is

size dependent. Hence, size and morphology seem to play a significant role in the electrochemical performance of carbons with regards to sodium-ion storage. Materials with nanodomains like nanofibers, nanosheets, mesoporous carbon, carbon nanotubes, nanospheres etc. have been reported as negative electrode materials in NIB [48]. Tang *et al*. [66] showed a superior rate capability in hollow carbon nanospheres. A specific discharge capacity of 100 mA h g^{-1} was obtained at a current density of 2000 mA g^{-1}, which was much higher than those previously reported for NIBs.

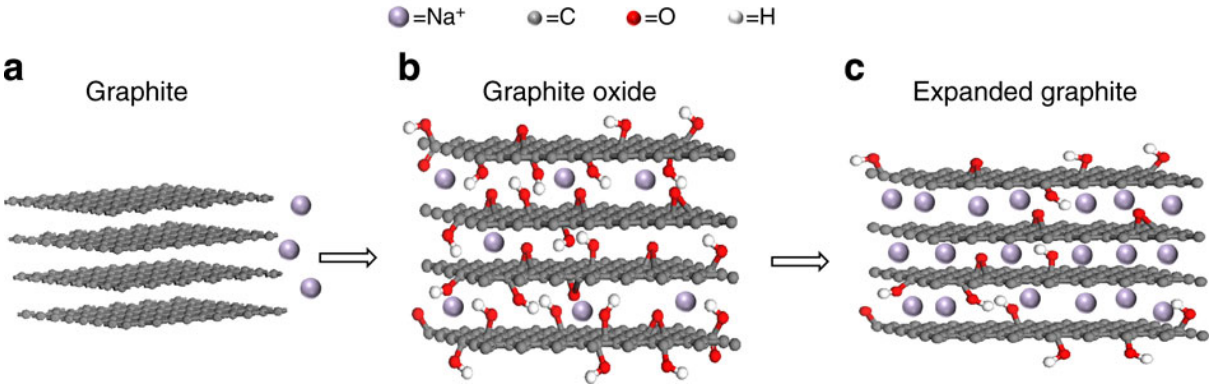

Figure 2.14 Schematic for sodium insertion in expanded graphite **[67]**.

Few layered graphene has a large surfacer area with superior conductivity and chemical inertness. Therefore, they hold a great potential as an electrode material for electrochemical energy storage. Though such graphene sheets have been used in the past as anodes for LIBs, they have recently emerged as potential anode materials for NIBs [68-73].

As seen earlier the larger ionic radius of sodium mandate larger interlayer *d*-spacing for reversible ion insertion. Reduced graphene oxide (RGO) has shown promise in this regard with superior sodium-ion storage properties. A recent study on reduced graphene oxide (RGO) by Dou and co-workers [69] have shown that an interlayer spacing of 3.7 Å could deliver a capacity of 174 mA h g^{-1} at a current density of 40 mA g^{-1}. In order to further increase the specific capacity, the interlayer spacing was increased to 4.3 Å which delivered a discharge capacity of 280 $mAhg^{-1}$ at a current density of 20 mAg^{-1}. (**Figures 2.14 and 2.15**). In another work [74], a reduced graphene oxide prepared by an environmentally friendly metal based reduction of graphene oxide delivered a capacity of 272 mA h g^{-1} at a current density of 50 mA g^{-1} respectively, with an excellent cycling stability of more than 300 cycles. Density functional theory calculations were carried out in order to investigate the superior performance of the anode which revealed that the defects in the graphene aided better sodium-ion storage. Also,

the work calculated the capacity obtained in the presence of a small amount of Stone-Wales defect that showed a reasonable estimate of the obtained capacity.

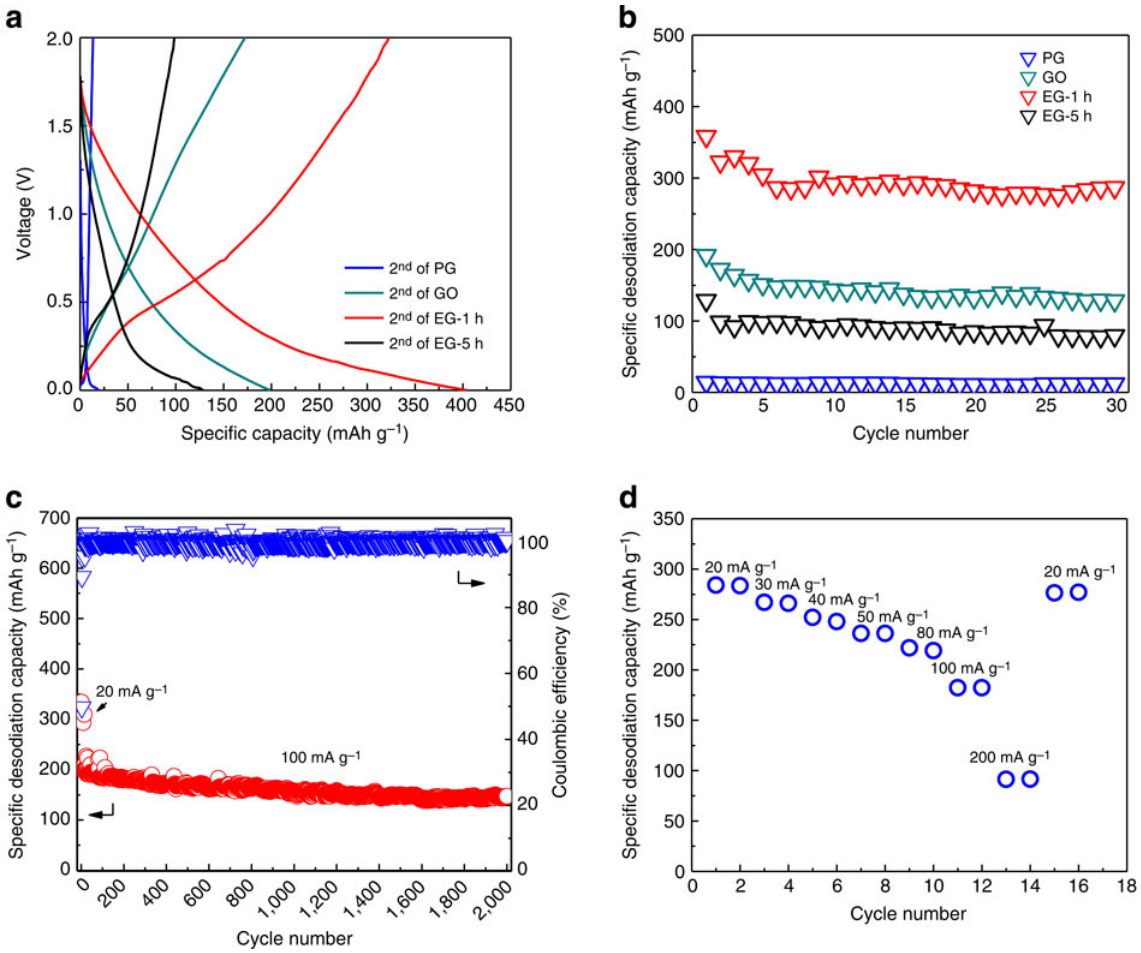

Figure 2.15 (a) Second cycle charge/discharge curves and (b) short-term stability of graphite (PG), graphene Oxide (GO), and expanded graphite (EG) at a current density of 20 mA g^{-1}. (c) Stability of EG for 2000 cycles. (d) Rate capability test for EG [67].

Further improving on the specific capacity, recent works on hard carbons from sustainable biomass resources have shown superior performances with capacities reaching that of graphite-based electrodes in LIBs. Several researchers have worked to produce high-performance biomass-derived carbon materials [3, 51, 75-142]. Some of the important works are briefly discussed here. Lotfabad *et al.* [51] reported a pseudo–graphite derived from banana peel that offered a gravimetric capacity of 328 mA h g^{-1} for NIB (**Figure 2.16**). The material had a low-surface area ranging from 19-217 m^2 g^{-1} depending on the treatment conditions. The pseudo-graphite showed larger interlayer spacing for insertion of sodium with the surface-accessible pores and possess substantial defects on the graphitic micro-crystallites for better sodium-adsorption. In a work reported by Zhu *et al*. [141], an Sn film coated onto a hierarchical wood

fibre was used as an electrode in NIB. The wood fibre was initially treated with CNT for enhancing the conductivity prior to Sn deposition. The material was tested as anode against sodium which delivered excellent cycling stability alongside a high discharge Capacity of 339 mA h g^{-1}. The electrode pulverisation was avoided through a wrinkling effect produced by the wood fibre that released the mechanical stress associated with volume expansion.

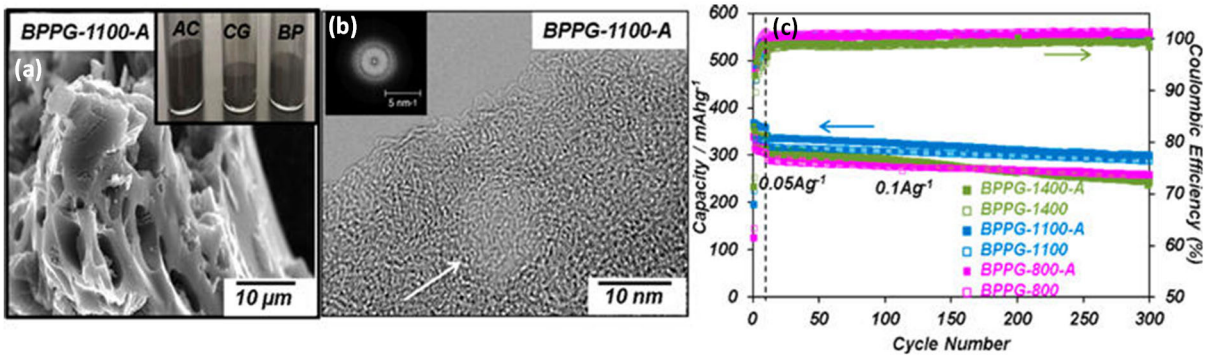

Figure 2.16 (a) Scanning electron microscope image (b) TEM image of banana peel derived pseudo-graphite, and (c) cycling stability of BPPG tested as an anode in NIBs [51].

In a recent work by Wang and co-workers, they reported a hierarchically porous carbon from peanut shell as an anode material for NIBs [112]. A high initial charge capacity of 431 mA h g^{-1} at 100 mA g^{-1} was observed. Excellent cycling stability was also reported, where 83-86 % of the capacity was retained after 200 cycles. The surface area, accessible surface pores, increased graphite interlayer spacing, and the overall geometry was responsible for the battery stability. In a recent report by Yang *et al*. [107] okra derived nitrogen-doped carbon sheets were tested as anodes in NIBs. The carbon sheets possessed a high specific surface area and showed a reversible capacity of 292 mA h g^{-1}, good cycling stability (about 2000 cycles) and near 100% coulombic efficiency was obtained.

The capacities of the anode materials can further be improved by introducing heteroatom dopants, with the most common one being nitrogen. Such doped carbons can enhance redox reactions, create defects and lead to the formation of disordered structures therefore boosting the sodium-ion storage [143]. Various nitrogen species like quaternary, pyridinic, and pyrrolic nitrogen[144-146] have been identified to influence the sodium-ion storage capabilities [147]. In a work by Yan and coworkers[107], hard carbons derived from biomass *okara*, that were enriched pyrrolic and graphitic nitrogen functional groups, showed a longer cycle life and rate

performance in NIBs. The present thesis has investigated such doped carbon materials as prospective anodes for NIBs.

2.3 References

[1] S. Damien, O. Brahim, X. Biwei, C. Daniel, L. Xiaolin, R. Teófilo, Adv. Energy Mater., 8 (2018) 1703268.

[2] D.A. Stevens, J.R. Dahn, J. Electrochem. Soc., 148 (2001) A803-A811.

[3] Y. Yao, F. Wu, Nano Energy, 17 (2015) 91-103.

[4] K.S. Novoselov, A.K. Geim, S.V. Morozov, D. Jiang, Y. Zhang, S.V. Dubonos, I.V. Grigorieva, A.A. Firsov, Science, 306 (2004) 666-669.

[5] D. Haag, H.H. Kung, Topics in Catalysis, 57 (2013) 762-773.

[6] R. Raccichini, A. Varzi, S. Passerini, B. Scrosati, Nat. Mater., 14 (2014) 271.

[7] H. Kroto, Nature (London), 318 (1985) 162.

[8] Q.L. Zhang, S. O'Brien, J. Heath, Y. Liu, R. Curl, H. Kroto, R. Smalley, J. Phys. Chem., 90 (1986) 525-528.

[9] R. Taylor, D.R.M. Walton, Nature, 363 (1993) 685.

[10] M. Vizuete, M. Barrejon, M.J. Gomez-Escalonilla, F. Langa, Nanoscale, 4 (2012) 4370-4381.

[11] R.O. Loutfy, S. Katagiri, Fullerene Materials for Lithium-ion Battery Applications, in: E. Ōsawa (Ed.) Perspectives of Fullerene Nanotechnology, Springer Netherlands, Dordrecht, 2002, pp. 357-367.

[12] R. Zhang, F. Mizuno, Google Patents2015.

[13] I.Y. Jeon, D.W. Chang, N.A. Kumar, J.-B. Baek, ISBN 978-953-307-498-6, Published by InTech under CC BY-NC-SA 3.0 LICENSE2011.

[14] N. Hamada, S.-i. Sawada, A. Oshiyama, Phys. Rev. Lett., 68 (1992) 1579-1581.

[15] V.N. Popov, Mater. Sci. Eng.: R: Reports, 43 (2004) 61-102.

[16] R.H. Baughman, A.A. Zakhidov, W. A. de Heer, Science, 297 (2002) 787-792.

[17] A. Hirsch, Angew. Chem., 41 (2002) 1853-1859.

[18] H. Lu, X.S. Zhao, Sustainable Energy & Fuels, 1 (2017) 1265-1281.

[19] Y.P. Gao, Z.B. Zhai, K.J. Huang, Y.Y. Zhang, New Journal of Chemistry, 41 (2017) 11456-11470.

[20] R.R. Gaddam, S. Kantheti, R. Narayan, K.V.S.N. Raju, RSC Adv., 4 (2014) 23043-23049.

[21] R.R. Gaddam, D. Vasudevan, R. Narayan, K.V.S.N. Raju, RSC Adv., 4 (2014) 57137-57143.

[22] P. Kalyani, A. Anitha, Int. J. Hydrogen Energy, 38 (2013) 4034-4045.

[23] K. Nanjundan Ashok, B. Jong-Beom, Nanotechnology, 26 (2015) 492001.

[24] L. Hao, S. Zhang, R. Liu, J. Ning, G. Zhang, L. Zhi, Adv. Mater., 27 (2015) 3190-3195.

[25] L. Dai, Y. Xue, L. Qu, H.-J. Choi, J.-B. Baek, Chem. Rev., 115 (2015) 4823-4892.

[26] L. Dai, Acc. Chem. Res., 46 (2013) 31-42.

[27] L. Lu, X. Han, J. Li, J. Hua, M. Ouyang, J. Power Sources, 226 (2013) 272-288.

[28] X. Zhang, L. Ji, O. Toprakci, Y. Liang, M. Alcoutlabi, Polymer Rev., 51 (2011) 239-264.

[29] S. Goriparti, E. Miele, F. De Angelis, E. Di Fabrizio, R. Proietti Zaccaria, C. Capiglia, J. Power Sources, 257 (2014) 421-443.

[30] J. M. Tarascon, M. Armand, Nature, 414 (2001) 359-367.

[31] O. Haik, S. Ganin, G. Gershinsky, E. Zinigrad, B. Markovsky, D. Aurbach, I. Halalay, J. Electrochem. Soc., 158 (2011) A913-A923.

[32] C. M. Park, W. Choi, Y. Hwa, J.-H. Kim, G. Jeong, H.-J. Sohn, J. Mater. Chem., 20 (2010) 4854-4860.

[33] V. Meunier, J. Kephart, C. Roland, J. Bernholc, Phys. Rev. Lett., 88 (2002) 075506.

[34] C.M. Schauerman, M.J. Ganter, G. Gaustad, C.W. Babbitt, R.P. Raffaelle, B.J. Landi, J. Mater. Chem., 22 (2012) 12008-12015.

[35] R.A. DiLeo, A. Castiglia, M.J. Ganter, R.E. Rogers, C.D. Cress, R.P. Raffaelle, B.J. Landi, ACS Nano, 4 (2010) 6121-6131.

[36] H.S. Oktaviano, K. Yamada, K. Waki, J. Mater. Chem., 22 (2012) 25167-25173.

[37] B.P. Vinayan, S. Ramaprabhu, Journal of Materials Chemistry A, 1 (2013) 3865-3871.

[38] B. Wang, X. Li, X. Zhang, B. Luo, M. Jin, M. Liang, S.A. Dayeh, S.T. Picraux, L. Zhi, ACS Nano, 7 (2013) 1437-1445.

[39] J. Wang, J.-L. Liu, Y.-G. Wang, C.-X. Wang, Y.-Y. Xia, Electrochim. Acta, 74 (2012) 1-7.

[40] H. Fujimoto, K. Tokumitsu, A. Mabuchi, N. Chinnasamy, T. Kasuh, J. Power Sources, 195 (2010) 7452-7456.

[41] J. Hu, H. Li, X. Huang, Solid State Ionics, 176 (2005) 1151-1159.

[42] J. Yang, X.-y. Zhou, J. Li, Y.-l. Zou, J.-j. Tang, Mater. Chem. Phys., 135 (2012) 445-450.

[43] B. Campbell, R. Ionescu, Z. Favors, C.S. Ozkan, M. Ozkan, Sci. Rep., 5 (2015) 14575.

[44] N. Yabuuchi, K. Kubota, M. Dahbi, S. Komaba, Chem. Rev., 114 (2014) 11636-11682.

[45] R.S. Carmichael, Physical properties of rocks and minerals, CRC press Boca Raton1989.

[46] T. Oshima, M. Kajita, A. Okuno, Int. J. App. Ceramic Tech., 1 (2004) 269-276.

[47] R.J. Bones, D.A. Teagle, S.D. Brooker, F.L. Cullen, J. Electrochem. Soc., 136 (1989) 1274-1277.

[48] M.S. Balogun, Y. Luo, W. Qiu, P. Liu, Y. Tong, Carbon, 98 (2016) 162-178.

[49] V.L. Chevrier, G. Ceder, J. Electrochem. Soc., 158 (2011) A1011-A1014.

[50] J. Qian, X. Wu, Y. Cao, X. Ai, H. Yang, Angew. Chem., 125 (2013) 4731-4734.

[51] E.M. Lotfabad, J. Ding, K. Cui, A. Kohandehghan, W.P. Kalisvaart, M. Hazelton, D. Mitlin, ACS Nano, 8 (2014) 7115-7129.

[52] D. Kundu, E. Talaie, V. Duffort, L.F. Nazar, Angew. Chem. Int. Ed., 54 (2015) 3431-3448.

[53] L.P. Wang, L.H. Yu, X. Wang, M. Srinivasan, Z.C.J. Xu, J. Mater. Chem. A, 3 (2015) 9353-9378.

[54] M.D. Slater, D. Kim, E. Lee, C.S. Johnson, Adv. Funct. Mater., 23 (2013) 947-958.

[55] H. Xiong, M.D. Slater, M. Balasubramanian, C.S. Johnson, T. Rajh, J. Phys. Chem. Lett., 2 (2011) 2560-2565.

[56] Y. Jiang, M. Hu, D. Zhang, T. Yuan, W. Sun, B. Xu, M. Yan, Nano Energy, 5 (2014) 60-66.

[57] H. Yu, Y. Ren, D. Xiao, S. Guo, Y. Zhu, Y. Qian, L. Gu, H. Zhou, Angew. Chem. Int. Ed., 53 (2014) 8963-8969.

[58] X.J. Li, M.M. Hasan, A.L. Hector, J.R. Owen, J. Mater. Chem. A, 1 (2013) 6441-6445.

[59] Y. Kim, Y. Park, A. Choi, N.S. Choi, J. Kim, J. Lee, J.H. Ryu, S.M. Oh, K.T. Lee, Adv. Mater., 25 (2013) 3045-3049.

[60] L. Wu, X.H. Hu, J.F. Qian, F. Pei, F.Y. Wu, R.J. Mao, X.P. Ai, H.X. Yang, Y.L. Cao, Energy Environ. Sci., 7 (2014) 323-328.

[61] B. Jache, P. Adelhelm, Angew. Chem. Int. Ed., 53 (2014) 10169-10173.

[62] P. Ge, M. Fouletier, Solid State Ionics, 28 (1988) 1172-1175.

[63] Y. Cao, L. Xiao, M.L. Sushko, W. Wang, B. Schwenzer, J. Xiao, Z. Nie, L.V. Saraf, Z. Yang, J. Liu, Nano Lett., 12 (2012) 3783-3787.

[64] C. Bommier, T.W. Surta, M. Dolgos, X. Ji, Nano Lett., 15 (2015) 5888-5892.

[65] M.M. Doeff, Y. Ma, S.J. Visco, L.C. De Jonghe, J. Electrochem. Soc., 140 (1993) L169-L170.

[66] K. Tang, L. Fu, R.J. White, L. Yu, M.-M. Titirici, M. Antonietti, J. Maier, Adv. Energy Mater., 2 (2012) 873-877.

[67] Y. Wen, K. He, Y. Zhu, F. Han, Y. Xu, I. Matsuda, Y. Ishii, J. Cumings, C. Wang, Nature Comm., 5 (2014) 4033.

[68] Y. Yan, Y.X. Yin, Y.G. Guo, L.J. Wan, Adv. Energy Mater., 4 (2014) 1301584.

[69] Y.X. Wang, S.L. Chou, H.K. Liu, S.X. Dou, Carbon, 57 (2013) 202-208.

[70] Y.S. Yun, Y.-U. Park, S.-J. Chang, B.H. Kim, J. Choi, J. Wang, D. Zhang, P.V. Braun, H.-J. Jin, K. Kang, Carbon, 99 (2016) 658-664.

[71] X.F. Luo, C.H. Yang, Y.Y. Peng, N.W. Pu, M.D. Ger, C.T. Hsieh, J.K. Chang, J. Mater. Chem. A, 3 (2015) 10320-10326.

[72] J.C. Pramudita, D. Pontiroli, G. Magnani, M. Gaboardi, M. Riccò, C. Milanese, H.E.A. Brand, N. Sharma, ChemElectroChem, 2 (2015) 600-610.

[73] L. David, G. Singh, J. Phys. Chem. C, 118 (2014) 28401-28408.

[74] N.A. Kumar, R.R. Gaddam, S.R. Varanasi, D. Yang, S.K. Bhatia, X.S. Zhao, Electrochim. Acta, 214 (2016) 319-325.

[75] Z. Zhu, F. Liang, Z. Zhou, X. Zeng, D. Wang, P. Dong, J. Zhao, S. Sun, Y. Zhang, X. Li, J. Mater. Chem. A, 6 (2018) 1513-1522.

[76] Y. Zhu, M. Chen, Q. Li, C. Yuan, C. Wang, Carbon, 129 (2018) 695-701.

[77] N. Zhang, Q. Liu, W. Chen, M. Wan, X. Li, L. Wang, L. Xue, W. Zhang, J. Power Sources, 378 (2018) 331-337.

[78] G. Zeng, B. Zhou, L. Yi, H. Li, X. Hu, Y. Li, Sustainable Energy & Fuels, 2 (2018) 855-861.

[79] C. Yang, J. Xiong, X. Ou, C.-F. Wu, X. Xiong, J.-H. Wang, K. Huang, M. Liu, Mater. Today Energy, 8 (2018) 37-44.

[80] M.K. Rybarczyk, Y. Li, M. Qiao, Y.-S. Hu, M.-M. Titirici, M. Lieder, J. Energy Chem., (2018).

[81] B. Luo, Y. Hu, X. Zhu, T. Qiu, L. Zhi, M. Xiao, H. Zhang, M. Zou, A. Cao, L. Wang, J. Mater. Chem. A, 6 (2018) 1462-1472.

[82] R. Hao, Y. Yang, H. Wang, B. Jia, G. Ma, D. Yu, L. Guo, S. Yang, Nano Energy, 45 (2018) 220-228.

[83] R.R. Gaddam, N.A. Kumar, X.S. Zhao, Materials Today Energy, 8 (2018) 29-36.

[84] X. Dou, C. Geng, D. Buchholz, S. Passerini, APL Materials, 6 (2018).

[85] G. Zou, Z. Huang, G. Zhao, S. Li, H. Hou, X. Qiu, X. Ji, J. Electrochem. Soc., 164 (2017) A1431-A1437.

[86] Y. Zhu, M. Chen, Q. Li, C. Yuan, C. Wang, Carbon, 123 (2017) 727-734.

[87] H. Zhu, F. Shen, W. Luo, S. Zhu, M. Zhao, B. Natarajan, J. Dai, L. Zhou, X. Ji, R.S. Yassar, T. Li, L. Hu, Nano Energy, 33 (2017) 37-44.

[88] Y. Zheng, Y. Wang, Y. Lu, Y.-S. Hu, J. Li, Nano Energy, 39 (2017) 489-498.

[89] T.Y. Zhang, J.T. Chen, B.J. Yang, H.X. Li, S.L. Lei, X. Ding, RSC Adv., 7 (2017) 50336-50342.

[90] T. Zhang, J. Mao, X. Liu, M. Xuan, K. Bi, X.L. Zhang, J. Hu, J. Fan, S. Chen, G. Shao, RSC Adv., 7 (2017) 41504-41511.

[91] C.M. Wu, P.I. Pan, Y.W. Cheng, C.P. Liu, C.C. Chang, M. Avdeev, S.K. Lin, J. Power Sources, 340 (2017) 14-21.

[92] P. Wang, X. Zhu, Q. Wang, X. Xu, X. Zhou, J. Bao, J. Mater. Chem. A, 5 (2017) 5761-5769.

[93] K. Wang, Y. Jin, S. Sun, Y. Huang, J. Peng, J. Luo, Q. Zhang, Y. Qiu, C. Fang, J. Han, ACS Omega, 2 (2017) 1687-1695.

[94] J. Wang, P. Nie, B. Ding, S. Dong, X. Hao, H. Dou, X. Zhang, J. Mater. Chem. A, 5 (2017) 2411-2428.

[95] M. Wahid, Y. Gawli, D. Puthusseri, A. Kumar, M.V. Shelke, S. Ogale, ACS Omega, 2 (2017) 3601-3609.

[96] N. Sharma, Y. Gawli, A. Ahmad, M. Muhammed, S. Ogale, ChemistrySelect, 2 (2017) 6909-6915.

[97] H. Liu, M. Jia, S. Yue, B. Cao, Q. Zhu, N. Sun, B. Xu, J. Mater. Chem. A, 5 (2017) 9572-9579.

[98] R. Li, J. Huang, Z. Xu, H. Qi, L. Cao, Y. Liu, W. Li, J. Li, Energy Technology, (2017) n/a-n/a.

[99] K. Kim, D.G. Lim, C.W. Han, S. Osswald, V. Ortalan, J.P. Youngblood, V.G. Pol, ACS Sustainable Chem. & Eng., 5 (2017) 8720-8728.

[100] R.R. Gaddam, A.H.F. Niaei, M. Hankel, D.J. Bernhardt, A.K. Nanjundan, X.S. Zhao, J. Mater. Chem. A, (2017).

[101] R.R. Gaddam, E. Jiang, N. Amiralian, P.K. Annamalai, D.J. Martin, N.A. Kumar, X.S. Zhao, Sustainable Energy & Fuels, 1 (2017) 1090-1097.

[102] x. Dou, I. Hasa, M. Hekmatfar, T. Diemant, R.J. Behm, D. Buchholz, S. Passerini, ChemSusChem, (2017) n/a-n/a.

[103] M. Dahbi, M. Kiso, K. Kubota, T. Horiba, T. Chafik, K. Hida, T. Matsuyama, S. Komaba, J. Mater. Chem. A, 5 (2017) 9917-9928.

[104] Y. Zhou, W. Sun, X. Rui, Y. Zhou, W.J. Ng, Q. Yan, E. Fong, Nano Energy, 21 (2016) 71-79.

[105] Y.Z. Zhang, L. Chen, Y. Meng, J. Xie, Y. Guo, D. Xiao, J. Power Sources, 335 (2016) 20-30.

[106] Y. Zhang, Y. Meng, L. Chen, Y. Guo, D. Xiao, J. Mater. Chem. A, 4 (2016) 17491-17502.

[107] T. Yang, T. Qian, M. Wang, X. Shen, N. Xu, Z. Sun, C. Yan, Adv. Mater., 28 (2016) 539-545.

[108] T. Yang, X. Niu, T. Qian, X. Shen, J. Zhou, N. Xu, C. Yan, Nanoscale, 8 (2016) 15497-15504.

[109] D. Yan, C.Y. Yu, X.J. Zhang, W. Qin, T. Lu, B.W. Hu, H.L. Li, L.K. Pan, Electrochim. Acta, 191 (2016) 385-391.

[110] D. Xu, C. Chen, J. Xie, B. Zhang, L. Miao, J. Cai, Y. Huang, L. Zhang, Adv. Energy Mater., 6 (2016) 1501929.

[111] L.M. Wu, D. Buchholz, C. Vaalma, G.A. Giffin, S. Passerini, Chemelectrochem, 3 (2016) 292-298.

[112] H.L. Wang, W.H. Yu, J. Shi, N. Mao, S.G. Chen, W. Liu, Electrochim. Acta, 188 (2016) 103-110.

[113] R. Thangavel, K. Kaliyappan, K. Kang, X.L. Sun, Y.S. Lee, Adv. Energy Mater., 6 (2016) 1502199.

[114] T. Sun, Z.J. Li, H.G. Wang, D. Bao, F.L. Meng, X.B. Zhang, Angew. Chem. Int. Ed. Engl., 55 (2016) 10662-10666.

[115] F. Shen, W. Luo, J. Dai, Y. Yao, M. Zhu, E. Hitz, Y. Tang, Y. Chen, V.L. Sprenkle, X. Li, L. Hu, Adv. Energy Mater., 6 (2016) 1600377.

[116] V. Selvamani, R. Ravikumar, V. Suryanarayanan, D. Velayutham, S. Gopukumar, Electrochim. Acta, 190 (2016) 337-345.

[117] D.C. Qin, F. Zhang, S.Y. Dong, Y.Z. Zhao, G.Y. Xu, X.G. Zhang, RSC Adv., 6 (2016) 106218-106224.

[118] D. Qin, S. Chen, J. Solid State Electrochem., (2016) 1-8.

[119] X. Meng, D. Deng, Chem. Mater., 28 (2016) 3897-3904.

[120] P. Liu, Y. Li, Y.-S. Hu, H. Li, L. Chen, X. Huang, J. Mater. Chem. A, 4 (2016) 13046-13052.

[121] B. Lin, Q. Li, B. Liu, S. Zhang, C. Deng, Nanoscale, 8 (2016) 8178-8188.

[122] Y.M. Li, Y.S. Hu, H. Li, L.Q. Chen, X.J. Huang, J. Mater. Chem. A, 4 (2016) 96-104.

[123] Y. Li, Y.-S. Hu, M.-M. Titirici, L. Chen, X. Huang, Adv. Energy Mater., 6 (2016) 1600659.

[124] H. Li, F. Shen, W. Luo, J. Dai, X. Han, Y. Chen, Y. Yao, H. Zhu, K. Fu, E. Hitz, L. Hu, ACS Appl. Mater. Inter., 8 (2016) 2204-2210.

[125] N.R. Kim, Y.S. Yun, M.Y. Song, S.J. Hong, M. Kang, C. Leal, Y.W. Park, H.-J. Jin, ACS Appl. Mater. Inter., 8 (2016) 3175-3181.

[126] Q. Jiang, Z. Zhang, S. Yin, Z. Guo, S. Wang, C. Feng, Appl. Surf. Sci., 379 (2016) 73-82.

[127] J. Górka, C. Vix-Guterl, C. Matei Ghimbeu, C, 2 (2016) 24.

[128] R.R. Gaddam, D.F. Yang, R. Narayan, K.V.S.N. Raju, N.A. Kumar, X.S. Zhao, Nano Energy, 26 (2016) 346-352.

[129] I. Elizabeth, B.P. Singh, S. Trikha, S. Gopukumar, J. Power Sources, 329 (2016) 412-421.

[130] Y. Zhou, X. Rui, W. Sun, Z. Xu, Y. Zhou, W.J. Ng, Q. Yan, E. Fong, ACS Nano, 9 (2015) 4628-4635.

[131] Y.S. Yun, K.Y. Park, B. Lee, S.Y. Cho, Y.U. Park, S.J. Hong, B.H. Kim, H. Gwon, H. Kim, S. Lee, Y.W. Park, H.J. Jin, K. Kang, Adv. Mater., 27 (2015) 6914-6921.

[132] G.Y. Xu, J.P. Han, B. Ding, P. Nie, J. Pan, H. Dou, H.S. Li, X.G. Zhang, Green Chemistry, 17 (2015) 1668-1674.

[133] Y.X. Wang, J. Yang, S.L. Chou, H.K. Liu, W.X. Zhang, D. Zhao, S.X. Dou, Nat Commun, 6 (2015) 8689.

[134] H. Wang, P. Hu, J. Yang, G. Gong, L. Guo, X. Chen, Adv. Mater., 27 (2015) 2348-2354.

[135] F. Shen, H. Zhu, W. Luo, J. Wan, L. Zhou, J. Dai, B. Zhao, X. Han, K. Fu, L. Hu, ACS Appl. Mater. Inter., 7 (2015) 23291-23296.

[136] X. Meng, P.E. Savage, D. Deng, Environ. Sci. Technol., 49 (2015) 12543-12550.

[137] J. Ding, H. Wang, Z. Li, K. Cui, D. Karpuzov, X. Tan, A. Kohandehghan, D. Mitlin, Energy & Environmental Science, 8 (2015) 941-955.

[138] X. Li, J. Liang, Z. Hou, Y. Zhu, Y. Qian, RSC Adv., 4 (2014) 50950-50954.

[139] J. Jin, S.J. Yu, Z.Q. Shi, C.Y. Wang, C.B. Chong, J. Power Sources, 272 (2014) 800-807.

[140] K.L. Hong, L. Qie, R. Zeng, Z.Q. Yi, W. Zhang, D. Wang, W. Yin, C. Wu, Q.J. Fan, W.X. Zhang, Y.H. Huang, J. Mater. Chem. A, 2 (2014) 12733-12738.

[141] H. Zhu, Z. Jia, Y. Chen, N. Weadock, J. Wan, O. Vaaland, X. Han, T. Li, L. Hu, Nano Lett., 13 (2013) 3093-3100.

[142] J. Ding, H. Wang, Z. Li, A. Kohandehghan, K. Cui, Z. Xu, B. Zahiri, X. Tan, E.M. Lotfabad, B.C. Olsen, D. Mitlin, ACS Nano, 7 (2013) 11004-11015.

[143] Z. Wang, L. Qie, L. Yuan, W. Zhang, X. Hu, Y. Huang, Carbon, 55 (2013) 328-334.

[144] D. Yan, C. Yu, X. Zhang, W. Qin, T. Lu, B. Hu, H. Li, L. Pan, Electrochimica Acta, 191 (2016) 385-391.

[145] M. Hankel, D.J. Searles, Phys Chem Chem Phys, (2016).

[146] Y. Hu, X. Sun, Chemically Functionalized Graphene and Their Applications in Electrochemical Energy Conversion and Storage, Advances in Graphene Science, InTech, Rijeka, 2013.

[147] D. Li, L. Zhang, H. Chen, J. Wang, L.-X. Ding, S. Wang, P.J. Ashman, H. Wang, J. Mater. Chem. A, 4 (2016) 8630-8635.

Chapter 3. Materials and methods

3.1 Materials and reagents

Table 3.1 represents a comprehensive list of the chemicals and reagents used for the preparation of electrode materials and batteries. The chemicals procured were used as received without any further treatment.

Table 3.1 List of chemicals and reagents used.

Name of the chemical	Company	Purity/Grade
Sodium Nitrate	Sigma Aldrich	AR
Hydrogen Peroxide	Merck	30 wt. % in H_2O
Potassium Permanganate	Merck	AR
Hydrogen Chloride	Merck	37 wt.% in H_2O
Sulphuric acid	Merck	98%
Ammonia	EMSURE	~28-30 wt. % in water
1-Methyl-2-pyrrolidinone	Sigma Aldrich	98.5 %
Poly(vinylidene fluoride)	Sigma Aldrich	-
Sodium perchlorate	Merck	> 98% pure
Ethylene carbonate	Sigma Aldrich	98%
Propylene carbonate	Sigma Aldrich	99.7 %
Fluoroethylene Carbonate	Sigma Aldrich	99%
Lithium hexafluorophosphate solution	Merck	(Battery grade)

Copper foil and nickel foam were purchased from Shenzhen Biyuan Electronic, Co. Ltd. China.

Experimental methods for the preparation of carbon materials are detailed out in their respective individual chapters.

3.2 Materials characterisation

3.2.1 Scanning electron microscope

Field emission scanning electron microscope measurements were carried out on JOEL 7001 electron microscope at 10-15 kV beam voltage with a spot size of 6-8. The sample to be observed were isolated onto a carbon tape placed on a stainless steel stub. The samples were then sputter coated with Iridium to provide a conductive pathway to the electrons.

3.2.2 Transmission electron microscope

High-resolution Transmission electron microscope JEOL 2100 was used to study the samples at an accelerating voltage of 200 kV. The samples were initially subjected to ultra-sonication followed by isolation onto a holey carbon grid. The grid was then carefully mounted onto the holder and inserted into the TEM for imaging. Energy dispersive X-ray mapping was also carried out to investigate the elemental composition of the sample.

3.2.3 X-ray diffraction

X-ray diffraction measurements were carried out on powdered samples using a CuKα radiation (wavelength λ=1.54056 Å) with a step size of 2 degrees per minute with a voltage of 40 KV and current of 30 mA with 2 theta ranging from 5 to 80°. Shimadzu diffractometer (XRD–6000, Tokyo, Japan) was used in reflection mode to perform the X-ray diffraction measurements.

3.2.4 X-ray photoelectron spectroscopy

X-ray photoelectron spectroscopy spectra were acquired on a Kratos Axis ULTRA X-ray photoelectron spectrometer with a 165 mm hemispherical electron energy analyzer and a monochromatic Al Kα (1486.6 eV) radiation at 225 W (15 kV, 15 mA). Samples were isolated onto a scotch tape and placed in ultra-high vacuum condition overnight in the XPS chamber prior to the characterisation. CASA XPS software was used to analyse the obtained data.

3.2.5 Raman spectroscopy

Raman spectra were collected using a Raman Spectrometer (Renishaw) with a 514 nm laser. The powdered samples were isolated onto a glass plate for the measurements. The obtained Raman spectra for carbon materials were analysed for its D-band and G-band respectively.

3.2.6 Nitrogen sorption analyses

Micromeritics Tristar II 3020 was used for the nitrogen sorption analysis. The samples were initially taken into the test-tube and were degassed at 100 °C overnight. Then the samples were then tested for nitrogen sorption at -196 °C at a relative pressure P/P_o of 0.00 to 0.99. The

specific surface area was calculated using the Brunauer-Emmett-Teller method. The total pore volumes were evaluated from the nitrogen volumes adsorbed at a relative pressure P/P_o of 0.99.

3.3 Electrode preparation and battery cell assembly

Typically, a slurry of 70% active material, 20% carbon black and 10 % polyvinylidene fluoride in *N*-methyl pyrrolidine was coated onto a copper foil current collector and then dried at 60 °C overnight in a vacuum oven (**Figure 3.1**). The obtained electrode, a polypropylene separator (for Lithium-ion batteries (LIB)), glass fiber (for sodium-ion batteries (NIB)), and Na/Li metal counter electrode were assembled into a 2032-type coin cell filled with an electrolyte in an Ar-filled glovebox with less than 0.1 ppm moisture and oxygen contents. For the LIB cells, 1 M $LiPF_6$ in ethylene carbonate and dimethyl carbonate in equal volume ratio was used as the electrolyte. For the NIB cells, 1 M $NaClO_4$ in an equal volume ratio of ethylene carbonate and propylene carbonate mixed with 0.3 wt% of fluoroethylene carbonate was used.

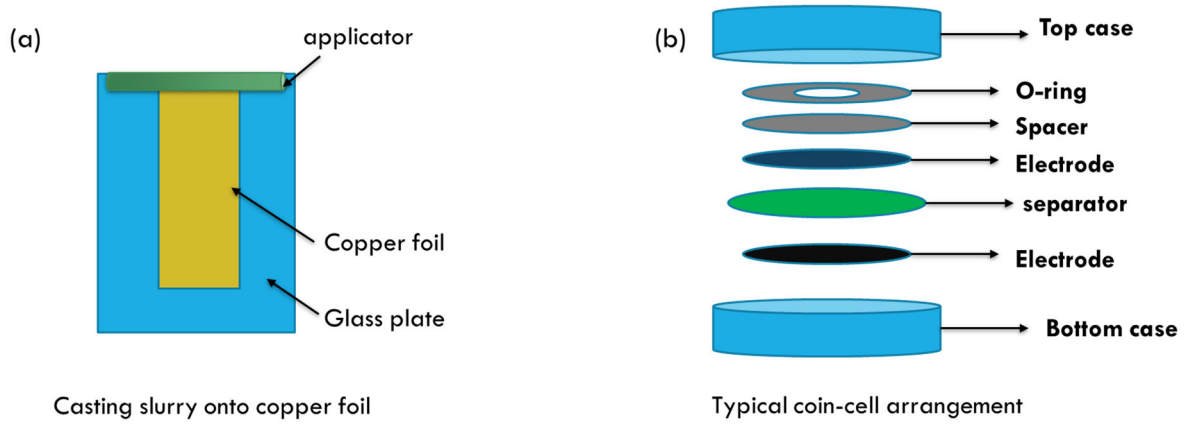

Figure 3.1 (a) Doctor blade method for casting the slurry onto the copper foil. (b) A typical setup for coin-cell battery assembly.

3.4 Electrochemical measurements

Electrochemical studies on the as-prepared carbon electrodes were carried out using cyclic voltammetry, galvanostatic charge/discharge and electrochemical impedance spectroscopy measurements.

3.4.1 Cyclic voltammetry

Cyclic voltammetry is one of the versatile and sensitive electrochemical characterization techniques used to analyze materials for battery development [1]. It is a potentiostatic method that helps to gain insights on the kinetics of reaction that happen at the electrode in a battery

[2]. It has also been increasingly used to interpret potential dependent process that happens at the interface. The shape of the cyclic voltammogram can help in narrowing down redox reactions to a particular type of electrochemical system thereby acting as a virtual fingerprint for reactions that occur [3]. Cyclic voltammetry measurements were carried out using a CHI-600D electrochemical workstation at a scan rate of 0.1 mVs^{-1} in the voltage domain of 0.005 to 3 V on a half cell with lithium/sodium metal as the counter electrode.

3.4.2 Galvanostatic charge-discharge

The cycling performance of the electrode were investigated using the galvanostatic charge-discharge method while maintaining a constant current density. Also, the rate tolerance of the electrode material was investigated by increasing the current densities and measuring the capacity retention upon reinstating the battery testing to its original current density. The charge/discharge measurements were performed using a Neware battery tester CT3008 in the voltage domain of 0.005 to 3 V on a half cell with lithium/sodium metal as the counter electrode.

3.4.3 Impedance spectroscopy

Electrochemical impedance spectroscopy (EIS) is an important electrochemical characterization tool that can provide information electronic and ionic conductivities in the electrode material. The impedance spectra were analyzed by fitting it into an equivalent circuit model. In general, the impedance spectra of the carbon electrode in lithium or sodium ion battery consists of one of more of the following components arising from the resistance from contacts (sum of all the electrical resistances), the double layer capacitance, the charge transfer resistance and an additional Warburg element associated with ion diffusion in carbon electrode [4, 5]. EIS measurements were performed using a CHI 660D electrochemical workstation in the frequency range of 100 kHz to 10 mHz.

3.5 References

[1] T. Reddy, D. Linden, Linden's Handbook of Batteries (4th Edition), McGraw-Hill Professional Publishing, New York, NY, USA, 2010.

[2] S. Hansen, E. Quiroga-González, J. Carstensen, H. Föll, Electrochim. Acta, 217 (2016) 283-291.

[3] J. Heinze, Angewandte Chemie International Edition in English, 23 (1984) 831-847.

[4] E.M. Lotfabad, J. Ding, K. Cui, A. Kohandehghan, W.P. Kalisvaart, M. Hazelton, D. Mitlin, ACS Nano, 8 (2014) 7115-7129.

[5] R.R. Gaddam, D.F. Yang, R. Narayan, K.V.S.N. Raju, N.A. Kumar, X.S. Zhao, Nano Energy, 26 (2016) 346-352.

Chapter 4. Biomass-derived carbon nanoparticles for sodium and lithium-ion batteries

-Published as *R.R. Gaddam et al.*, Biomass derived carbon nanoparticle as anodes for high performance sodium and lithium ion batteries, *Nano Energy*, 2016, 26, 346-352.

4.1 Introduction

Lithium-ion batteries (LIBs) with graphite as the anode are nowadays popularly used to power portable electronic devices. However, the limited theoretical capacity of graphite (372 $mAhg^{-1}$) [1, 2] hinders further development of new-generation LIBs for large-scale energy storage applications. On the other hand, lithium is geographically limited and politically sensitive. Increasing the utilization of lithium in energy storage will definitely increase the cost of LIBs in future [3]. Unlike lithium, sodium is naturally abundant. Sodium-ion batteries (NIBs) are promising alternative for LIBs. However, the graphite anode that is being used in LIBs fails to perform well in a NIB owing to the larger ionic radius of Na (0.102 nm) than that of Li (0.076 nm) and the thermodynamic instability of sodium-graphite system [4]. Therefore, an alternative anode with high performance and low cost are of paramount importance in the development of the NIB technology.

Electrode materials such as transition metal oxides [5-9], graphene [10], metal nitrides [11] and carbons [12-15] have been studied as anodes for NIBs. Carbon materials, especially hard carbon [16], have been shown to be the most promising anode for both NIBs and LIBs [17]. Production of carbon materials from biomass is highly attractive [18]. For battery applications, biomass-derived carbons can usually offer a higher capacity than graphite because biomass intrinsically has desirable molecular structures and architectures, which are favorable for charge storage and transport [19]. Since the raw material is naturally available no tedious approaches need to be realized for material engineering, which itself is an economic solution [19].

Herein, a flame deposition method to synthesize carbon nanoparticles (CNPs) with coconut oil as the biomass precursor is presented. The coconut oil derived CNPs possessed graphitic domains and displayed a quasi-spherical morphology. The obtained CNPs were further treated with an oxidizing agent to modify the surface of the CNPs to be rich in carboxylic groups [20, 21]. The carbon samples were then tested as anode materials in both LIBs and NIBs. Tested against sodium, the CNPs and *c*-CNPs delivered a capacity of 277 and 278 $mAhg^{-1}$ at a current density of 100 mAg^{-1} in the second cycle. For LIBs, the discharge capacities of CNP and *c*-CNP were 741 and 742 $mAhg^{-1}$ respectively at a current density of 100 mAg^{-1} in the second cycle. The present work has the following advantages: (i) the precursor is cheap and widely available, (ii) the synthesis method is scalable, and (iii) the obtained carbons are dense and show good performance in both NIBs and LIBs.

4.2 Experimental section

4.2.1 Material preparation

100 g of coconut oil purchased from the local market was taken in a crucible with a cotton wick placed inside. The wick was lit to let incineration of coconut oil imbibed by capillary action. The crucible was then covered with a brass lid with holes to allow air circulation. The carbon nanoparticles (CNPs) in the form of soot deposited on the brass plate was collected. The CNPs were further carboxylated by refluxing in a piranha solution (caution: a highly exothermic mixture of H_2SO_4 and H_2O_2 in the ratio of 7:3) for 6 h and subsequently washed with copious amounts of ethanol and water, filtered and dried in a vacuum oven at 80 °C for 24 h to obtain *c*-CNPs.

4.2.2 Material characterization

X-Ray diffraction (XRD) was recorded on Bruker D8 Advance X-ray diffractometer with Ni-filtered Cu Kα radiation (λ = 1.54056 Å; 40 kV, 30 mA) at a scan rate of 2° min^{-1}. Nitrogen sorption isotherms were measured on a Tristar II 3020. All samples were degassed at 150 °C for 3 h prior to the measurement. Transmission electron microscopy (TEM) measurements were carried out on a JEOL 2100 at an acceleration voltage of 200 kV. Field emission scanning electron microscope measurements were taken on JEOL 7001. X-ray photoelectron spectroscopy (XPS) spectra were acquired on a Kratos Axis ULTRA X-ray photoelectron spectrometer with a 165 mm hemispherical electron energy analyzer and a monochromatic Al Kα (1486.6 eV) radiation at 225 W (15 kV, 15 mA). Raman spectra were collected using a Raman Spectrometer (Renishaw) with a 514 nm laser.

4.2.3 Electrochemical testing

Typically, a slurry of 70% active material, 20% carbon black and 10 % polyvinylidene fluoride (PVDF) in *N*-methyl pyrrolidine (NMP) was coated onto a copper foil current collector (~1.5 mg of active material on each electrode) and then dried at 60 °C overnight in a vacuum oven. The obtained electrode, a polypropylene separator or glass fibre, and Na/Li metal counter electrode were assembled into a 2032-type coin cell filled with an electrolyte in an Ar-filled glovebox with sub-0.1 ppm water and oxygen contents. For the LIB cells, 1 M $LiPF_6$ in ethylene carbonate and dimethyl carbonate (1:1) was used as the electrolyte. For the NIB cells, 1 M $NaClO_4$ in an equal volume ratio of ethylene carbonate and propylene carbonate mixed with 0.3 wt% of fluoroethylene carbonate was used. Cyclic voltammetry was carried out using

a CHI-600D electrochemical workstation at a scan rate of 0.1 mV s^{-1} in the voltage domain of 0.005 to 3 V. The charge/discharge measurements were performed using a Neware battery tester CT3008. Electrochemical impedance spectroscopy measurements were also performed using a CHI 660D electrochemical workstation in the frequency range of 100 kHz to 10 mHz.

4.3 Results and discussion

Figures 4.1a and 4.1b show the FESEM and TEM images of CNPs with a quasi-spherical morphology and particle size ranging from 40 to 50 nm. The CNPs upon treatment with piranha solution shows no obvious changes in morphology (**Figures 4.1c and 4.1d**). Pores within the particles are not obvious from the FESEM and TEM images.

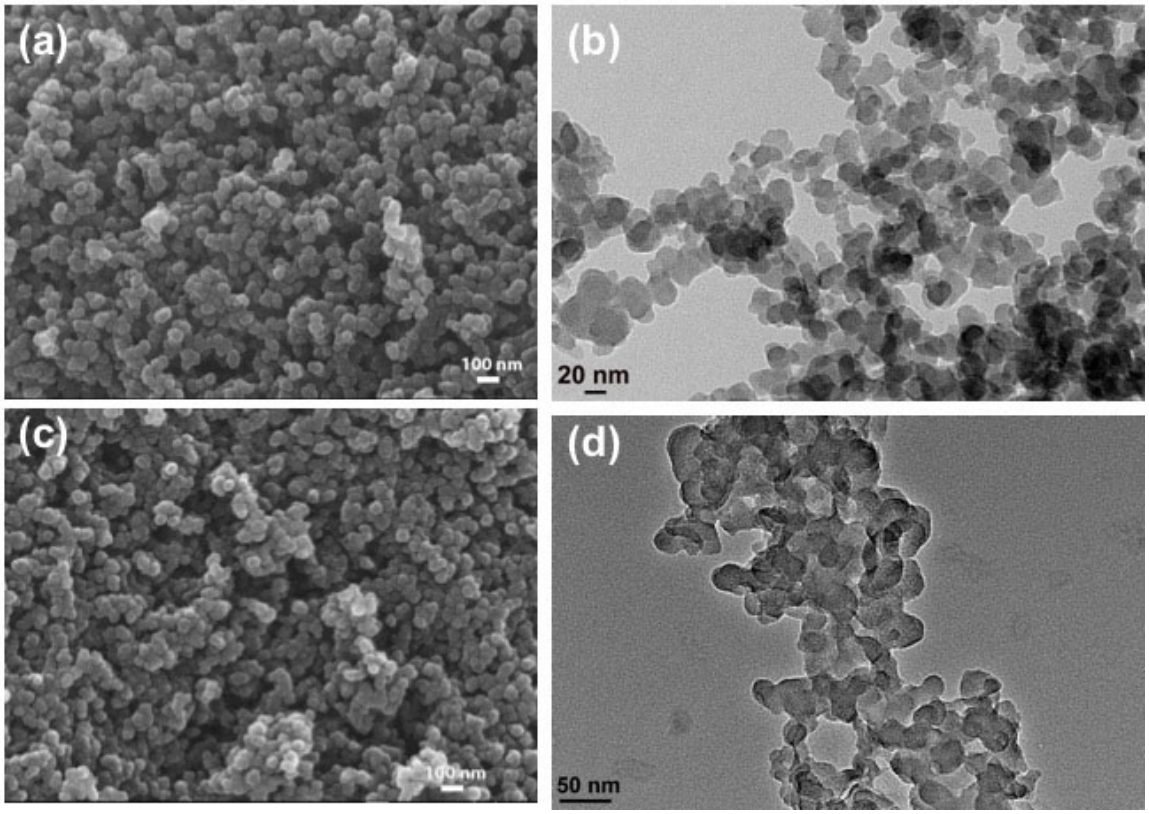

Figure 4.1 FESEM and TEM images of pristine carbon nanoparticles (CNPs) (a, c) and (b, d) carboxyl terminated carbon nanoparticle (*c*-CNPs).

The XRD patterns for CNPs and *c*-CNPs show two peaks at about 25° and 45° two theta, which correspond to (002) and (100) reflections of graphite, respectively (**Figure 4.2a**) [22]. An increase in crystallinity of *c*-CNP is evident from the XRD profile. This may be attributed to the nascent oxygen (originating from piranha solution), which generates a cascading effect,

favouring the disentanglement of carbon bonds and formation of oxygen sites for carboxyl bond establishment along with the removal of some amorphous carbons [23].

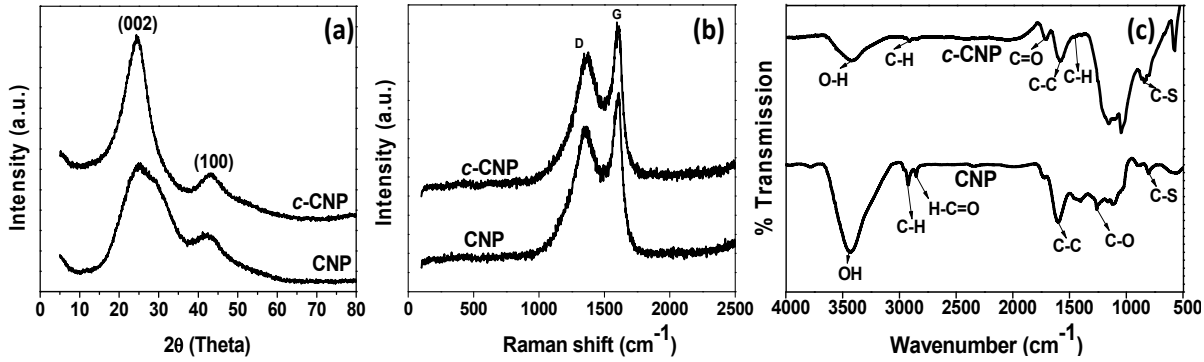

Figure 4.2 (a) X-ray diffraction profile (b) Raman spectroscopy (c) FTIR analysis of CNP and c-CNP.

The Raman spectra (**Figure 4.2b**) revealed two significant bands at around 1360 cm^{-1} and 1590 cm^{-1}, corresponding to the D-band and G-band of graphitic carbon, respectively. The D-band represents A_{1g} symmetry of disordered graphite, indicating the existence of crystalline domains in the samples [24, 25]. The G-band corresponds to the zone center symmetry of single crystalline graphite. The intensity ratio of D and G bands also can be used to determine the rate of disorder in the carbon. The I_D/I_G ratios of the samples were calculated to be around 0.854 for CNPs and 0.840 in the case of *c*-CNPs. No distinct differences were observed in the I_D/I_G ratios probably because piranha solution would dissolve active defect sites in the carbons without creating additional defects as observed previously [26]. The superimposition of different Raman modes as a result of the distribution cluster of nanoparticle with different sizes, result in a broader width in case of the CNPs, different from that of the *c*-CNP [27].

The Fourier-transform infrared (FTIR) spectra shown in **Figure 4.2c** exhibited a peak at 1726 cm^{-1} for *c*-CNP, which is due to the C=O stretching [28], confirming the presence of carboxyl groups. This peak could not be observed in CNP. Also, an additional peak at 1052 cm^{-1} corresponding to stretching frequency of primary alcohols is observable from *c*-CNP. Both CNP and *c*-CNP contain absorption peaks around 3430 cm^{-1} pertaining to –OH stretching, 2920 cm^{-1} of –C-H- bond and 820 cm^{-1} of -C-S- bond. The C-S bond could possibly arise from ν C-S stretching [23]. The coconut oil contained Sulphur, which gave rise to the C-S bond formation in both CNP and *c*-CNP samples.

The nitrogen adsorption/desorption isotherms and the corresponding pore size distribution curves computed using the Barrett–Joyner–Halenda (BJH) method [29] for both CNP and *c*-CNP are shown in **Figure S4.1**. The obtained isotherms show the existence of both micropores

and mesopores (type IV). An upward tendency at the high relative pressure region, P/P_o~0.9-1, can be attributed to the macropores formed between carbon particles [30]. Though the above statement holds true for the as prepared carbon materials, *c*-CNP showed a positive shift from that of CNP showcasing the significant existence of micropores and mesopores. The surface area of *c*-CNP (133 m^2/g) is higher than that of the CNP (56 m^2/g), indicating the creation of pores during the oxidative treatment using piranha solution. The X–ray Photoelectron spectroscopy (XPS) results for CNP and *c*-CNP samples revealed atomic concentrations of carbon of 93.02 and 80.49 atm.%, oxygen 6.64 and 17.06 atm.%, and sulfur 0.34 and 2.45 atm.%, respectively (**Figure S4.2**). The surface oxygen content upon piranha solution treatment was increased largely. Since the carbons have low surface area, it is not anticipated that oxygen and sulfur functionalities will have a substantial impact on the electrochemical performance [17, 31].

4.3.1 Electrochemical performance as a sodium-ion battery anode

Sodium-ion storage behavior in CNP and *c*-CNP was evaluated using cyclic voltammetry (CV) and galvanostaic charge-discharge (GCD) techniques. **Figure S4.3** shows the CV curves of CNP and c-CNP *vs* Na/Na^+ in the range of 0.005 to 3 V at a sweep rate of 0.1 mV s^{-1}. The CV curves reveal a strong cathodic peak at around 1.0 V in both CNP and *c*-CNP corresponding to the electrolyte decomposition, leading to the formation of solid electrolyte interphase (SEI) on the surface of the electrode [32, 33]. This peak disappeared in the subsequent cycles, indicating that the formation of the SEI occurred mostly in the initial discharge. A redox peak near 0 V similar to that observed during lithium insertion [2], endorse the sodium insertion and de-insertion in the interlayer of the graphitic domains present in the as prepared carbons. The shape of the CV curve being nearly rectangular in nature in the whole voltage range is indicative of the capacitive storage behavior of sodium ions [34]. It may be inferred that sodium-ion interaction with the anode material predominantly takes place by physical interaction, along with some redox reactions due to the interaction between sodium ions and oxygen containing functional groups during the charge-discharge process [35]. Notably, the CV curves overlapped after the initial cycle, indicating the reversible interaction of sodium-ion with the as prepared carbons.

Figure 4.3a and 4.3d shows the GCD curves of CNP and *c*-CNPs. An initial discharge capacity of 507 and 733 mA g^{-1} for CNP and *c*-CNPs respectively was obtained at a current density of 100 mAh g^{-1} with a coulombic efficiency of 49 and 34% (**Figure 4.3b** and **4.3e**). Such large

capacity loss and low initial coulombic efficiency is generally observed in carbon materials due to the decomposition of electrolytes on the surface of active site [33], formation of SEI on the electrode surface, side reactions on the electrode surface and trapping of sodium-ions in the voids between the carbon particles [34]. The coulombic efficiency improves to about 88% in the second cycle and stabilizes at more than 96% in the tenth cycle owing to the structural stability of the as prepared carbon materials upon cycling. These observations corroborate with that of CV curves. At the 2nd cycle, the CNP and *c*-CNP show a specific capacity of 278 and 277 mAh g^{-1} respectively. Upon repeated cycling, the coulombic efficiency is increased to near 100% and a capacity of 198 and 203 mAh g^{-1} can still be retained at the 50th cycle (**Table S4.1**). The discharge capacity of both samples outperformed most of the carbon materials previously reported (**Table 4.1**).

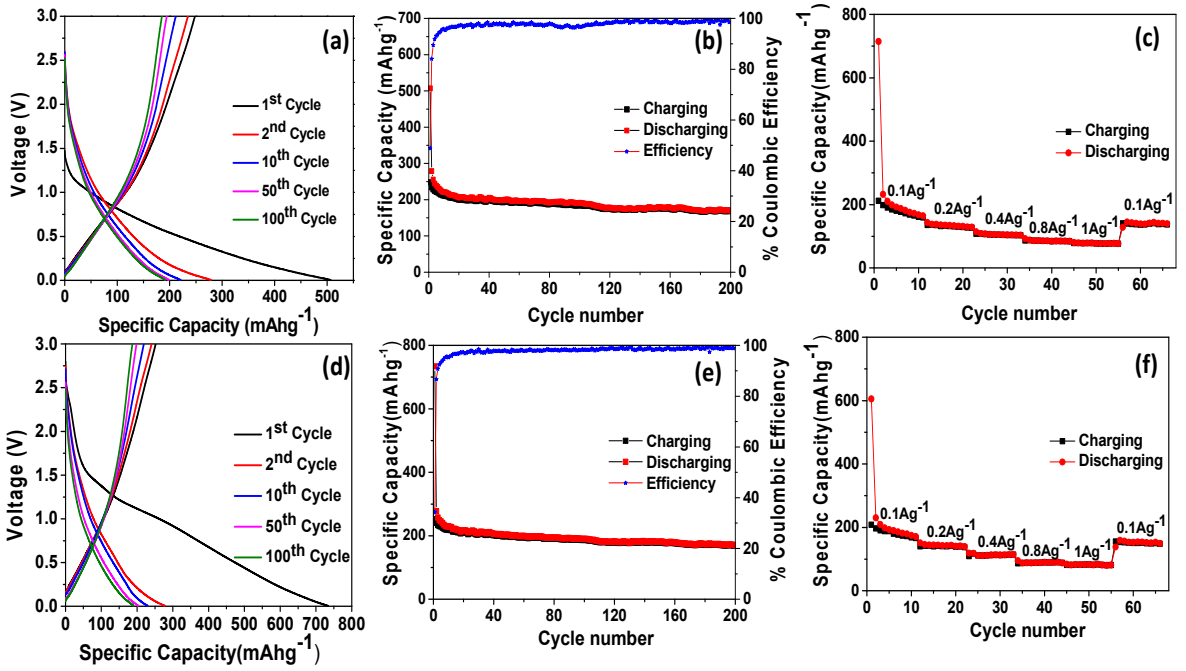

Figure 4.3 Electrochemical performance of CNP and *c*-CNP tested against sodium: charge-discharge curves (a, d), cycling stability (b, e), and rate capability (c, f).

The rate performance of electrodes CNP and *c*-CNP was evaluated with current densities ranging from 100 to 1000 mA g^{-1}, and the results are shown in **Figure 4.3c** and **4.3f**. For sample CNP, specific capacities of 135, 107, 87 and 78 mAh g^{-1} were obtained at current densities of 200, 400, 800, and 1000 mA g^{-1}, respectively. Similarly, electrode *c*-CNPs delivered discharge capacities of 140, 109, 87 and 82 mAh g^{-1} at current densities of 200, 400, 800 and 1000 mA g^{-1}, respectively. At higher current densities, the capacity is mainly due to the diffusion of sodium ion in and out the solid electrode.

Table 4.1 Comparison of electrochemical performance of carbon nanoparticles prepared in this work with other carbon electrode materials

Material	Initial Coulombic Efficiency (%)	Discharge Capacity (mAh g^{-1}) (Cycle 2)	Reference
CNP	49	278 at 100 mA g^{-1}	(this work)
c-CNP	34	277 at 100 mA g^{-1}	(this work)
Hard carbon particles	78	250 at 25 mA g^{-1}	[36]
Templated carbon	20	180 at 74 mA g^{-1}	[37]
Carbon fibers	46	ca. 350 at 50 mA g^{-1}	[38]
Graphene nanosheets	NA	220 at 30 mA g^{-1}	[39]
Carbon nanotubes	NA	82 at 30 mA g^{-1}	[39]
Nitrogen-doped carbon nanofibers	64	293 at 50 mA g^{-1}	[40]
Carbon microspheres	NA	202 at 30 mA g^{-1}	[41]
Highly disordered carbon	57.6	255 at 100 mA g^{-1}	[13]
Banana peel derived carbon	71	371 at 50 mA g^{-1}	[17]
Nanocellular carbon	NA	152 at 100 mA g^{-1}	[42]

Figure S4.4 shows the Nyquist plots of the carbon electrodes. A straight line in the low frequency region along with a depressed semicircle in the high frequency region can be seen. The impedance spectra were modelled with equivalent circuits, which are depicted in **Figure S4.5**, where R_e represents the resistance arising from contacts (sum of all the electrical resistances), C_{Lc} represents the double layer capacitance, R_c is the charge transfer resistance, Z_w is the Warburg element associated with ion diffusion in carbon electrode [17]). The SEI formation at the electrode surface results in a resistance and a capacitance named as C_{SF} and R_{SF} [17], respectively. The numerical values obtained from modelling are represented in the

Table S4.2. It can be noted that the charge-transfer resistance is higher in the case of electrode CNP. The overall resistance R_c+R_{SF} of *c*-CNP is much less as compared to CNP as observed from the impedance spectroscopy. However, with respect to performance both the batteries delivered similar capacitance indicating that the effect of carboxyl group is negligible. Overall both CNP and *c*-CNP perhaps because of the high density of the samples in turn delivers a high capacity.

Table 4.1 compares the performance of CNP and *c*-CNP vs Na/Na^+ with that of the literature. Carbons included in comparison are hard carbon particles [36], templated carbon [37], carbon fibers [38], graphene nanosheets [39], carbon nanotubes [39], nitrogen-doped carbon nanofibers [40], carbon microspheres [41], highly disordered carbon [13], banana peel derived pseudographite [17] and nanocellular carbon [42]. The performance of as prepared carbons is comparable with that of highly disordered carbons[13] whose discharge capacity is about 255 at 100 mAg^{-1}. The carbons reported in the present work has a highly reversible capacity, good cycling performance and high rate capability when tested against sodium, as compared to the previous reports.

4.3.2 Electrochemical performance as a lithium-ion battery anode

The obtained carbon materials were also evaluated as an anode for LIBs. The CV curves of CNP and *c*-CNP measured between 0.005 to 3 V with a sweep rate of 0.1 mVs^{-1} are shown in **Figure S4.6**. The cathodic peak at around 0.76 V relates to the electrolyte decomposition on the surface of the electrode, leading to the formation of SEI [4]. The other peak at ~1.5 V corresponds to the reaction of lithium with some functional groups present on the carbon surface as observed previously [43]. A sharp reduction peak near 0 V can be attributed to the lithium intercalation with carbons representing sharp diffusion path of lithium ions [44]. After the first cycle, the CV curve overlaps on each other indicating the reversibility of lithium storage in the electrodes.

The charge-discharge curves (**Figure 4.4a** and **4.4d**) show a slope from ~0 to 1.5 V, corresponding to the lithium deintercalation from the graphitic domains, and the slope above 1.5 V can be ascribed to the extraction of lithium from defect sites with higher energies like vacancies as observed previously [43, 45]. Both CNP and *c*-CNP exhibited a high discharge capacity of 1330 and 1231 mAh g^{-1} during the initial cycle, but with a poor coulombic efficiency which was about 50 and 55% for CNP and *c*-CNP, respectively. It is reasonable to assume that the degree of irreversible trapping of lithium within the bulk of the carbon would

affect the first cycle coulombic efficiency values, due to the formation of SEI on the surface of electrode [17]. Such capacity loss in the initial cycles is common amongst carbon materials.

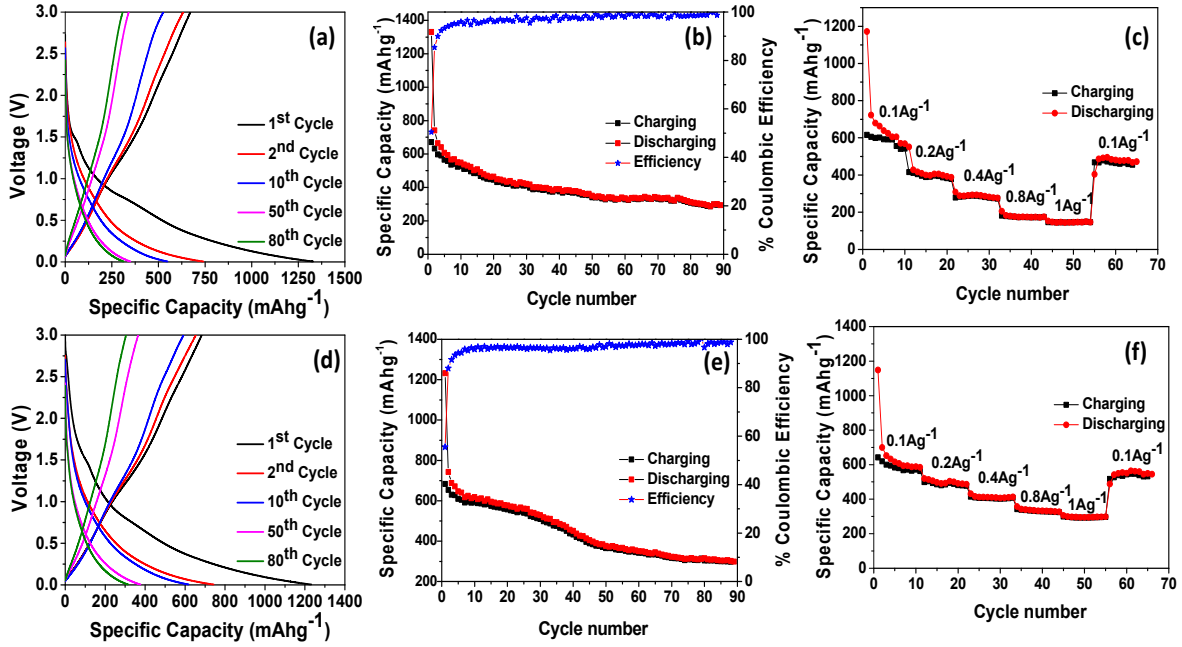

Figure 4.4 Electrochemical performance of CNP and *c*-CNP tested against lithium: charge-discharge curves (a, d), cyclic stability (b, e), and rate capability (c, f).

The CNP and *c*-CNP showed reversible capacities of 741 and 742 mAh g^{-1} respectively at the 2nd cycle and after 20 cycles the capacities became 464 and 577 mAh g^{-1} respectively i.e., 37% and 22% capacity losses (**Table S4.3**). These results are in sharp contrast when compared to the performance of the as prepared carbon materials in NIBs, where no distinction in the cycling profile was observable. It was found that *c*-CNP exhibited a greater capacity than CNP in LIBs during cycling [21].

The effect of the carboxyl group is more pronounced in the case of LIBs. It can be inferred from the cyclic performance that, *c*-CNP has a higher capacity retention as compared to that of CNP (**Figure 4.4b** and **4.4e**). This is credited to the presence of a carboxyl group that can provide a reversible lithium interaction [21]. This may be due to the formation of organic lithium salts with carboxyl groups ($-COO^- Li^+$) present on *c*-CNP which serve as a passive layer causing the reduction of irreversible capacity to a minimum value [20]. A noticeable difference is that the capacity of the carbon samples as an anode for LIBs is thrice that for NIBs. The carboxyl group has a substantial effect while testing against lithium, unlike sodium where the effect is negligible. This may be due to the larger size of sodium ion which might show lesser affinity to form such organic salts with carboxyl groups.

Table 4.2 Comparison of CNP & *c*-CNP with the state of art LIBs

Material	Initial Coulombic Efficiency (%)	Discharge Capacity (mAh g^{-1}) (2^{nd} cycle)	Reference
CNP	50	741 at 100 mA g^{-1}	**(this work)**
***c*-CNP**	55	742 at 100 mA g^{-1}	**(this work)**
Graphene	38	580 at 25 mA g^{-1}	**[46]**
Graphene nanosheets	NA	784 at 50 mA g^{-1}	**[47]**
Banana peel derived carbon	69	826 at 50 mA g^{-1}	**[17]**
Nitrogen rich porous carbon spheres	64	631 at 0.5 A g^{-1}	**[48]**
Graphene/carbon nanofibers	55	667 at 0.12 mA cm^{-2}	**[49]**
Nitrogen-doped graphitic carbon spheres	49	840 at 50 mA g^{-1}	**[50]**
Graphitic carbon spheres	NA	ca. 550 at 50 mA g^{-1}	**[50]**
Porous carbon nanofibers	66	ca. 491 at 50 mA g^{-1}	**[51]**
Carbon nanofibers	NA	483 at 50 mA g^{-1}	**[52]**
Carbon nanospheres	72	ca. 800 at 50 mA g^{-1}	**[53]**

The rate capability of CNP and *c*-CNP vs Li is shown in the **Figures 4.4c, 4.4f**. For sample CNP, specific capacities of 427, 309, 183 and 149 mAh g^{-1} were observed at current densities of 200, 400, 800 and 1000 mAg^{-1}, respectively. For sample *c*-CNP, a capacity of 499, 409, 336 and 295 mAh g^{-1} were obtained at current densities of 200, 400, 800 and 1000 mA g^{-1}. The higher rate capability and better reversibility can be seen from electrode *c*-CNP when compared to CNP which is again credited to the presence of carboxyl groups. The Nyquist plots for both CNP and *c*-CNP electrodes (**Figure S4.7**) displayed a depressed semi-circle spiked at the lower frequency region, similar to that of NIB. From the semicircle, $R_{SF}+R_C$ value can be obtained and are listed in **Table S4.3** [54]. It can be observed that the $R_{SF}+R_C$ is lower in case of *c*-CNP as compared with CNP, showing that the former has a faster charge transfer kinetics than the latter. A comparison with the state of art carbon is represented in **Table 4.2**. Carbons included for comparison are graphene [46], graphene nanosheets [47], banana peel derived carbon [17],

nitrogen-rich porous carbon spheres [48], graphene/carbon nanofibers [49], nitrogen-doped Graphitic carbon spheres [50], graphitic carbon spheres [50], porous carbon nanofibers [51], carbon nanofibers [52] and carbon nanospheres [53]. From the **Table 4.2,** it can be evaluated that the overall performance of the carbons prepared in this work is excellent in terms of cycling and capacity retention, only slightly inferior to that of the banana-peel-derived carbon [17].

4.4 Conclusion

Carbon nanoparticles prepared from coconut oil using the flame deposition method showed good performance as an anode in both sodium-ion and lithium-ion batteries. The carbon electrode exhibited a second-cycle discharge capacity of about 277 mAh g^{-1} in a sodium-ion battery and of about 741 mAh g^{-1} in a lithium-ion battery at a current density of 100 mA g^{-1}. The stability of the carbon nanoparticles against cycling can be significantly improved by surface modification. The electrode was found to be highly stable in terms of charge-storage and efficiency. The effect of the surface chemistry of the carbon nanoparticles on electrochemical performance was found to be distinctly observable in the case of lithium-ion batteries. However, no such effect was found in the case of NIBs. Hence, different chemistries seem to be present for the interactions between carbon nanoparticles before and after treatment in lithium and sodium ion battery systems. This research showed that biomass-derived carbon nanoparticles are potential anode materials for high-performance batteries.

4.5 References

[1] E. Peled, C. Menachem, D. Bar-Tow, A. Melman, J. Electrochem. Soc., 143 (1996) L4-L7.

[2] Y. Cao, L. Xiao, X. Ai, H. Yang, Electrochemical and solid-state lett., 6 (2003) A30-A33.

[3] Y. Kim, K.H. Ha, S.M. Oh, K.T. Lee, Chem.-A Eur. J., 20 (2014) 11980-11992.

[4] D. Stevens, J. Dahn, J. Electrochem. Soc., 148 (2001) A803-A811.

[5] L. Wu, D. Buchholz, D. Bresser, L. Gomes Chagas, S. Passerini, J. Power Sources, 251 (2014) 379-385.

[6] R. Alcántara, M. Jaraba, P. Lavela, J.L. Tirado, Chem. Mater., 14 (2002) 2847-2848.

[7] H. Xiong, M.D. Slater, M. Balasubramanian, C.S. Johnson, T. Rajh, J. Phys. Chem. Lett., 2 (2011) 2560-2565.

[8] Y. Xu, E. Memarzadeh Lotfabad, H. Wang, B. Farbod, Z. Xu, A. Kohandehghan, D. Mitlin, Chem. Comm., 49 (2013) 8973-8975.

[9] K.-T. Kim, G. Ali, K.Y. Chung, C.S. Yoon, H. Yashiro, Y.-K. Sun, J. Lu, K. Amine, S.-T. Myung, Nano Lett., 14 (2014) 416-422.

[10] L. David, R. Bhandavat, G. Singh, ACS Nano, 8 (2014) 1759-1770.

[11] X. Li, M.M. Hasan, A.L. Hector, J.R. Owen, J. Mater. Chem. A, 1 (2013) 6441-6445.

[12] Q. Fan, W. Zhang, J. Duan, K. Hong, L. Xue, Y. Huang, Electrochim. Acta, 174 (2015) 970-977.

[13] X. Zhou, Y.G. Guo, ChemElectroChem, 1 (2014) 83-86.

[14] E. Irisarri, A. Ponrouch, M. Palacin, J. Electrochem. Soc., 162 (2015) A2476-A2482.

[15] H. Hou, C.E. Banks, M. Jing, Y. Zhang, X. Ji, Adv. Mater., 27 (2015) 7861-7866.

[16] Y. Bai, Z. Wang, C. Wu, R. Xu, F. Wu, Y. Liu, H. Li, Y. Li, J. Lu, K. Amine, ACS Appl. Mater. Inter., 7 (2015) 5598-5604.

[17] E.M. Lotfabad, J. Ding, K. Cui, A. Kohandehghan, W.P. Kalisvaart, M. Hazelton, D. Mitlin, ACS Nano, 8 (2014) 7115-7129.

[18] P. Kalyani, A. Anitha, Int. J. Hydrog. Energy, 38 (2013) 4034-4045.

[19] Y. Yao, F. Wu, Nano Energy, 17 (2015) 91-103.

[20] Y. Ein-Eli, V.R. Koch, J. Electrochem. Soc., 144 (1997) 2968-2973.

[21] Z. Xie, Z. Yu, W. Fan, G. Peng, M. Qu, RSC Adv., 5 (2015) 90041-90048.

[22] R.R. Gaddam, D. Vasudevan, R. Narayan, K.V.S.N. Raju, RSC Adv., 4 (2014) 57137-57143.

[23] R.R. Gaddam, S. Kantheti, R. Narayan, K.V.S.N. Raju, RSC Adv., 4 (2014) 23043-23049.

[24] D.S. Knight, W.B. White, J. Mater. Res., 4 (1989) 385-393.

[25] N.A. Kumar, H.-J. Choi, Y.R. Shin, D.W. Chang, L. Dai, J.-B. Baek, ACS Nano, 6 (2012) 1715-1723.

[26] K.J. Ziegler, Z. Gu, H. Peng, E.L. Flor, R.H. Hauge, R.E. Smalley, J. Am. Chem. Soc., 127 (2005) 1541-1547.

[27] G.X. Chen, M.H. Hong, T.C. Chong, H.I. Elim, G.H. Ma, W. Ji, J. Appl. Phys., 95 (2004) 1455-1459.

[28] J. Chen, M.A. Hamon, H. Hu, Y. Chen, A.M. Rao, P.C. Eklund, R.C. Haddon, Science, 282 (1998) 95-98.

[29] K.S. Sing, J. Rouquerol, Adsorption at the gas-solid and liquid-solid interface, Elsevier, 2009.

[30] G. Xu, J. Han, B. Ding, P. Nie, J. Pan, H. Dou, H. Li, X. Zhang, Green Chem., 17 (2015) 1668-1674.

[31] K. Nanjundan Ashok, B. Jong-Beom, Nanotechnology, 26 (2015) 492001.

[32] S. Kajiyama, L. Szabova, K. Sodeyama, H. Iinuma, R. Morita, K. Gotoh, Y. Tateyama, M. Okubo, A. Yamada, ACS Nano, 10 (2016) 3334-3341.

[33] Y. Cao, L. Xiao, M.L. Sushko, W. Wang, B. Schwenzer, J. Xiao, Z. Nie, L.V. Saraf, Z. Yang, J. Liu, Nano Lett., 12 (2012) 3783-3787.

[34] H.L. Wang, W.H. Yu, J. Shi, N. Mao, S.G. Chen, W. Liu, Electrochim. Acta, 188 (2016) 103-110.

[35] T. Yang, T. Qian, M. Wang, X. Shen, N. Xu, Z. Sun, C. Yan, Adv. Mater., 28 (2016) 539-545.

[36] S. Komaba, W. Murata, T. Ishikawa, N. Yabuuchi, T. Ozeki, T. Nakayama, A. Ogata, K. Gotoh, K. Fujiwara, Adv. Funct. Mater., 21 (2011) 3859-3867.

[37] S. Wenzel, T. Hara, J. Janek, P. Adelhelm, Energy Environ. Sci., 4 (2011) 3342.

[38] L. Fu, K. Tang, K. Song, P.A. van Aken, Y. Yu, J. Maier, Nanoscale, 6 (2014) 1384-1389.

[39] X.-F. Luo, C.-H. Yang, Y.-Y. Peng, N.-W. Pu, M.-D. Ger, C.-T. Hsieh, J.-K. Chang, J. Mater. Chem. A, 3 (2015) 10320-10326.

[40] J. Zhu, C. Chen, Y. Lu, Y. Ge, H. Jiang, K. Fu, X. Zhang, Carbon, 94 (2015) 189-195.

[41] T. Chen, L. Pan, T. Lu, C. Fu, D.H.C. Chua, Z. Sun, J. Mater. Chem. A, 2 (2014) 1263-1267.

[42] Y. Shao, J. Xiao, W. Wang, M. Engelhard, X. Chen, Z. Nie, M. Gu, L.V. Saraf, G. Exarhos, J.-G. Zhang, J. Liu, Nano Lett., 13 (2013) 3909-3914.

[43] K. Tang, R.J. White, X. Mu, M.M. Titirici, P.A. van Aken, J. Maier, ChemSusChem, 5 (2012) 400-403.

[44] M. Kakunuri, C.S. Sharma, Electrochim. Acta, 180 (2015) 353-359.

[45] N.A. Kaskhedikar, J. Maier, Adv. Mater., 21 (2009) 2664-2680.

[46] A. Kumar, A.L.M. Reddy, A. Mukherjee, M. Dubey, X. Zhan, N. Singh, L. Ci, W.E. Billups, J. Nagurny, G. Mital, P.M. Ajayan, ACS Nano, 5 (2011) 4345-4349.

[47] E. Yoo, J. Kim, E. Hosono, H.-s. Zhou, T. Kudo, I. Honma, Nano Letters, 8 (2008) 2277-2282.

[48] D. Li, L.-X. Ding, H. Chen, S. Wang, Z. Li, M. Zhu, H. Wang, J. Mater. Chem. A, 2 (2014) 16617-16622.

[49] Z.-J. Fan, J. Yan, T. Wei, G.Q. Ning, L.J. Zhi, J.C. Liu, D.X. Cao, G.L. Wang, F. Wei, ACS Nano, 5 (2011) 2787-2794.

[50] S.-X. Wang, S. Chen, Q. Wei, X. Zhang, S.Y. Wong, S. Sun, X. Li, Chemistry of Materials, 27 (2015) 336-342.

[51] J. Liwen, Z. Xiangwu, Nanotechnology, 20 (2009) 155705.

[52] L. Ji, X. Zhang, Electrochemistry Communications, 11 (2009) 684-687.

[53] Y. Chen, Z. Lu, L. Zhou, Y.-W. Mai, H. Huang, Nanoscale, 4 (2012) 6800-6805.

[54] P. Kollu, P.R. Kumar, C. Santosh, D.K. Kim, A.N. Grace, RSC Advances, 5 (2015) 63304-63310.

4.6 Supplementary information

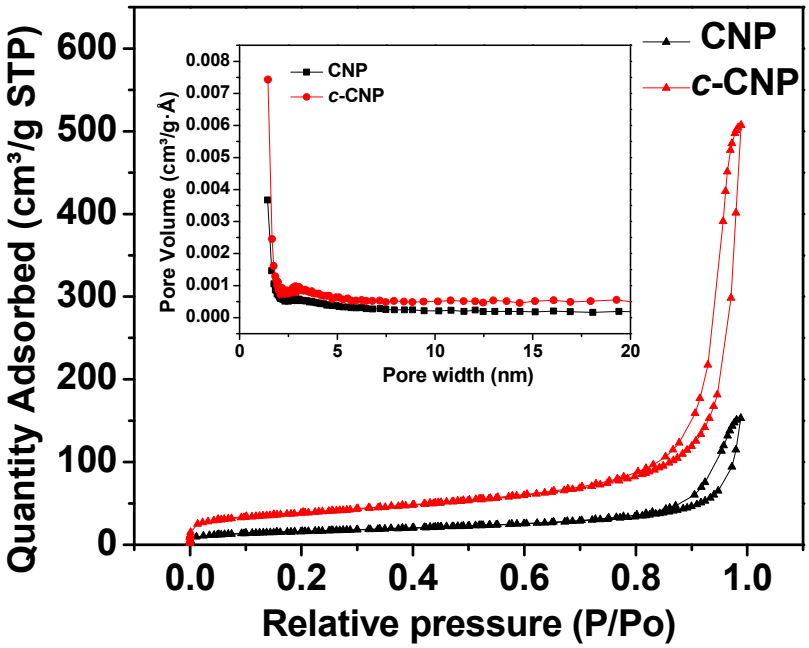

Figure S4.1 Nitrogen adsorption and desorption isotherms and pore-size distribution curves (inset) calculated using the Barrett-Joyner-Halenda (BJH) method.

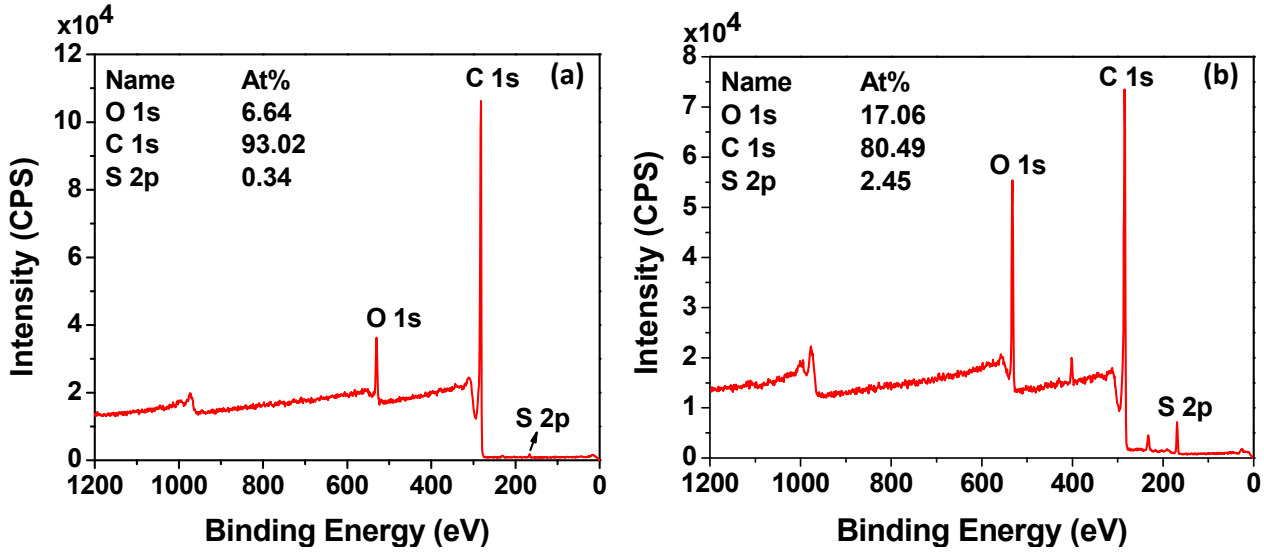

Figure S4.2 XPS survey scans of (a) CNP and (b) *c*-CNP

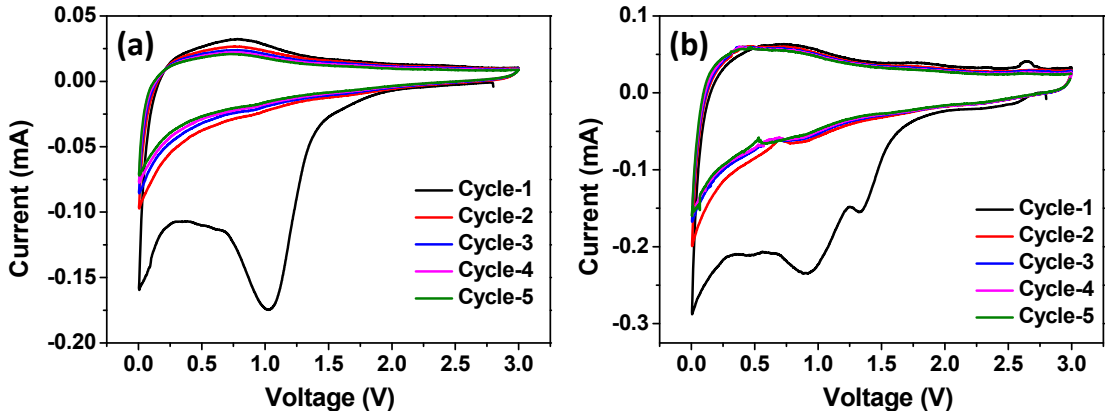

Figure S4.3 Cyclic voltammetry curves of (a) CNP and (b) *c*-CNP *vs* Na

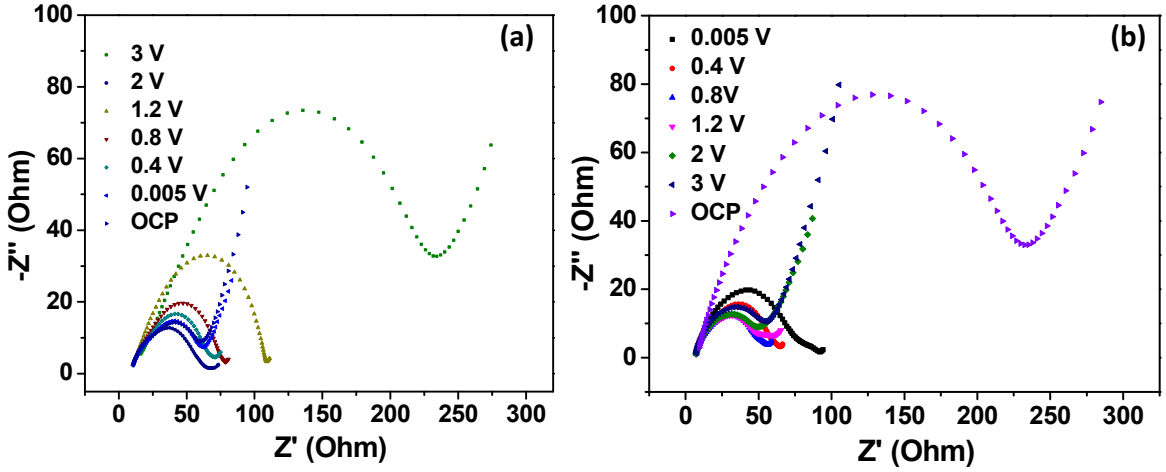

Figure S4.4 Experimental electrochemical impedance spectroscopy of (a) CNP and (b) *c*-CNP in sodium ion battery.

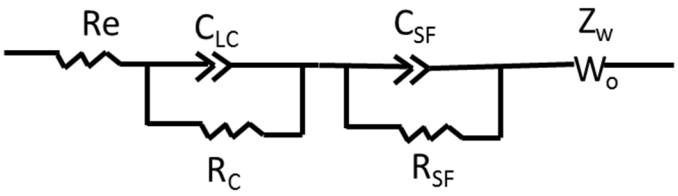

Figure S4.5 Equivalent circuit used in the simulation of electrochemical impedance.

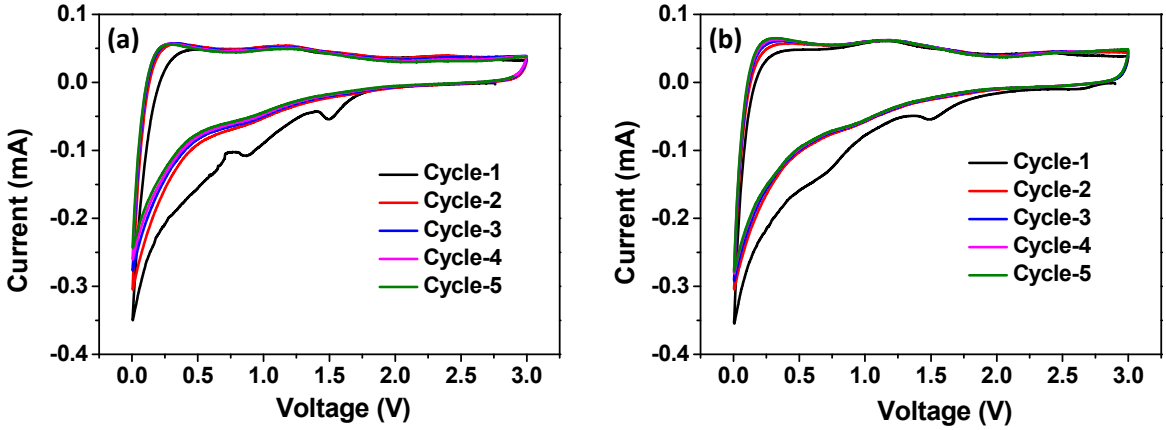

Figure S4.6 Cyclic voltammetry plots for (a) CNP and (b) *c*-CNP vs Li

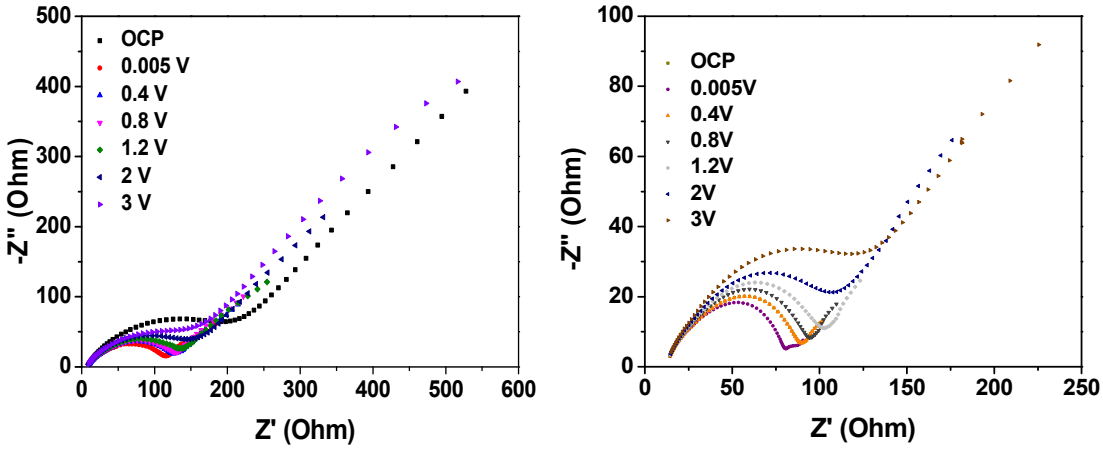

Figure S4.7 Experimental electrochemical impedance spectroscopy of CNP and *c*-CNP in lithium ion battery.

Table S4.1 Specific capacity of CNP and *c*-CNP, *vs* Na. Samples were tested at a current density of 100 mAg^{-1}

Samples	Cycle 2 ($mAh\ g^{-1}$)	Cycle 20 ($mAh\ g^{-1}$)	Cycle 30 ($mAh\ g^{-1}$)	Cycle 50 ($mAh\ g^{-1}$)
CNP	278	206	203	198
c-CNP	277	217	207	203

Table S4.2 Resistance values simulated by modelling the experimental impedance. The equivalent circuit is shown in Figure S4.5.

Samples	R_e	R_{c+} R_{SF}
CNP (vs Na)	9.8	188.29
c-CNP (vs Na)	18.1	41.55
CNP (vs Li)	9.78	134.73
c-CNP (vs Li)	16.49	46.58

Table S4.3 Specific capacities of CNP and *c*-CNP *vs* Li. Samples were tested at a current density of 100 mAg^{-1}.

Samples	Initial capacity ($mAh\ g^{-1}$)	Cycle 2 ($mAh\ g^{-1}$)	Cycle 20 ($mAh\ g^{-1}$)
CNP	1330	741	464
c-CNP	1231	742	577

Chapter 5. Biomass derived carbon based binder-free anode for lithium-ion and sodium-ion batteries

-Published as *R. R. Gaddam et al.*, Carbon nanoparticle-based three-dimensional binder-free anode for rechargeable alkali-ion batteries, *Materials Today Energy*, 2018, 8, 29-36.

5.1 Introduction

Carbonaceous materials are good anode candidates for alkali-ion batteries because of their low cost, corrosion resistance, electrical conductivity, and mature technology for large-scale production [1]. Graphite is a common anode for lithium-ion batteries (LIBs) [2]. However, graphite is unsuitable as an anode for sodium-ion batteries (NIBs) because the ionic radius of sodium (0.102 nm) is much larger than that of lithium (0.076 nm) [3]. Recent research has shown that non-graphitizable hard carbons obtained from the biomass exhibit considerably high capacity for storing both lithium and sodium ions [4]. However, the electrode fabrication process using such materials involve preparation of a slurry, that contains an electrochemically active material, a binder and an electron-conductive additive. The binder such as poly(vinylidene)fluoride helps to integrate the active material and the conducting additive. Nevertheless, the presence of the binder can largely lower the electrochemical performance of a battery cell because it is electrochemically inactive [5, 6]. A binder-free electrode thus can provide a better performance and reduce the cost of the electrode.

Till date, fractal-like carbon soots from candle flame [7], mushroom derived carbons [8], and carbon derived from leaves [9] have been reported as binder-free anodes in LIBs or NIBs. However, most, if not all, of the reported electrodes suffer from mediocre capacity and/or stability. In addition, traditional electrodes might be incompetent in preventing the structural collapses during electrochemical reactions [6]. Thus, an inexpensive and scalable electrode design that can resist collapses and enhance the battery performance is desirable.

This work demonstrates a robust electrode design *via* self-assembly of carbon nanoparticles (CNPs) onto a three-dimensional (3D) Ni-foam using a simple yet very effective one-step flame deposition method. This design allows the flow of electrolyte throughout the electrode. In addition, the nickel foam substrate prevents the electrode architecture from deformation during cycling and the eradication of binder and conducting additive simplifies the electrode fabrication process, thus making the costs of electrode manufacturing low. The 3D electrode was tested as anode in both LIB and NIB cells. The anode delivered a specific discharge capacity of 764 mA h g^{-1} and 241 mA h g^{-1} in the second cycle when tested against lithium and sodium ions, respectively, at a current density of 50 mA g^{-1}. The 3D electrode displayed an exceptional cycling stability at high current rate (1 A g^{-1}) delivering a capacity of 664 mA h g^{-1} at the 500^{th} cycle in a LIB cell.

5.2 Experimental section

5.2.1 Material synthesis

Nickel foam was sonicated in a diluted hydrochloric acid solution followed by washing with ethanol and drying under vacuum. The foam was then cut into circles of ~15 mm in diameter. ~1-10 g of camphor was taken in a crucible and ignited in a well-aerated space. The nickel foam was held above the flame so as to deposit the soot uniformly on the surface of the foam, which was then directly used as an anode.

5.2.2 Material characterization

X-Ray diffraction (XRD) was recorded on Bruker D8 Advance X-ray diffractometer with Ni-filtered Cu Kα radiation (λ = 1.54056 Å; 40 kV, 30 mA) at a scan rate of 2^{o} min^{-1}. Transmission electron microscopy (TEM) measurements were taken on a JEOL 2100 at an acceleration voltage of 200 kV. Field-emission scanning electron microscopy (FESEM) measurements were taken on JEOL 7001. X-ray photoelectron spectroscopy (XPS) spectra were acquired on a Kratos Axis ULTRA X-ray photoelectron spectrometer with a 165-mm hemispherical electron energy analyzer and a monochromatic Al Kα (1486.6 eV) radiation at 225 W (15 kV, 15 mA). Fourier transform infrared (FTIR) spectrographs of the synthesized samples were recorded using a Thermo Nicolet Nexus 670 spectrometer. Raman spectra were collected using a Raman Spectrometer (Renishaw) with a 514 nm laser.

5.2.3 Electrochemical testing

The obtained anode placed on a copper foil, with a polypropylene (for LIB) or a glass fibre (for NIB) separator, and Na/Li metal counter electrode were assembled into a 2032-type coin cell filled with electrolytes, in an Ar-filled glovebox with < 0.1 ppm water and oxygen contents. For LIBs 1M $LiPF_6$ in an equal volume ratio of ethylene carbonate (EC) and dimethyl carbonate (DC) was used as the electrolyte. NIB electrolyte was 1M $NaClO_4$ in an equal volume ratio of ethylene carbonate (EC) and propylene carbonate (PC) mixed with 0.3wt% of fluoroethylene carbonate (FEC). Cyclic voltammetry was carried out using a CHI-600D electrochemical workstation at a scan rate of 0.2 mVs^{-1} in the voltage range 0.005–3 V. The galvanostatic charge-discharge measurements were performed using a Neware battery tester CT3008. Electrochemical impedance spectroscopy measurements were also performed using a CHI 660D electrochemical workstation in the frequency range of 100 kHz to 10 mHz.

5.3 Results and discussion

Figure 5.1a. shows a schematic representation of the CNPs flame deposited onto nickel foam using camphor, which is a naturally available terpene ketone that possesses methyl and carboxyl groups. The combustion of camphor leads to cleavages of the methyl groups, resulting in the formation of a reactive intermediate hexagonal and pentagonal carbon backbones [10]. These carbon backbones combine forming a nanoparticle [10, 11]. The CNPs produced from camphor were self-assembled onto the nickel foam (**Figure 5.1b**). The deposited nickel foam can be bent without any detachment of CNPs (**Figure 5.1c**).

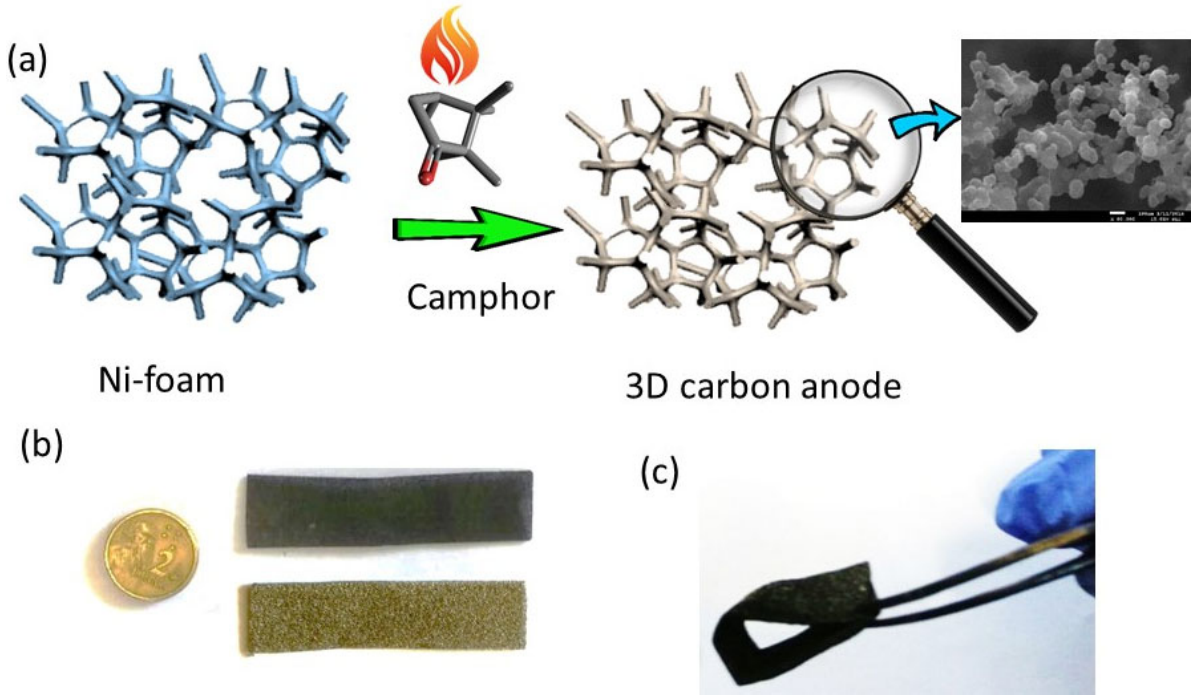

Figure 5.1 (a) Schematic for the preparation of three-dimensional carbon anode, (b) digital image of pristine nickel foam (below) and carbon nanoparticle assembled nickel foam (above), and (c) photograph of bent electrode revealing its mechanical flexibility.

Figure 5.2 shows the field-emission scanning electron microscope (FESEM) and transmission electron microscope (TEM) images, along with elemental mapping images. It can be seen that the CNPs take a quasi-spherical morphology with sizes ranging from 40 to 50 nm (Figures 5.2a-c). Local graphitic domains with an interlayer *d*-spacing of 0.34 nm were observed from the high-resolution TEM images (**Figure S5.1**). The uniformly deposited CNPs are interconnected with each other as visualised from the FESEM images (**Figure 5.2b**). The

energy dispersive X-ray (EDS) mapping images of the CNPs clearly indicate the presence of carbon and oxygen throughout the sample (**Figures 5.2d-f**).

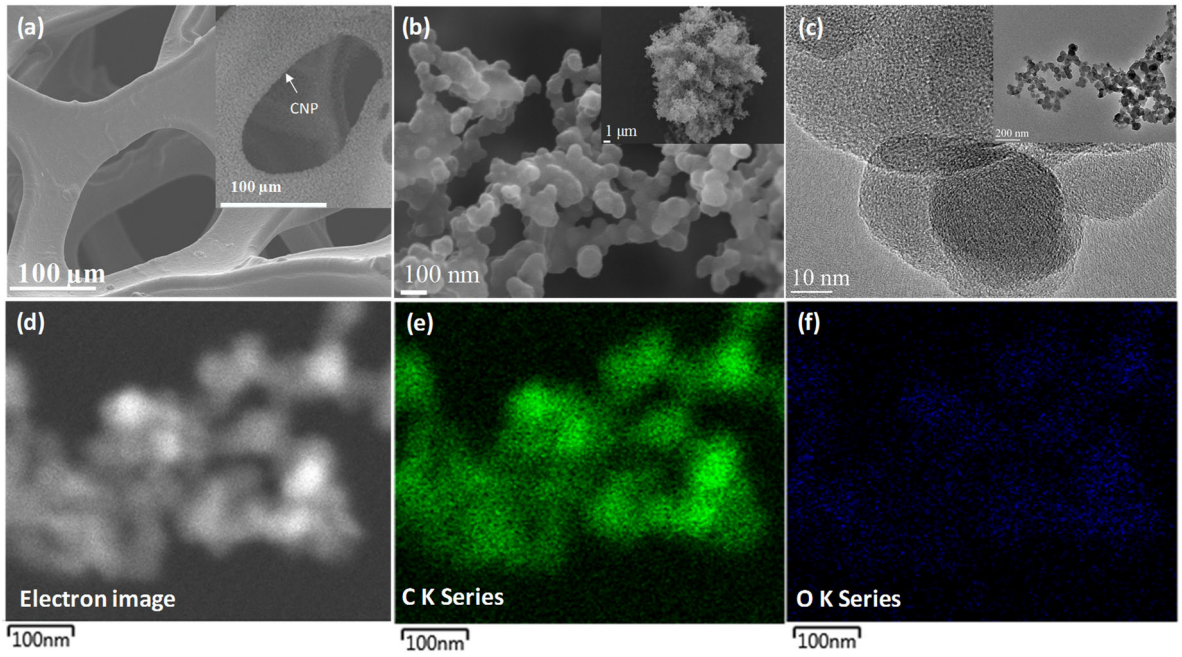

Figure 5.2 FESEM image of (a) pristine nickel foam (inset: CNP deposited nicked foam), (b) high resolution image of CNP (inset: overview of CNP); (c) TEM image of CNP (inset: an overview of the samples); (d) the scanning transmission electron microscope (STEM) image of CNPs. Energy dispersive X-ray elemental colour mapping images of (e) carbon and (f) oxygen in CNPs.

The X-ray diffraction patterns for the CNPs reveal two peaks at ~29° and ~42° 2θ, corresponding to (002) and (100) planes of graphite (**Figure 5.3a**) [12]. The peak at ~42° is relatively weak, indicating the presence of crystalline carbon or graphitic domains in the CNPs [13]. The *d*-spacing at ~29° (2θ) was around 0.34 nm, matching with the turbostratic structure [13], suggesting the presence of intermediate structure between graphite and amorphous carbon with turbostratic disorders [13]. The Raman spectra of the CNPs showed a pronounced D (defect) and G (graphite) band at 1364 and 1600 cm^{-1}, respectively (**Figure 5.3b**). The D-band corresponds to A_{1g} symmetry of disordered graphite and indicates the existence of nanocrystalline graphite. The G-band arises due to an ideal lattice vibration mode in E_{2g} symmetry [14, 15]. The peak intensity ratio of the two bands is $I_D/I_G = 0.68$, which indicates a fair degree of graphitization. The Fourier transform infrared (FTIR) spectra of CNPs showed

strong peaks at 3440 and 1620 cm^{-1} corresponding to the stretching and bending frequency of –OH (hydroxyl) group, indicating the presence of adsorbed moisture. Peaks at around 2934 and 2850 cm^{-1} correspond to the saturated –C-H stretching of $–CH_3$ and $–CH_2$ respectively. A stretching frequency at 1100 cm^{-1} can be assigned to the C-O (carboxyl) group (**Figure 5.3c**) [7, 16]. **Figure 5.3d** shows the elemental composition of the obtained CNPs, quantified using X-ray photoelectron spectroscopy (XPS) technique. The pronounced peaks at 287 and 532 eV correspond to C 1s (97.11 at %) and O 1s (2.89 at %), respectively. The high-resolution C1s spectrum was de-convoluted to C-C sp^2, C-C sp^3, C-O-C and C=O at binding energies of 284.4, 284.6, 286.25 and 287.77 eV, respectively. A π-π* peak with a dissymmetric shape (a broadening on the high-energy side) characteristic of graphitic carbons was also observed at 290.20 eV (**Figure 5.3e**). As shown in **Figure 5.3f**, the de-convoluted high-resolution XPS scan of O1s reveal peaks at 531.21, 532.55 and 533.81 eV corresponding to –OH, C-O-C and C=O respectively [17]. The oxygen content may be attributed to the thermally stable functional groups present in the CNPs except for those adsorbed on its surface pertaining to moisture.

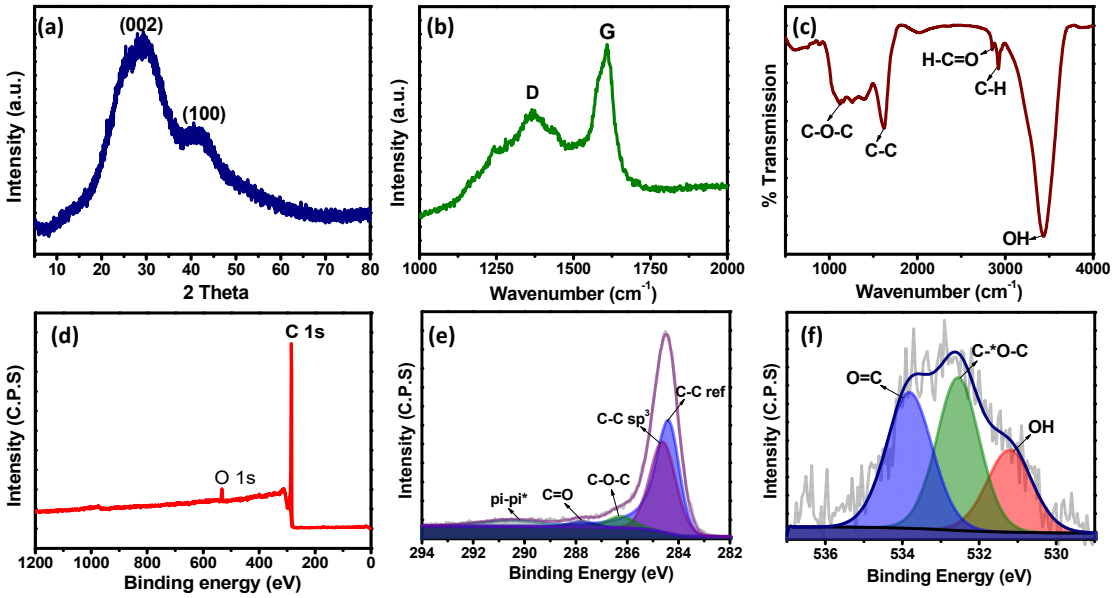

Figure 5.3 (a) XRD pattern, (b) Raman spectrum, (c) FTIR spectrum, (d) XPS survey, (e) high-resolution C1s and (f) O1s spectra of the CNPs.

To investigate the electrochemical performance, the obtained 3D binder-free electrodes were tested as anodes in LIBs. **Figure 5.4a** shows the cyclic voltammetry (CV) profiles for the 3D

anode recorded at a sweep rate of 0.2 mV s^{-1} in the voltage range of 0.005 to 3V. A cathodic peak at 0.34 V in the initial cycle corresponds to the degradation of electrolyte and the formation of solid electrolyte interphase (SEI) layer on the electrode surface [18]. The sharp reduction peak near 0 V represents the lithium-ion insertion and de-insertion within the graphitic domains present in the CNPs [19]. This sharpness in the reduction peak might indicate the shorter ion-diffusion pathway and faster kinetics of the electrode [7]. An anodic peak observed at 2.22 V may be attributed to the interaction of lithium-ion with some oxygen-containing functional groups. The corresponding reduction peaks were observed at 1.07 V. After the initial cycle, the CV curves overlapped indicating the system's reversibility.

The galvanostatic charge-discharge curve showed an initial discharge capacity of 1283 mA h g^{-1} and a charge capacity of 724 mA h g^{-1} at a current density of 50 mA g^{-1} (**Figure 5.4b**). The first cycle coulombic efficiency was around 56%. This loss in capacity during the initial cycle is due to the formation of a dense SEI layer on the surface of the electrode due to the irreversible reaction of the lithium-ions with CNPs and the oxygen-containing functional groups as observed in the cyclic voltammograms [20]. Despite the moderate coulombic efficiency in the first cycle, the electrodes exhibited nearly 97% in the 10^{th} cycle. As it can be seen in **Figure 5.4b**, the charge-discharge curve exhibited a slope from 0 to 1 V corresponding to lithium desorption from the disordered carbons. Further, a sloping plateau near 1.3 V in the discharge cycle and near 2.2 V in the charge cycle was observed. The slope above 1.3 V can be ascribed to the lithium-ion interactions at the vacancies and/or defect sites [21, 22]. To test the cycling performance of the battery, we charged and discharged the coin-cells anodes for 500 cycles at a current density of 1 A g^{-1}. As shown in **Figure 5.4c**, a specific discharge capacity of 485 mA h g^{-1} was observed in the second cycle. At the 500^{th} cycle, the coulombic efficiency was near 100%, with a discharge capacity of 664 mA h g^{-1}. An increasing trend in the specific capacity with progression in the cycling can be observed, suggesting the access of lithium-ions to the inaccessible areas of the electrode [8]. To determine the rate tolerance, the binder-free CNP electrode was cycled at various current densities ranging from 50 mA g^{-1} to 1 A g^{-1} (**Figure 5.4d**). With the increase in the current density, a specific discharge capacity of 764, 689, 610, 506, 448 and 394 mA h g^{-1} was obtained at 50, 100, 200, 400, 800 and 1000 mA g^{-1} respectively (**Figure S5.2**). When the current rate was restored to 50 mA g^{-1}, the specific capacity of the CNP anode was 751 mA h g^{-1}, indicating the tolerance of the battery towards high current rates.

Figure 5.4e shows the Nyquist plots of the CNP electrode before and after cycling. A depressed semicircle spiked at the lower frequency region can be seen. The impedance spectra were

modelled using an equivalent circuit presented in the inset of **Figure 5.4e**. The resistance due to the contact between particles and the electrolyte is represented by R_{EL}, C_{LC} is the capacitance associated with an electrical double layer and R_{LC} is the charge transfer resistance. A parallel combination of capacitance and resistance, C_{SEI} and R_{SEI} respectively, is associated with the SEI formation [20]. A constant phase element (Q_i) in parallel with resistance (R_i) is also present, indicating ion-diffusion into the CNPs. The charge-transfer resistance increased to 83 Ω from 81 Ω after the initial cycle.

To understand the contribution of the electrode setup towards capacity, pristine nickel foam was tested against lithium, which delivered a specific capacity of meagre 0.6 mA h g^{-1}. As the capacity offered by the pristine nickel is negligible (**Figure S5.3**), the superior electrochemical performance of the as-prepared CNP anodes is attributed to the unique self-assembly of CNP and the binder-free electrode architecture. The porosity of Ni-foam and spacing between the neighbouring CNPs allow easy diffusion of electrolytes into the interior of the electrode. This unique setup might help in overcoming the pulverization and exfoliation of CNPs deposited onto the current collector [23]. Also, good electronic contact between the CNPs and Ni-foam enables an easy flow of electrons. Furthermore, the absence of insulating polymeric binder could facilitate better lithium-flux, with enhanced electron kinetics and conducting pathways throughout the electrode [6]. For comparison, the cycling performance of the traditional electrode of CNP mixed with a polymeric binder (polyvinylidene fluoride) and conducting additive was investigated. Surprisingly, the performance of the CNP anode with binder displayed a low specific capacity of ~ 232 mA h g^{-1} at 1 Ag^{-1} (**Figure S5.4**) when tested against lithium, unlike the one without binder.

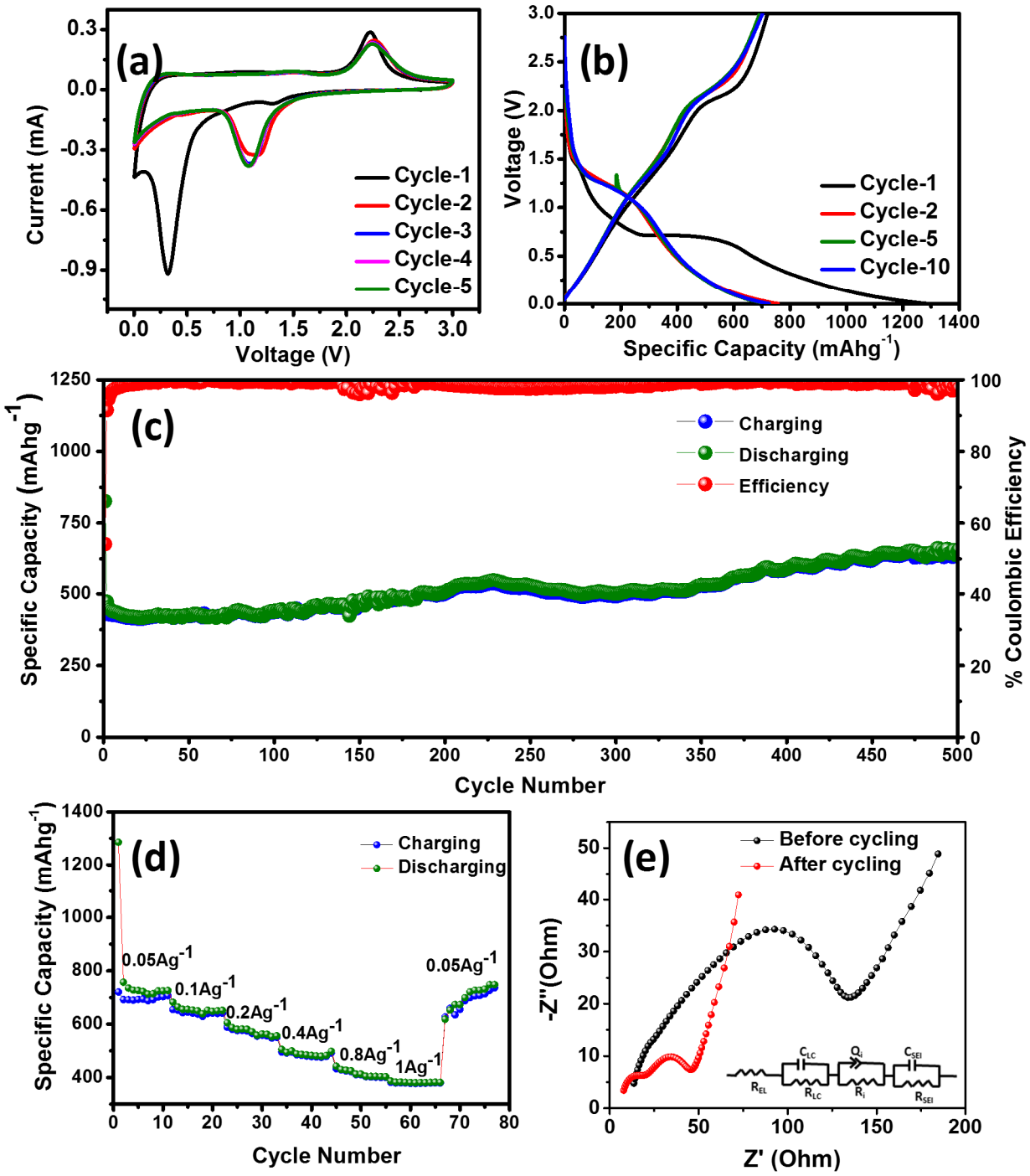

Figure 5.4 (a) Cyclic voltammogram, (b) galvanostatic charge-discharge (50 mA g^{-1} current density) curve, (c) cycling stability (current density = 1 A g^{-1}), (d) rate capability and (e) electrochemical impedance spectroscopy before and after cycling at open circuit potential of CNP *vs.* Li/Li^+.

To investigate ion storage mechanism in the electrode material, *ex-situ* TEM and *ex-situ* XPS techniques were used to characterise charged and discharged electrode samples, and the results

are shown in **Figures 5.5a and b** (TEM images) and **Figure 5.5c (**XPS spectra). The TEM images after discharging and recharging show no obvious changes in *d*-spacing, indicating the absence of intercalation into the graphitic domains. The Li 1s XPS spectra of samples discharged at 0.8 V and 0.005 V showed a gradual shift in binding energy towards metallic lithium, indicating a void-filling mechanism in the lower voltage domain (near to 0V) [24]. Further, *ex-situ* XRD studies (**Figure 5.5d**) of electrodes were carried out at different charged and discharged state which showed a completely amorphous profile (between 2θ of 0º and 40º), without any distinct peak for that of carbon. The absence of peaks belonging to a crystallite phase is an indication amorphous product formation along with a chemically stable SEI [25]. The other crystalline peaks in the *ex-situ* XRD correspond to that of the Ni-metal template (JCPDS 65-2865) [26]. In all, the lithium-ion storage in the present electrode involves adsorption of lithium-ions at defect sites, edges, and the surface of nanographitic domains along with nanovoids filling. Also, the enhanced performance could be attributed to the easy transport of electrolyte and lithium-ion throughout the electrode (**Figure 5.5e**). It was observed that the CNP-binder free anode performance is comparable or even better than those reported in the literature [7, 8, 27-31].

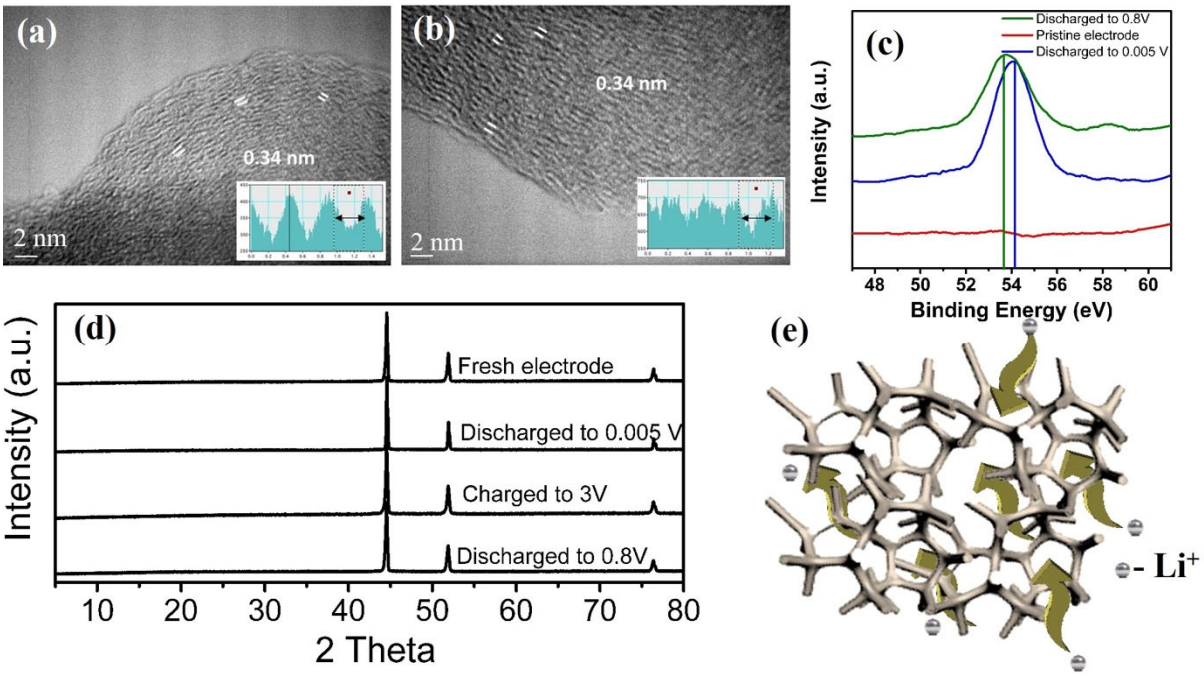

Figure 5.5 *Ex-situ* TEM images of (a) discharged and (b) recharged electrode; *ex-situ* (c) XPS and (d) *ex-situ* XRD of the binder-free CNP electrodes at different charged and discharged states. (e) Schematic of lithium-ion transport across the electrode.

The feasibility of the binder-free electrode in sodium-ion batteries was also tested. **Figure 5.6a** shows the CV curves of CNP *vs.* Na/Na^+ measured in the voltage domain 0.005 to 3 V at a sweep rate of 0.2 mV s^{-1}. Two reduction peaks at 0.005 V and 0.8 V were observed in the first cathodic process indicating the decomposition of electrolytes and the formation of the SEI layer [17]. The shape of CV is nearly rectangular, suggesting capacitive storage behaviour for the as-prepared 3D binder-free CNP anode in NIBs [32]. The sodium-ion interaction with the CNPs is an amalgamation of physical interactions, interactions with functional groups and other redox-reactions [17]. After the initial cycle, the CV almost overlapped on each-other which indicates reversible sodium insertion and extraction. **Figure 5.6b** shows the galvanostatic charge-discharge curves of CNP measured at a current density of 50 mA g^{-1}, in the voltage domain of 0.005 to 3.0 V. A second cycle discharge capacity of 241 mA h g^{-1} was observed. Similar to that observed for LIBs, the formation of SEI on the surface of anode lead to a loss in the capacity during the initial cycle. The low coulombic efficiency is typically observed in carbon materials due to the formation of SEI and irreversible sodium-ion interaction at vacancies or defects in the CNPs [33]. Even though a low initial coulombic efficiency of ~20% was observed, it stabilizes to near 97 % in the later cycles. This could be correlated with the CV curves, which overlapped on one-another upon prolonged cycling. The battery cycled at 50 mA g^{-1} (**Figure 5.6c**) showed a stable cycling performance and the stability was maintained even when the battery was cycled at 1 Ag^{-1} over 400 cycles with a near 100% coulombic efficiency (**Figure S5.5**). The rate performance of the anode was evaluated with current densities ranging from 50 mA g^{-1} to 1 A g^{-1}. With the increase in the current density, a specific discharge capacity of 118, 92, 76, 64 and 54 mA h g^{-1} at a current density of 100, 200, 400, 800 and 1000 mAg^{-1} respectively were obtained (**Figure 5.6d, Figure S5.6**). When compared with lignin-based electrospun carbon nanofibers [34], reduced graphene oxide (free-standing paper electrode) [35], leaf-derived porous carbon [9] and porous carbon nanofibers [36], the CNPs reported in the present work show superior performance with a specific capacity of 241 at 50 mA g^{-1} in the second cycle and a stable cycling performance.

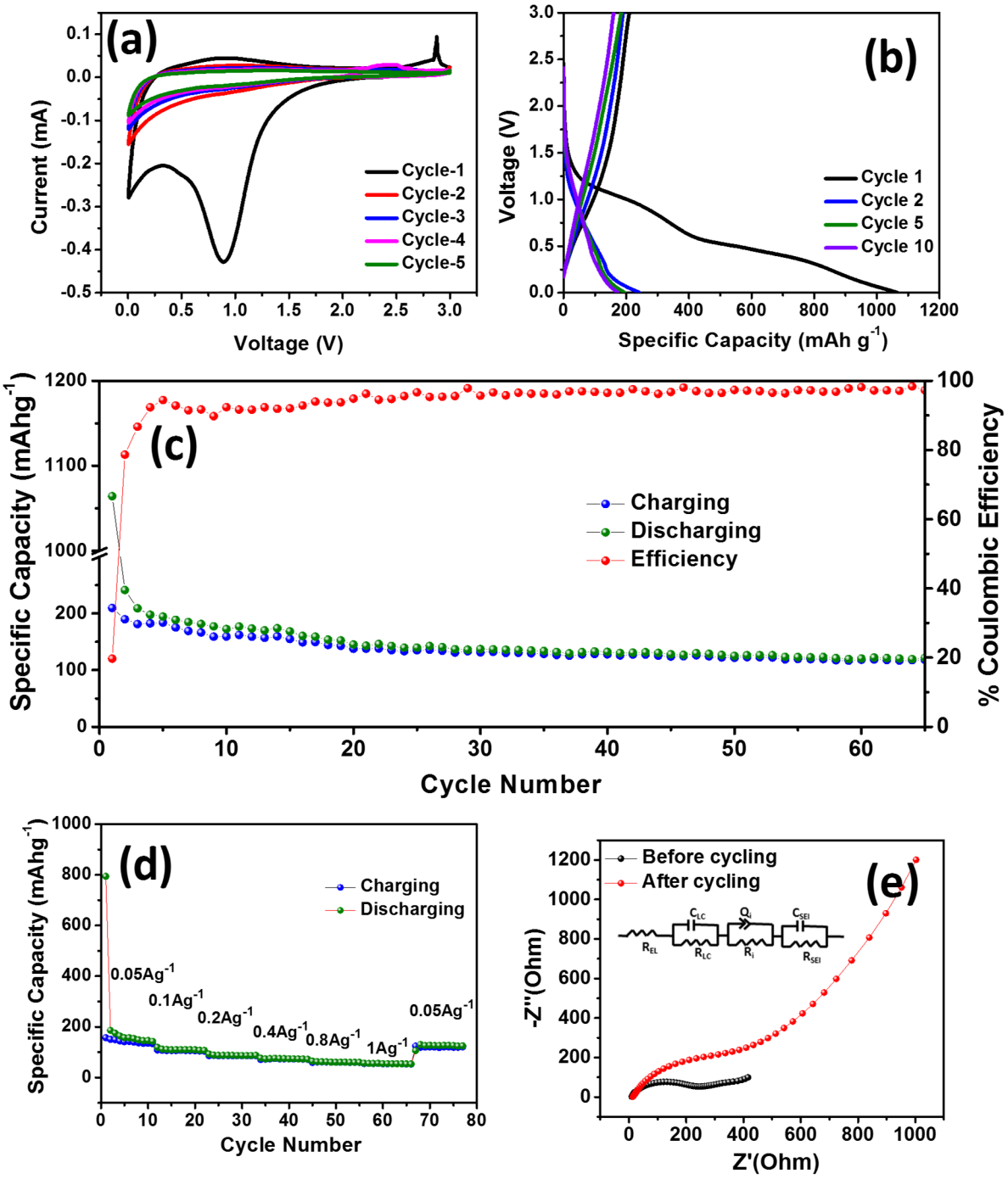

Figure 5.6 Electrochemical performance of binder-free CNP anodes tested against sodium: (a) cyclic voltammogram, (b) galvanostatic charge-discharge curves, (c) cycling stability and (d) rate performance. (e) EIS before and after cycling at open circuit potential for electrodes tested against sodium.

The Nyquist plot for the CNP anode exhibited a semicircle spiked at the lower frequency region (**Figure 5.6e**). From the semicircle, the charge-transfer resistance of the anodes before and after SEI formation can be obtained. The equivalent circuit is placed in the inset of the EIS spectra.

The impedance spectra during the formation of SEI was taken before cycling on a newly assembled battery. After performing CV (5 cycles) test on the battery, the EIS measurements were undertaken. The charge-transfer resistance (R_{LC}) is increased to 3595 ohms from 68.8 ohms after the formation of SEI.

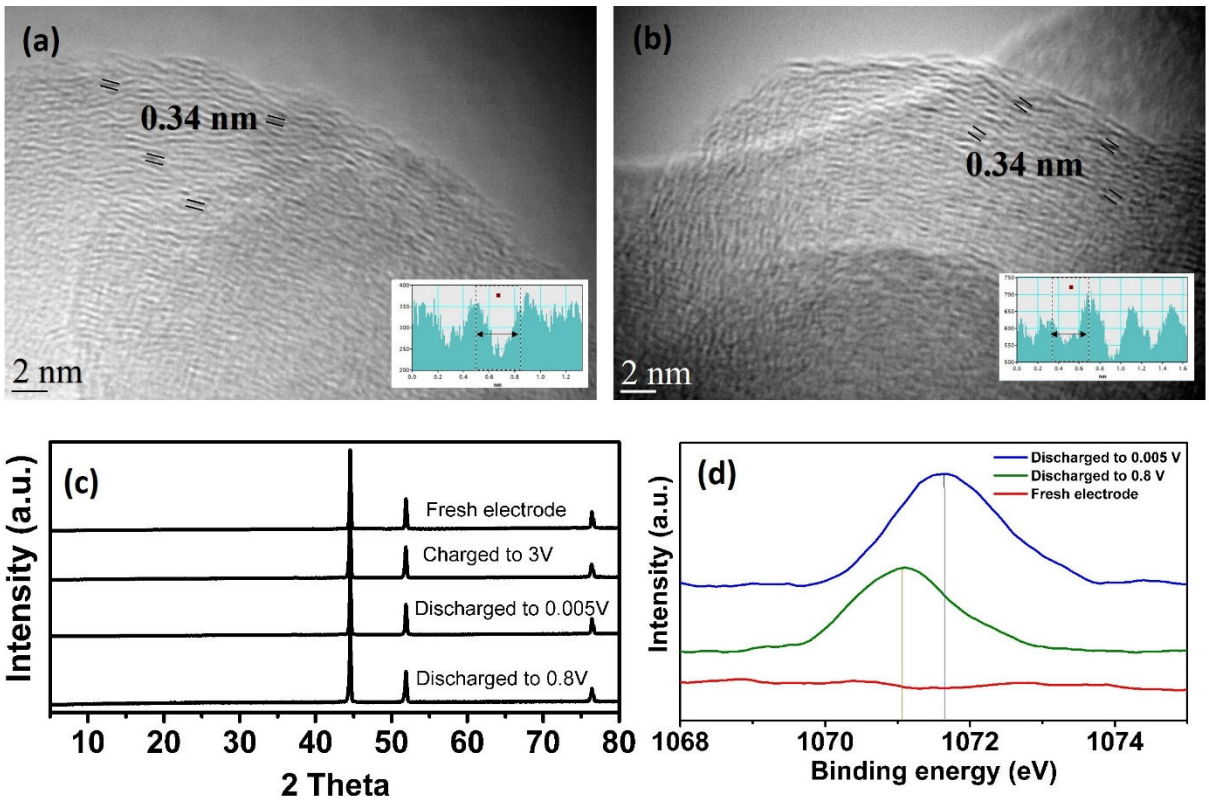

Figure 5.7 *Ex-situ* TEM images of (a) discharged and (b) recharged electrode; (c) *ex-situ* XRD and (d) *ex-situ* XPS of the electrodes at charged and discharged states.

Given the interlayer *d*-spacing, the intercalation of sodium-ion in the as-prepared carbon material might not be prominent. Therefore, the sodium-ion storage predominantly evolves from adsorption at defect sites and vacancies, alongside filling nanovoids. *Ex-situ* TEM (**Figure 5.7a and 5.7b**) confirmed the adsorption mechanism, where no changes in the *d*-spacing after discharging and charging was observed. Similar to that witnessed for LIB, the *ex-situ* XRD for CNP electrode in NIB (**Figure 5.7c**) also showed no crystalline profile for carbon, indicating the formation of amorphous product alongside the formation of SEI. In addition, the *ex-situ* XPS (**Figure 5.7d**) depicted a shift in the value of the binding energy for the Na 1s spectra approaching the metallic Na upon discharging from 0.8 to 0.005 V. Overall, the as-prepared binder-free CNP anode against lithium and sodium, showed a good electrochemical performance. The morphology of carbon nanoparticle and the electrode architecture play an

important role in the effective operation of the battery. The outstanding properties make the present electrodes as a promising choice for alkali-ion batteries.

5.4 Conclusion

In summary, we have developed a facile and scalable method for realizing a binder-free flexible three-dimensional carbon electrode formed on a nickel-foam. The free-standing carbon nanoparticles self-assembled onto the nickel-foam *via* a flame deposition process without a binder or carbon black, thus simplifying electrode fabrication process and lowering the electrode cost. In addition, this new electrode design facilitates electrolyte transport, thus delivering good performance in both lithium and sodium-ion batteries as an anode. Good cycling stability and rate performance were also observed. Given the electrochemical performance, the present electrode is believed to be a promising candidate for high-performance alkali-ion batteries.

5.5 References

[1] B. Jache, P. Adelhelm, Angew. Chem. Int. Ed., 53 (2014) 10169-10173.

[2] J. Ding, H. Wang, Z. Li, A. Kohandehghan, K. Cui, Z. Xu, B. Zahiri, X. Tan, E.M. Lotfabad, B.C. Olsen, D. Mitlin, ACS Nano, 7 (2013) 11004-11015.

[3] M.D. Slater, D. Kim, E. Lee, C.S. Johnson, Adv. Funct. Mater., 23 (2013) 947-958.

[4] J. Górka, C. Vix-Guterl, C. Matei Ghimbeu, C, 2 (2016) 24.

[5] B. Koo, H. Kim, Y. Cho, K.T. Lee, N.-S. Choi, J. Cho, Angew. Chem. Int. Ed., 51 (2012) 8762-8767.

[6] S. Yuan, X.L. Huang, D. L. Ma, H.G. Wang, F.Z. Meng, X.B. Zhang, Adv. Mater., 26 (2014) 2273-2279.

[7] M. Kakunuri, C.S. Sharma, Electrochim. Acta, 180 (2015) 353-359.

[8] B. Campbell, R. Ionescu, Z. Favors, C.S. Ozkan, M. Ozkan, Sci. Rep., 5 (2015) 14575.

[9] H. Li, F. Shen, W. Luo, J. Dai, X. Han, Y. Chen, Y. Yao, H. Zhu, K. Fu, E. Hitz, L. Hu, ACS Appl. Mater. Inter., 8 (2016) 2204-2210.

[10] G. Oza, M. Ravichandran, V.I. Merupo, S. Shinde, A. Mewada, J.T. Ramirez, S. Velumani, M. Sharon, M. Sharon, Sci. Rep., 6 (2016) 21286.

[11] M. Sharon, K. Mukhopadhyay, K. Yase, S. Iijima, Y. Ando, X. Zhao, Carbon, 36 (1998) 507-511.

[12] R.R. Gaddam, D. Vasudevan, R. Narayan, K.V.S.N. Raju, RSC Adv., 4 (2014) 57137-57143.

[13] I. Elizabeth, B.P. Singh, S. Trikha, S. Gopukumar, J. Power Sources, 329 (2016) 412-421.

[14] D.S. Knight, W.B. White, J. Mater. Res., 4 (1989) 385-393.

[15] N.A. Kumar, H.-J. Choi, Y.R. Shin, D.W. Chang, L. Dai, J.-B. Baek, ACS Nano, 6 (2012) 1715-1723.

[16] C.J. Liang, J.D. Liao, A.J. Li, C. Chen, H.Y. Lin, X.J. Wang, Y.-H. Xu, Fuel, 128 (2014) 422-427.

[17] N.A. Kumar, R.R. Gaddam, S.R. Varanasi, D.F. Yang, S.K. Bhatia, X.S. Zhao, Electrochim. Acta, 214 (2016) 319-325.

[18] D. Stevens, J. Dahn, J. Electrochem. Soc., 148 (2001) A803-A811.

[19] Y. Cao, L. Xiao, X. Ai, H. Yang, Electrochem. solid-state lett., 6 (2003) A30-A33.

[20] E.M. Lotfabad, J. Ding, K. Cui, A. Kohandehghan, W.P. Kalisvaart, M. Hazelton, D. Mitlin, ACS Nano, 8 (2014) 7115-7129.

[21] K. Tang, R.J. White, X. Mu, M.M. Titirici, P.A. van Aken, J. Maier, ChemSusChem, 5 (2012) 400-403.

[22] N.A. Kaskhedikar, J. Maier, Adv. Mater., 21 (2009) 2664-2680.

[23] J. Jiang, Y. Li, J. Liu, X. Huang, C. Yuan, X.W. Lou, Adv. Mater., 24 (2012) 5166-5180.

[24] Y. Li, Y.-S. Hu, M.-M. Titirici, L. Chen, X. Huang, Adv. Energy Mater., 6 (2016) 1600659.

[25] J. Xu, I.-Y. Jeon, J. Ma, Y. Dou, S.-J. Kim, J.M. Seo, H. Liu, S. Dou, J.-B. Baek, L. Dai, Nano Res., (2017) 1-14.

[26] C. Xu, Y. Liu, Q. Hao, H. Duan, J. Mater. Chem. A, 1 (2013) 13542-13548.

[27] A. Abouimrane, O.C. Compton, K. Amine, S.T. Nguyen, J. Phys. Chem. C, 114 (2010) 12800-12804.

[28] Y. Hu, X. Li, J. Wang, R. Li, X. Sun, J. Power Sources, 237 (2013) 41-46.

[29] H. Sun, A.E. Del Rio Castillo, S. Monaco, A. Capasso, A. Ansaldo, M. Prato, D.A. Dinh, V. Pellegrini, B. Scrosati, L. Manna, F. Bonaccorso, J. Mater. Chem. A, 4 (2016) 6886-6895.

[30] K. Chiwon, C. Eunho, B. Rangasamy, C. Wonbong, Nanotechnology, 27 (2016) 105402.

[31] Z. Zhou, H. Zhang, Y. Zhou, H. Qiao, A. Gurung, R. Naderi, H. Elbohy, A.L. Smirnova, H. Lu, S. Chen, Q. Qiao, Sci. Rep., 7 (2017) 1440.

[32] H.L. Wang, W.H. Yu, J. Shi, N. Mao, S.G. Chen, W. Liu, Electrochim. Acta, 188 (2016) 103-110.

[33] S. Wenzel, T. Hara, J. Janek, P. Adelhelm, Energy Environ. Sci., 4 (2011) 3342.

[34] J. Jin, S.J. Yu, Z.Q. Shi, C.Y. Wang, C.B. Chong, J. Power Sources, 272 (2014) 800-807.

[35] L. David, G. Singh, J. Phys. Chem. C, 118 (2014) 28401-28408.

[36] W. Li, L. Zeng, Z. Yang, L. Gu, J. Wang, X. Liu, J. Cheng, Y. Yu, Nanoscale, 6 (2014) 693-698.

5.6 Supplementary Information

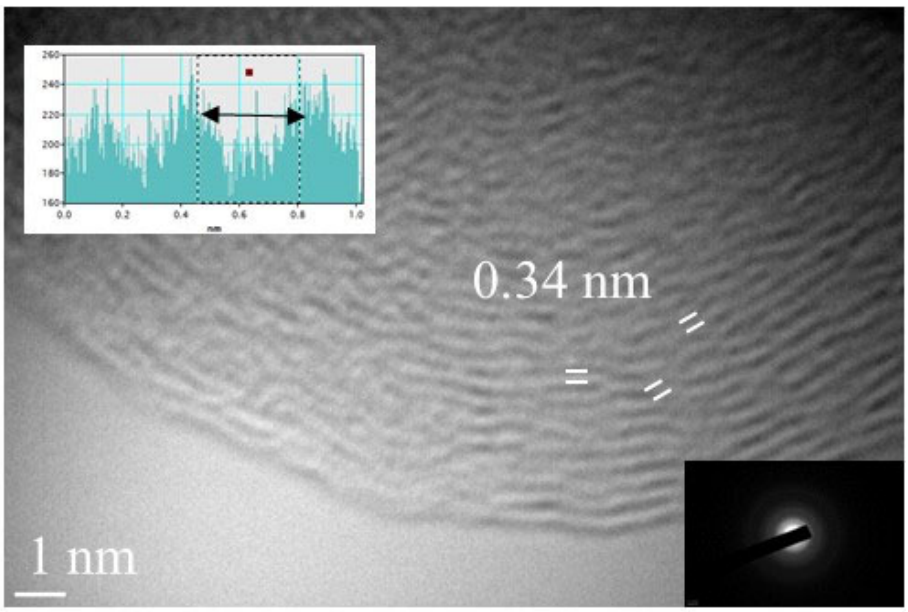

Figure S5.1 High resolution TEM image of carbon nanoparticle (Diffraction pattern shown in the inset).

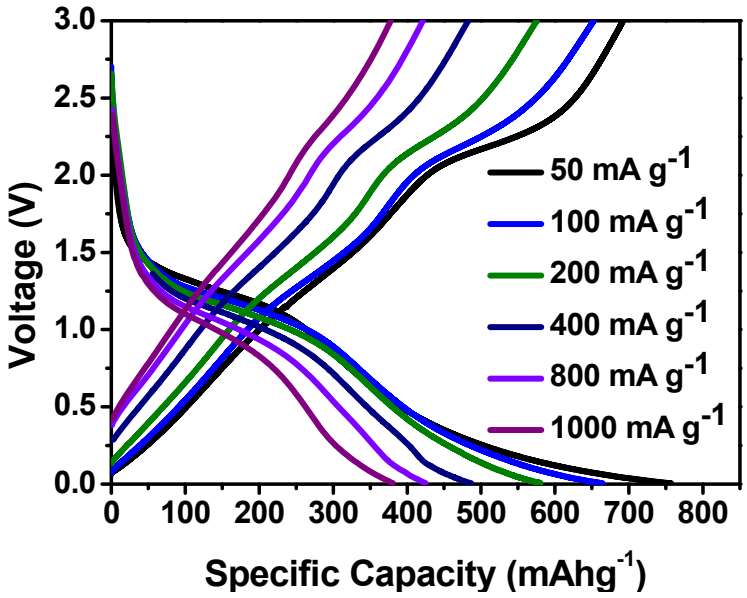

Figure S5.2 Charge-discharge curves of CNP vs. Li/Li^+ at different current densities

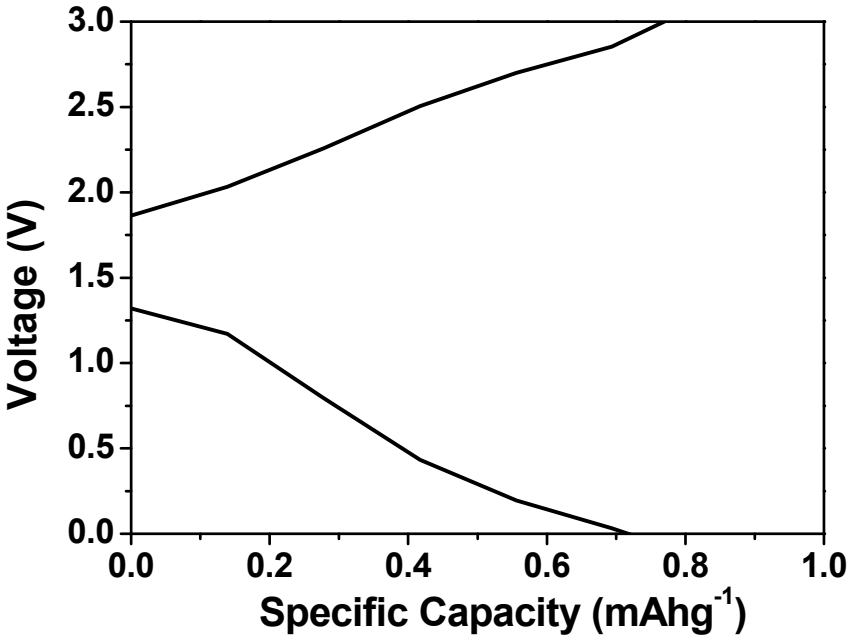

Figure S5.3 Charge-discharge curves (current density = 100 mAg^{-1}) of pristine nickel electrode tested against lithium.

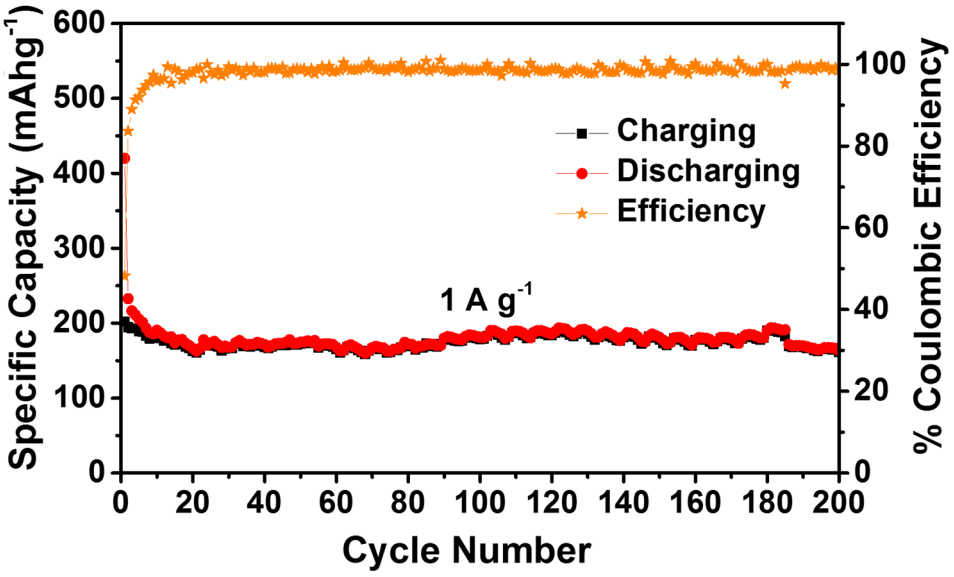

Figure S5.4 Cycling stability of CNP mixed with binder and conducting additive tested against lithium.

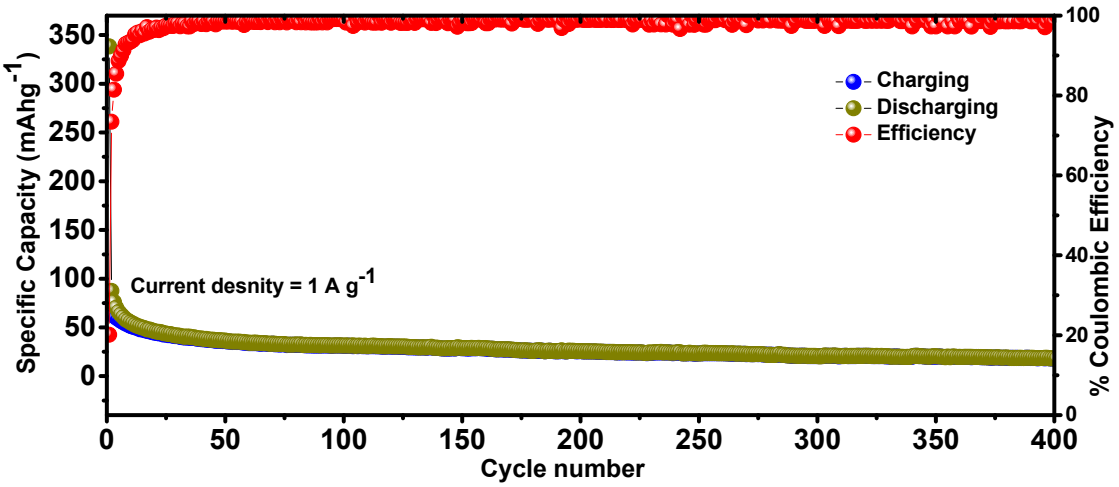

Figure S5.5 Cycling performance of the as-prepared binder-free CNP electrode tested against sodium at a current density of 1 Ag^{-1}.

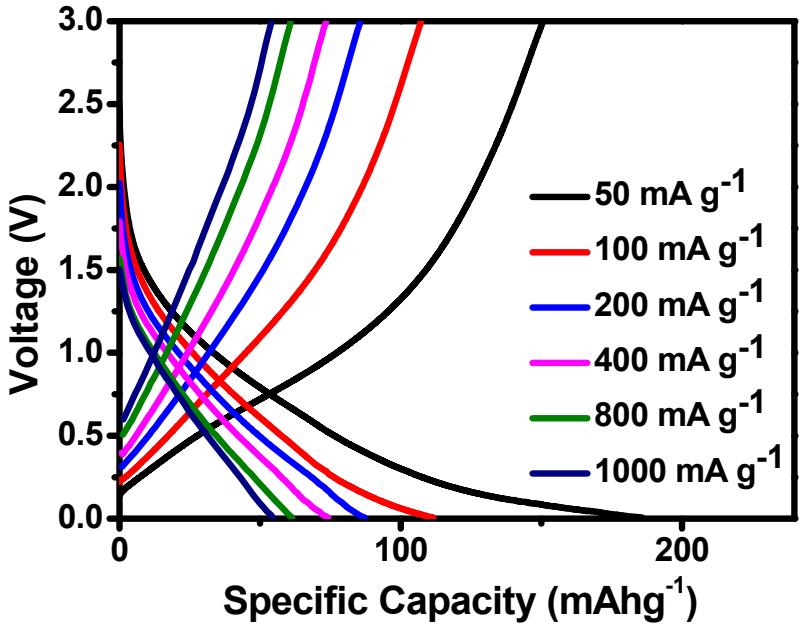

Figure S5.6 Charge-discharge curves of binder-free CNP *vs.* Na/Na^+ at different current densities.

Chapter 6. Spinifex grass derived carbons for sodium-ion batteries

-Published as *R. R. Gaddam et al.* Spinifex nanocellulose derived hard carbon as anodes for high-performance sodium-ion batteries, *Sustainable Energy and Fuels*, 2017,1, 1090-1097 (Listed as 2017 Sustainable Energy and Fuels HOT Article)

6.1 Introduction

In order to establish a decarbonized global economy, efficient and affordable energy storage technologies are of paramount importance. Especially, rechargeable batteries based electrochemical energy storage systems are promising owing to their efficiency and cycle life. Up to day, lithium-ion batteries (LIBs) have been the primary power source for most of the portable electronic devices [1]. Though the energy and power-density of LIBs are attractive, large-scale implementation of LIBs can lead to a significant upsurge in price, due to the uneven geographical distribution of lithium precursors [2]. Hence, a great deal of attention is being paid towards sodium-ion batteries (NIBs) as a potential technology for large-scale stationary energy storage, as sodium resources are practically unlimited [3]. Adopting this technology can significantly reduce the cost of the NIBs in comparison with that of LIB systems [4]. In spite of this, NIB technology is still its infancy, and its widespread adoption is highly dependent on the design of low-cost, high-performance electrode materials both cathode and anode. Several cathode materials with superior performance have already been reported [5]. Also, research on sodium-ion intercalation compound based cathodes are not new and have been previously studied alongside those for LIBs [6]. Compared with that of cathodes, the discovery of a suitable anode material for NIBs still remains a challenge [7]. This is because graphite, the most widely-used anode in LIBs, is unsuitable for sodium-ion storage in traditional electrolytes owing to thermodynamic instabilities [8]. Anode materials like metal-alloys [9, 10], oxides [11], nitrides [12], and carbonaceous materials [7] have been investigated for NIBs. While alloy materials pose concerns related to significant volume expansion during cycling leading to capacity fading and loss of electrical contact, metal oxides, on the other hand, have low sodium-storage capabilities. These drawbacks effectively limit the large-scale commercialization of such anodes. Therefore, carbonaceous materials appear to be the most promising anode material for the NIB system owing to their reversible capacity and low sodium-storage voltage [13, 14]. Emerging materials used for NIBs include few layer graphene [6, 15], carbon nanowires [16], carbon nanoparticles [17] and hard carbons derived from various precursors [18]. Although often touted as a promising anode, hard carbons still suffer from the poor overall performance. Therefore, developing hard carbon materials with high-performance is desirable. From the standpoint of sustainability, biomass-derived hard carbons are an attractive anode material for sodium-ion storage [19]. Their renewability, natural abundance and simple synthesis strategies have garnered interest in many research fields. In this work, a filament-like nanocellulose or cellulose nanofibers (CNF) derived from an extremophilic ‘spinifex’ grass (*Triodia pungens*) (**Figure S6.1**), is used as a sustainable precursor material for hard carbon

production. Spinifex is a highly abundant tussock grass endemic to the Australian continent, and has evolved over 15 million years under extreme desert conditions and presently covers one-third of the landmass [20]. Recently, we have demonstrated that very high aspect ratio (>500) cellulose nanofibers can be extracted from this grass with a very mild chemical treatment and low-energy mechanical process [21]. Compared to nanocellulose produced from other sources, the special attributes of the spinifex nanocellulose offer competitive advantages, such as, ultra-high aspect-ratio, incomparable flexibility and toughness, as well as uniquely high hemicellulose content (about 42 wt. %), which facilitate low energy and low cost processing. This contrasts the production of carbons from cellulose nanocrystals produced by a typical sulfuric acid hydrolysis (40-70%)[22], which upon the scale-up of process, will significantly increase costs, safety risks, and environmental impact.

The high-energy requirements in the production of carbon materials *via* carbonization, is another area worth considering in terms of sustainability. Attempts to reduce energy consumption typically involve reducing the maximum carbonization temperature by 'low temperature' carbonization of precursors around 1000°C [22, 23], However, the stabilization step is often considered the most energy consuming step, rather than carbonization [24, 25]. Authors which have previously carbonized cellulose nanofibers or cellulose nanocrystals for carbon anodes in NIBs, followed a similar protocol by stabilizing the nanocellulose in air for 8 hours, heating at an extremely slow rate of 1°C/min, followed by carbonization for 2 hours in argon (total heating time approximately 15 hours) [22, 25]. In this work, the unique low-cost, green-processed and high aspect ratio spinifex CNF was carbonized at 1000°C (in 4 hours) to yield a nanocellulose derived carbon (NDC) which was used as an anode material for NIBs. A specific discharge capacity of 386 mA h g^{-1} was obtained in the second cycle at a current density of 20 mA g^{-1}, and ~300 mA h g^{-1} a current density of 100 mA g^{-1} which is comparable or even higher than the values reported previously for carbonaceous anodes for NIBs [17, 26-32].

6.2 Materials and methods

6.2.1 Materials

Triodia pungens grass was collected near Camooweal, northwest Queensland, Australia. The chemicals used in this study included sodium hydroxide, glacial acetic acid (Ajax Finechem, Thermo Fischer Pty Ltd, Scoresby, Australia) and sodium chlorite technical grade, 80% (Sigma-Aldrich, Castle Hill, Australia), were used as-received.

6.2.2 Preperation of nanocellulose

Cellulose nanofibrils (CNF) from *Triodia pungens* (also known as Australian spinifex grass) was produced based on the method described in our previous work [21, 33, 34]. Briefly, after being harvested and washed, *T. pungens* was cut to the length of about 7 mm. Then the chopped grass was delignified at 80 °C for two hours using a 2 % (w/v) sodium hydroxide solution with a 10:1 solvent to grass ratio, followed by twice bleaching with an acidic solution of 1 % (w/v) sodium chlorite at 70 °C for one hour with a 30:1 solvent to grass ratio (pH=4, the pH was decreased with glacial acetic acid). Finally, a 0.3 wt% dispersion of bleached fibers was passed through a high-pressure homogenizer (Panda 2K NS1001L, GEA Niro Soavi S.p.A, Italy) for two passes at 700 bar pressure. The resulting nanocellulose dispersions were then stirred overnight and freeze-dried.

Based on the TAPPI standard analytical analysis (TAPPI, Acid-insoluble lignin in wood and pulp, modified method based on Test Method T-222 om-88, 1988; TAPPI, Acid-soluble lignin in wood and pulp, Useful Method UM-250, 1991) [35], the *T. pungens* raw grass sample was found to be comprised of 29 % (w/w) cellulose, 38.5 % (w/w) hemicellulose, and 20 % (w/w) lignin, and the treated bleached nanofiber used for carbonization consisted of 48 %, 37 %, and 2.5 % (w/w) of cellulose, hemicellulose, and lignin respectively.

6.2.3 Carbonization of spinifex nanocellulose

The carbonization of freeze-dried spinifex nanocellulose was carried out at 1000°C in a single zone tube furnace (CTF wire wound, 1300°C, Carbolite Gero) equipped with an aluminum oxide tube. The cellulose fibers were stabilized by heating to 240 °C at 5 °C min^{-1} under a constant flow of nitrogen and was held at this temperature for 2 hours. The samples were then heated under nitrogen to 1000°C for carbonization at a rate of 5°C min^{-1} and held at this temperature for another 2 hours, before being allowed to cool down.

6.2.4 Material characterization

X-ray diffraction (XRD) was carried out on a Bruker D8 Advance X-ray diffractometer with Ni-filtered Cu Kα radiation (λ = 1.54056 Å; 40 kV, 30 mA). The morphology of the prepared samples was examined by using a field emission scanning electron microscope (FESEM, JEOL 7001) and transmission electron microscope (TEM, JEOL 2100) at an acceleration voltage of 200 kV. X-ray photoelectron spectroscopy (XPS) spectra were acquired on a Kratos Axis ULTRA X-ray photoelectron spectrometer. Raman spectra were collected using a Renishaw Raman Spectrometer fitted with a 514 nm laser.

6.2.5 Electrochemical testing

The working electrode was fabricated by mixing the active material, carbon black and polyvinyldine fluoride (PVdF) in a mass ratio of 7:2:1 and homogenizing them in N-methyl pyrrolidine (NMP). The slurry was coated onto a Cu foil current collector, followed by drying under vacuum at 60°C overnight. 2032-type coin cells were assembled in an argon-filled glovebox at <0.1 ppm of water and oxygen content. For NIBs, glass fibre was used as the separator, sodium foil as the counter electrode, 1 M NaClO4 in a 1:1 (v/v) mixture of ethylene carbonate (EC) and propylene carbonate (PC) mixed with 0.3 wt% of fluoroethylene carbonate (FEC) additive as the electrolyte. Cyclic voltammetric (CV) measurements were carried out on a CHI-600D electrochemical workstation using cutoff voltages between 0.005 and 3V versus Na/Na^+ at a scan rate of 0.2 mV s^{-1}. Electrochemical impedance spectroscopy measurement was conducted in the frequency range of 100 kHz to 10 mHz. Galvanostatic charge/discharge measurements were performed on a NEWARE BTS-CT3008 system at various current densities.

6.3 Results and discussion

Figure 6.1a and 6.1b show the TEM images of spinifex NDCs. The formation of sheet-like structure post-pyrolysis of nanocellulose may be due to the longitudinal self-assembly of the long and thin cellulose nanofibers into a film-like structure during freeze-drying. During the freezing process, cellulose nanofibers (**Figure S6.2**) are trapped between the ice crystals and squeezed into the space between the crystals, which resulted in increasing the concentration of nanofiber in growing lamellar ice templates. When the ice molecules slowly sublimated, the concentrated cellulose nanofibers rearranged and self-assembled along the longitudinal direction *via* hydrogen bonds and van der Waals forces to form a lamellar structure (**Figure S6.3**) [36, 37]. This phenomenon has been found to be concentration dependent, where the formation of sheets is favoured by high concentration dispersions (> 0.1 wt%), while the formation of fibres on freeze-drying happens at low concentrations (< 0.1 wt%) [38].

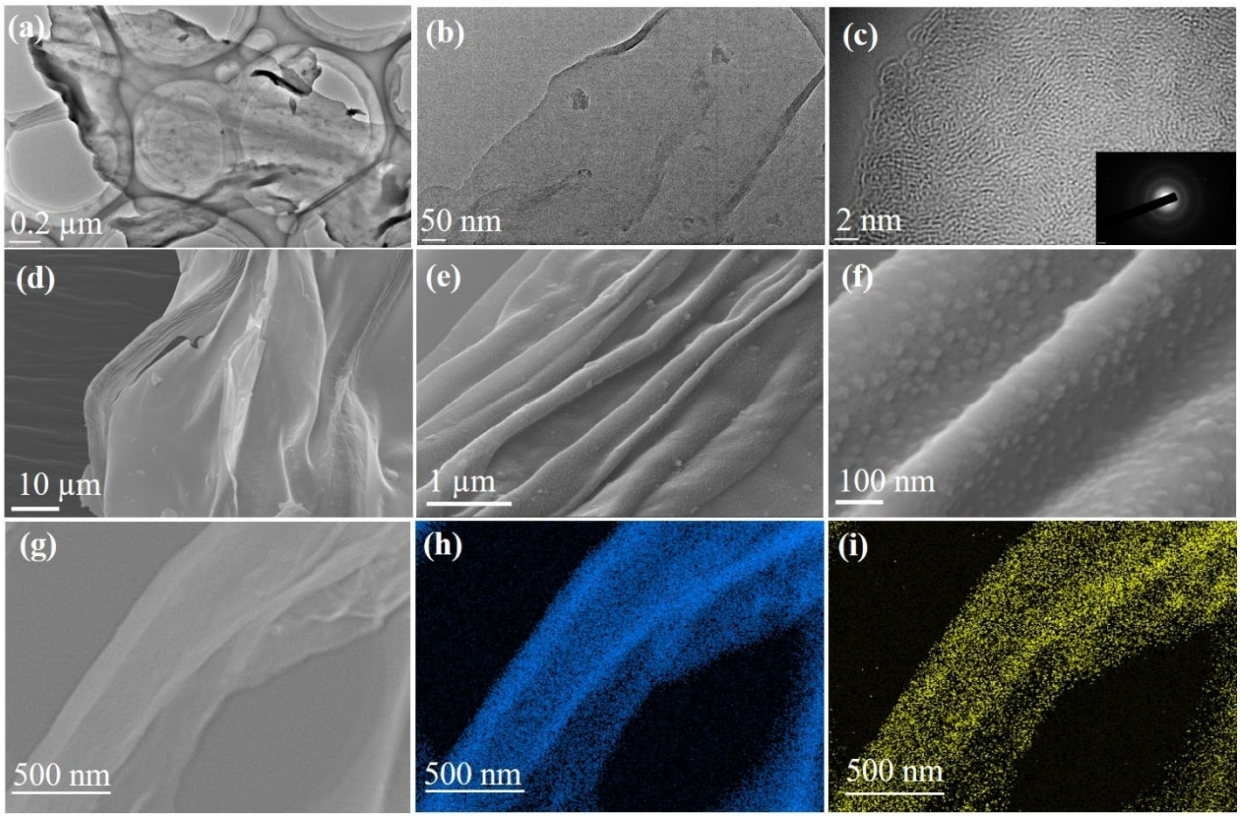

Figure 6.1 The structure and morphology of the NDC shown from TEM images (a, b, c), FESEM images (d, e, f), scanning transmission electron microscopy (STEM) (g), and energy dispersive X-ray mapping of carbon (h) and oxygen (i).

The dispersions of nanocellulose in the present work were > 0.1 wt%, which led to the increase in hydrogen bonding between fibrils, resulting in the formation of sheets. Subsequently, the CNFs were carbonized at 1000 °C to form sheet-like NDC. This temperature is optimum for the formation of the crystalline hard carbon material as indicated previously from theoretical and experimental studies [22]. The high-resolution TEM images (**Figure 6.1c**) indicate the presence of graphitic microcrystallites with an interlayer spacing of ~0.39 nm (**Figure S6.4**). The selected area diffraction pattern presented in the inset of **Figure 6.1c** reveals the presence of small crystalline domains interspersed in the amorphous matrix, which reconfirms the high-resolution TEM image. The presence of turbostratic graphitic domains can provide sufficient electrons for redox reactions enabling better rate performance [39]. The FESEM (**Figure 6.1d to 6.1f**) images of NDCs indicate the lamellar architecture and crumpled graphite sheet-like morphology [40]. Additionally, the elemental mapping images of NDCs display the uniform distribution of carbon and oxygen throughout the material (**Figure 6.1g to 6.1i**).

Figure 6.2a shows the X-ray diffraction profiles of NDCs. As can be seen, the characteristic (002) and (100) peaks corresponding to graphitic carbons were observed at 23º and 45º respectively [8]. The interlayer *d*-spacing was found to be approximately 0.39 nm as calculated from XRD, which is similar to that calculated from HRTEM. Compared to a *d*-spacing of 0.34 nm in the case of natural graphite, an increased layer-to-layer spacing in NDCs could enable the large sodium-ions to easily insert and exert [40]. The Raman spectra of NDCs displayed prominent D and G band at ~1358 cm^{-1} and ~1598 cm^{-1} respectively (**Figure 6.2b**). The G band is a result of in-plane bond-stretching motions of sp^2 bonded carbon atoms whereas the D band is due to out of plane vibrations attributed to the presence of disordered sp^3 carbon atoms. The I_D/I_G ratio of NDC is 1.05 indicating the disordered nature of the carbon sheets and the associated unrepaired edge defects [41]. The intensity of G-band is slightly higher than that of D-band suggesting higher in-plane bond-stretching of sp^2 carbon atoms [39]. To gain an understanding of the electrochemical performance of as prepared carbons, N_2 adsorption-desorption studies were carried out in the relative pressure range of 0 to 1 (**Figure 6.2c**). The inset shows the pore size distribution calculated from the corresponding N_2 adsorption-desorption isotherm using the Barrett–Joyner–Halenda (BJH) method. These distributions indicate the presence of both micropores and mesopores. The BET surface area of NDC was found to be around 154 $m^2\ g^{-1}$.

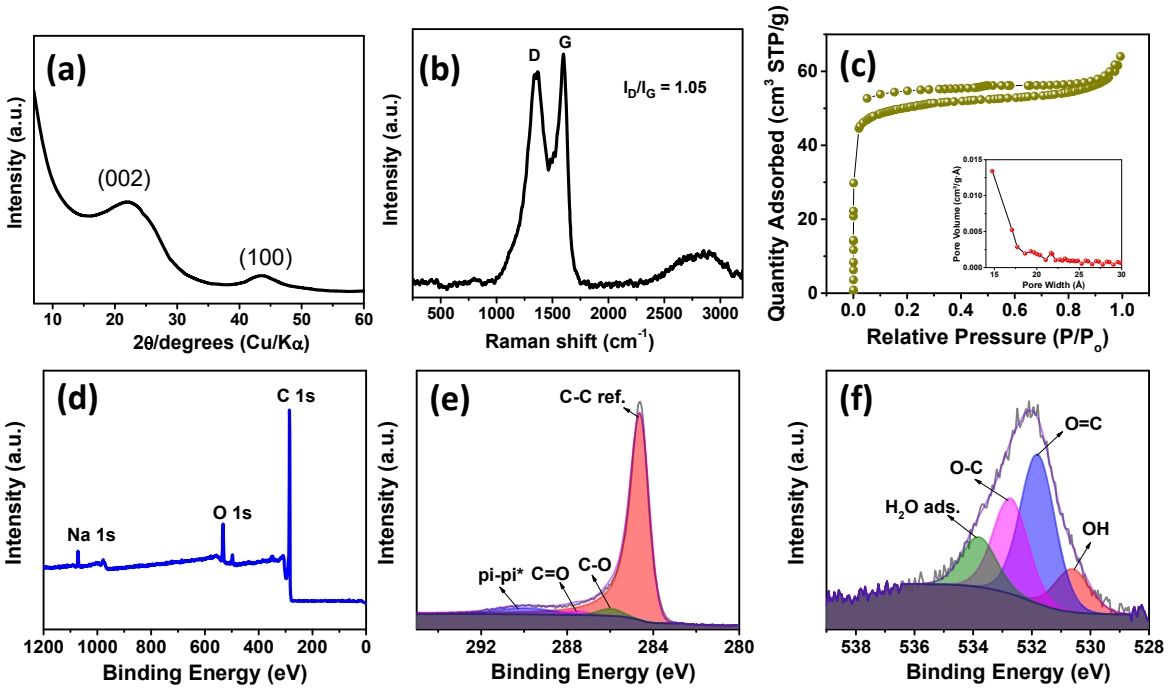

Figure 6.2 (a) X-ray diffraction pattern, (b) Raman spectrum, (c) N_2 adsorption-desorption isotherms (inset: BJH pore-size distribution of spinifex NDC), (d) XPS survey scan and high resolution C 1s (e) and O 1s (f) spectra of the NDC.

The X-ray photoelectron spectroscopic (XPS) survey showed a pronounced C1s peak (90.96 at%) at about 285 eV along with a weaker O1s peak (7.54 at%) at 534 eV (**Figure 6.2d**). The C1s spectrum (**Figure 6.2e**) is deconvoluted into a dominant component of C-C sp^2, C=O and C–O at 284.6, 285.9 and 285.6 eV respectively. Also, a long π-π* peak with a broadening on the high energy side, indicating the presence of conductive graphitic carbons, could be observed at ~290.05 eV [42]. Similarly, the O1s spectrum (**Figure 6.2f**) can be deconvoluted to OH, O=C, O-C and adsorbed H_2O at 530.6, 531.8, 532.7 and 533.8 eV respectively. In addition, a small Na 1s peak (1.51 at%) at 1071 eV is present. Though the influence of sodium is not investigated in the present work, we believe that this sodium impurity would not contribute significantly to the performance of the battery owing to the low surface area of the as-prepared NDCs [17, 41].

The electrochemical performance of NDC was evaluated in a coin-type half-cell with sodium-foil as the counter electrode. The cyclic voltammetry (CV) studies were carried out between 0.005 to 3 V at a scan rate of 0.2 mV s^{-1}. Three reduction peaks at 0.02, 0.5 and 1.0 V were observed during the initial cycle (**Figure 6.3a**). The peak at 0.5 and 1V correspond to the formation of solid electrolyte interphase (SEI) on the surface of NDC, which disappeared in the following cycles [43]. Owing to the low surface area of NDC, these peaks can be attributed to the sodium insertion into the bulk. After the initial cycle, no significant changes in the cathodic and anodic peaks were observed indicating the stable electrochemical interaction of NDC with sodium-ions. The cathodic peak near 0 V can be due to sodium-ion insertion or micro plating of sodium into the micropores of NDC [44]. A pair of highly reversible cathodic and anodic peaks at 0.4-0.01 V, similar to that of lithium insertion into graphite, could be observed in the later cycles [45]. The charge-storage behaviour of NDCs can be credited to chemical adsorption on heteroatom (oxygen) surface, nano-plating, intercalation between layers of graphite, and/or adsorption at defect sites [13]. In order to further investigate the intercalation of sodium-ions, logarithmic plots of scan rate *vs*. peak current were used to obtain slope *b* (**Figure S6.5**). The capacitive contribution was determined according to the equation $i=av^b$ [46]. The *b*-value for the anodic peaks were found to be around 0.34 indicating the presence of sodium-insertion into the NDCs.

The stable cycling performance delivered by the NDC was further investigated using electrochemical impedance spectroscopy (**Figure 6.3b**). The Nyquist plot was taken at different sodiation and desodiation cycles in order to probe the electrochemical performance. A depressed semicircle with a large diameter in the high-frequency region followed by a spike

at the low-frequency region was observed [39]. The semicircle corresponds to the sodium-ions passing through the passivating SEI layer and the charge transfer resistance between the electrolyte and the active layer. The sodium-ion diffusion into and out of the NDCs is represented by the spiked region. The impedance spectra were modelled using an equivalent circuit represented in **Figure S6.6**. Here, R_{el} represents the electrolyte resistance, C_{ct} signifies the double layer capacitance, R_{ct} is the charge transfer resistance, Z_w is the Warburg element associated with ion diffusion in carbon electrode. The SEI formation at the electrode surface results in a resistance and a capacitance named as C_{SEI} and R_{SEI}, respectively. The kinetic parameters were obtained by modeling the impedance using the equivalent circuit. The value of R_{ct} for the fresh cell is 27.2 **Ω**. After 5 cycles R_{ct} is around 30 **Ω** which further increased to 186 **Ω** in the 50^{th} cycle. The electrode-electrolyte activation in the initial cycle stabilises the system and provides steady cycling performance in the later cycles.

Representative galvanostatic charge-discharge curves at a current density of 20 mA g^{-1} and voltage between 0.005 to 3 V are shown in **Figure 6.3c**. A specific discharge and charge capacity of 722 and 366 mA h g^{-1} with a columbic efficiency of ~50% were obtained in the initial cycle. This loss in the initial capacity is mainly due to the decomposition of electrolyte that led to the formation of a passivating solid electrolyte interphase on the surface of NDC.[40] During the initial cycling, due to the insertion of sodium-ions, the graphitic microstructure may begin to exfoliate exposing fresh surfaces, which could potentially result in limited local pulverization of the electrode. In this case, the fresh surfaces may cause the formation of new SEI and subsequent loss in coulombic efficiency during the initial cycle [47]. After the initial cycle the coulombic efficiency stabilized to near 100% in the 10^{th} cycle, indicating the system's stability. A superior discharge capacity of 386 mA h g^{-1} obtained in the second cycle is higher than the values reported previously for carbonaceous anodes in NIBs. The charge-discharge curve shows three different potential regions (i) a plateau from 0 to 0.25 V corresponding to intercalation of sodium-ions into NDC electrode (ii) a slope-plateau from 1.2 to 0.25 V related to trapping at dangling hydrogen terminals followed by (iii) a monotonous slope above 1.2 V.[45] This behavior is well correlated with that observed in the CV curves. The presence of multiple defect sites and vacancies increases the reversible capacity of the as prepared carbons in NIBs.[15] Furthermore, the performance of the NDC against sodium was evaluated by continuously varying the current densities (**Figure S6.7**). From **Figure 6.3d,** it can be observed that the discharge capacities of 386, 326, 301, 274, 228, 195 and 157 mA h g^{-1} were obtained at 20, 50, 100, 200, 400, 800 and 1000 mA g^{-1} current density respectively. The capacity can be largely restored for repeated cycles after continuous cycling at different current rates (20-

1000 mA g^{-1}), and abruptly switching to 20 mA g^{-1} after deep cycling at 1 A g^{-1}. These results suggest the fast and efficient transport kinetics of sodium-ions, superior stability and rate capability, which can be attributed to the specific characteristics of NDC.

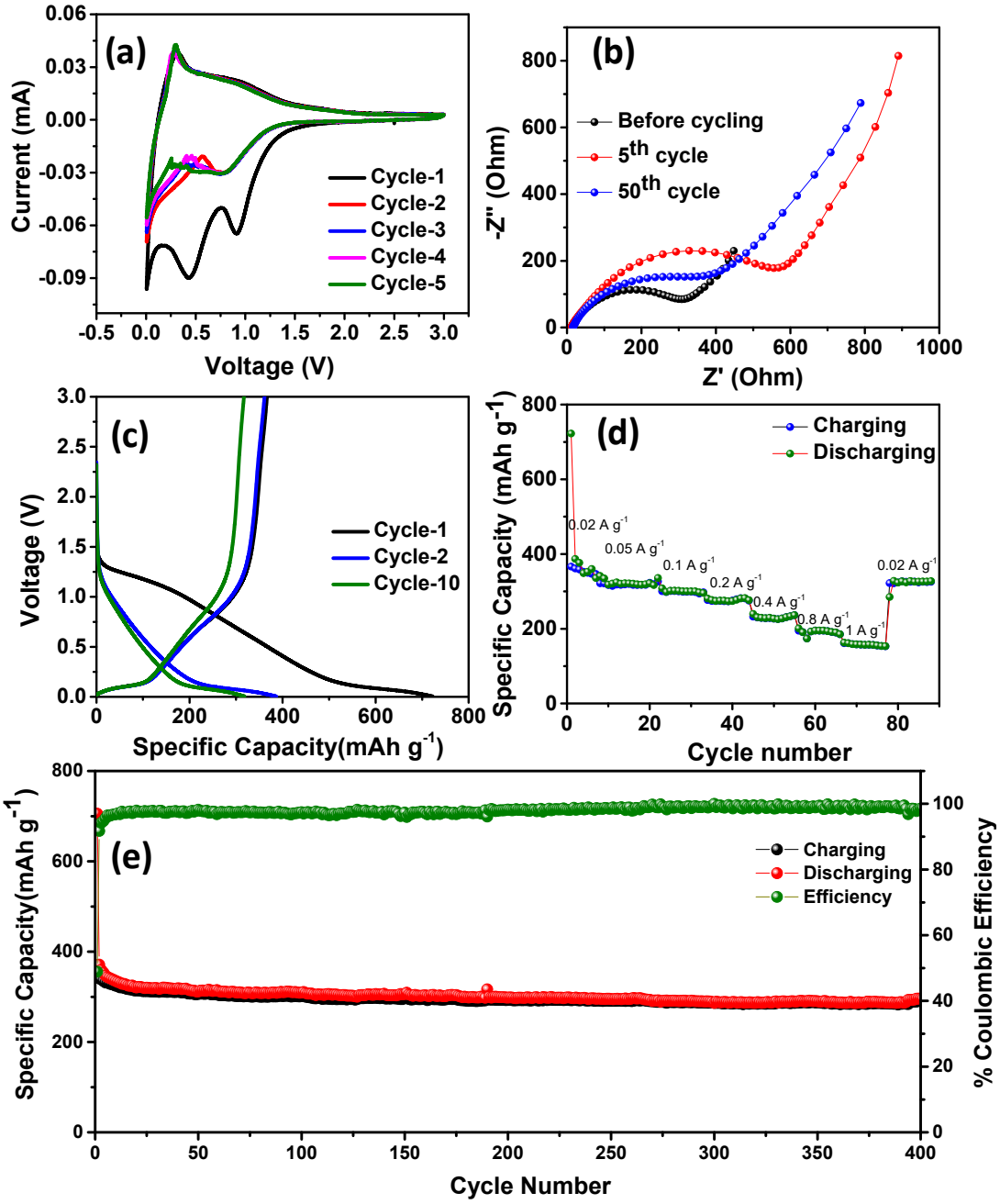

Figure 6.3 (a) CV curves, (b) Nyquist plots, (c) galvanostatic charge-discharge curves at a current density of 20 mA g^{-1}, (d) rate performance and (e) cycling stability of spinifex NDC tested against sodium at a current density of 100 mA g^{-1}.

Table 6.1 Comparison of carbon-based anodes reported in the literature for NIBs

Material	Precursor	Initial CE	Discharge capacity (mA h g^{-1})	Rate capability	Reference
Sprinifex Hard Carbon	Nanocellulose	50%	386 at 20 mA g^{-1}	326 mA h g^{-1} at 50 mA g^{-1} 300 mA h g^{-1} at 100 mA g^{-1}	This work
Hard carbon	Apple waste	61 %	230 at 20 mA g^{-1}	112 mA h g^{-1} at 1 A g^{-1} 86 mA h g^{-1} at 2 A g^{-1}	[26]
Porous carbons	Peanut skin	34 %	266 at 30 mA g^{-1}	154 mA h g^{-1} at 1 A g^{-1} 47 mA h g^{-1} at 10 A g^{-1}	[27]
Hard-carbon	Cellulose	NA	255 at 40 mA g^{-}	176 mA h g^{-1} at 200 mA g^{-1} 85 mA h g^{-1} at 2 A g^{-1}	[25]
Carbon nanosheet	Peat moss	57.5%	255 at 50 mA g^{-1}	203 mA h g^{-1} at 0.5 A g^{-1} 150 mA h g^{-1} at 1 A g^{-1}	[47]
Carbon nanoparticles	Coconut oil	49%	278 at 0.1 A g^{-1}	135 mA h g^{-1} at 0.2 A g^{-1} 107 mA h g^{-1} at 0.4 A g^{-1}	[17]
Carbon sheet	Wheat straw	50.53%	293 at 50 mA g^{-1}	255 mA h g^{-1} at 0.1 A g^{-1} 220 mA h g^{-1} at 0.2 A g^{-1}	[48]
N-doped carbon sheets	Okra	NA	315.2 at 0.1 C	302.1 mA h g^{-1} at 0.1 C 32.3 mA h g^{-1} at 30 C	[39]
Lamellar carbon	Maize	NA	267 at 50 mA g^{-1}	222.3 mA h g^{-1} at 0.1 A g^{-1} 144.5 mA h g^{-1} at 0.3 A g^{-1}	[49]
Carbon microtubes	Renewable cotton	83 %	300 at 30 mA g^{-1}	275 mA h g^{-1} at 0.15 A g^{-1} 180 mA h g^{-1} at 0.3 A g^{-1}	[50]
Mesoporous carbon	Honey	43.7 %	394 at 0.1 A g^{-1}	281 mA h g^{-1} at 0.5 A g^{-1} 217 mA h g^{-1} at 1 A g^{-1}	[51]
Carbon sheets	Corn stalks	52.6 %	260 at 0.1 A g^{-1}	216 mA h g^{-1} at 0.5 A g^{-1} 136 mA h g^{-1} at 1 A g^{-1}	[32]
Hard carbon	Leaf membrane	74.8 %	360 at 10 mA g^{-1}	320 mA h g^{-1} at 0.02 A g^{-1} 270 mA h g^{-1} at 0.04 A g^{-1}	[52]

Figure 6.3e shows the long-term cycling performance of the NDC electrode tested at a current density of 100 mA g^{-1}. Even under prolonged cycling, a specific discharge capacity of 305 mA h g^{-1} was retained at the 150th cycle. This stable specific discharge capacity is one of the highest among the biomass-derived carbon anodes for NIBs. This superior performance can be attributed to defects and increased interlayer spacing than that of conventional graphite. In view of the above results, the electrochemical sodium storage performance of these NDCs is far superior to carbonaceous materials previously reported in the literature [11, 22, 26, 50, 53-57]. A comparison of the performance of the NDC with the state-of-art carbons is given in **Table 6.1**.

6.4 Conclusions

A simple preparation method for producing low-cost, sustainable hard carbon with a sheet-like morphology from an abundant biomass source as anode materials for rechargeable NIBs is demonstrated. The carbon was produced from the greenly processed, high hemicellulosic spinifex CNF by fast stabilization at 240°C, and low-temperature carbonization at 1000°C. The NDC as an anode delivered superior performance with excellent specific capacity, rate capability and cycling stability for sodium-ion batteries. An increased layer-to-layer spacing than that of conventional graphite in the as-prepared carbon (~0.39 nm) enabled the large sodium-ions to easily intercalate. A specific capacity of 386 mA h g^{-1} and 300 mA h g^{-1} at current densities of 20 and 100 mA g^{-1} respectively was obtained. These values are on par with that of graphite in lithium-ion batteries and one of the highest capacity carbon anodes for NIBs. The good performance of the carbons in sodium-ion batteries highlights the use of sustainable resources for clean energy storage.

6.5 References

[1] T. Reddy, D. Linden, Linden's Handbook of Batteries (4th Edition), McGraw-Hill Professional Publishing, New York, NY, USA, 2010.

[2] S. Engelke, Storage4.EU, 1 (2013) 1-7.

[3] M.D. Slater, D. Kim, E. Lee, C.S. Johnson, Adv. Funct. Mater., 23 (2013) 947-958.

[4] Y. Wang, R. Chen, T. Chen, H. Lv, G. Zhu, L. Ma, C. Wang, Z. Jin, J. Liu, Energy Storage Mater., 4 (2016) 103-129.

[5] C. Fang, Y.H. Huang, W.X. Zhang, J.T. Han, Z. Deng, Y.L. Cao, H.X. Yang, Adv. Energy Mater., 6 (2016) 1501727.

[6] L.L. Peng, Y. Zhu, D.H. Chen, R.S. Ruoff, G.H. Yu, Adv. Energy Mater., 6 (2016) 1600025.

[7] M.S. Balogun, Y. Luo, W.T. Qiu, P. Liu, Y.X. Tong, Carbon, 98 (2016) 162-178.

[8] Y.X. Wang, S.L. Chou, H.K. Liu, S.X. Dou, Carbon, 57 (2013) 202-208.

[9] Y. Kim, Y. Park, A. Choi, N.S. Choi, J. Kim, J. Lee, J.H. Ryu, S.M. Oh, K.T. Lee, Adv. Mater., 25 (2013) 3045-3049.

[10] L. Wu, X.H. Hu, J.F. Qian, F. Pei, F.Y. Wu, R.J. Mao, X.P. Ai, H.X. Yang, Y.L. Cao, Energy Environ. Sci., 7 (2014) 323-328.

[11] H. Su, S. Jaffer, H. Yu, Energy Storage Mater., 5 (2016) 116-131.

[12] X.J. Li, M.M. Hasan, A.L. Hector, J.R. Owen, J. Mater. Chem. A, 1 (2013) 6441-6445.

[13] D.A. Stevens, J.R. Dahn, J. Electrochem. Soc., 147 (2000) 1271-1273.

[14] D.A. Stevens, J.R. Dahn, J. Electrochem. Soc., 148 (2001) A803-A811.

[15] N.A. Kumar, R.R. Gaddam, S.R. Varanasi, D.F. Yang, S.K. Bhatia, X.S. Zhao, Electrochim. Acta, 214 (2016) 319-325.

[16] Y. Cao, L. Xiao, M.L. Sushko, W. Wang, B. Schwenzer, J. Xiao, Z. Nie, L.V. Saraf, Z. Yang, J. Liu, Nano Lett., 12 (2012) 3783-3787.

[17] R.R. Gaddam, D.F. Yang, R. Narayan, K.V.S.N. Raju, N.A. Kumar, X.S. Zhao, Nano Energy, 26 (2016) 346-352.

[18] E. Irisarri, A. Ponrouch, M.R. Palacin, J. Electrochem. Soc., 162 (2015) A2476-A2482.

[19] J. Wang, P. Nie, B. Ding, S. Dong, X. Hao, H. Dou, X. Zhang, J. Mater. Chem. A, 5 (2017) 2411-2428.

[20] A. Toon, M. Crisp, H. Gamage, J. Mant, D. Morris, S. Schmidt, L.G. Cook, Sci. rep., 5 (2015).

[21] N. Amiralian, P.K. Annamalai, P. Memmott, E. Taran, S. Schmidt, D.J. Martin, RSC Adv., 5 (2015) 32124-32132.

[22] H. Zhu, F. Shen, W. Luo, S. Zhu, M. Zhao, B. Natarajan, J. Dai, L. Zhou, X. Ji, R.S. Yassar, T. Li, L. Hu, Nano Energy, 33 (2017) 37-44.

[23] E. Jiang, N. Amiralian, M. Maghe, B. Laycock, E. McFarland, B. Fox, D.J. Martin, P.K. Annamalai, ACS Sus. Chem. Eng., (2017).

[24] M. Maghe, C. Creighton, L.C. Henderson, M.G. Huson, S. Nunna, S. Atkiss, N. Byrne, B.L. Fox, J. Mater. Chem. A, 4 (2016) 16619-16626.

[25] W. Luo, J. Schardt, C. Bommier, B. Wang, J. Razink, J. Simonsen, X.L. Ji, J. Mater. Chem. A, 1 (2013) 10662-10666.

[26] L.M. Wu, D. Buchholz, C. Vaalma, G.A. Giffin, S. Passerini, Chemelectrochem, 3 (2016) 292-298.

[27] H.L. Wang, W.H. Yu, J. Shi, N. Mao, S.G. Chen, W. Liu, Electrochim. Acta, 188 (2016) 103-110.

[28] D. Yan, C.Y. Yu, X.J. Zhang, W. Qin, T. Lu, B.W. Hu, H.L. Li, L.K. Pan, Electrochim. Acta, 191 (2016) 385-391.

[29] G.Y. Xu, J.P. Han, B. Ding, P. Nie, J. Pan, H. Dou, H.S. Li, X.G. Zhang, Green Chem., 17 (2015) 1668-1674.

[30] K.L. Hong, L. Qie, R. Zeng, Z.Q. Yi, W. Zhang, D. Wang, W. Yin, C. Wu, Q.J. Fan, W.X. Zhang, Y.H. Huang, J. Mater. Chem. A, 2 (2014) 12733-12738.

[31] J. Jin, S.J. Yu, Z.Q. Shi, C.Y. Wang, C.B. Chong, J. Power Sources, 272 (2014) 800-807.

[32] D.C. Qin, F. Zhang, S.Y. Dong, Y.Z. Zhao, G.Y. Xu, X.G. Zhang, RSC Adv., 6 (2016) 106218-106224.

[33] N. Amiralian, P.K. Annamalai, P. Memmott, D.J. Martin, Cellulose, 22 (2015) 2483-2498.

[34] K. Markstedt, A. Mantas, I. Tournier, H. Martínez Ávila, D. Hägg, P. Gatenholm, Biomacromolecules, (2015) 150325142328001.

[35] R.C. Pettersen, V.H. Schwandt, J. wood chem. tech., 11 (1991) 495-501.

[36] J. Han, C. Zhou, Y. Wu, F. Liu, Q. Wu, Biomacromolecules, 14 (2013) 1529-1540.

[37] R. Dash, Y. Li, A.J. Ragauskas, Carbohydrate Polymers, 88 (2012) 789-792.

[38] S.Y. Cho, Y.S. Yun, H.-J. Jin, Macromol. Res., 22 (2014) 753-756.

[39] T. Yang, T. Qian, M. Wang, X. Shen, N. Xu, Z. Sun, C. Yan, Adv. Mater., 28 (2016) 539-545.

[40] J. Xu, M. Wang, N.P. Wickramaratne, M. Jaroniec, S. Dou, L. Dai, Adv. Mater., 27 (2015) 2042-2048.

[41] E.M. Lotfabad, J. Ding, K. Cui, A. Kohandehghan, W.P. Kalisvaart, M. Hazelton, D. Mitlin, ACS Nano, 8 (2014) 7115-7129.

[42] H. Estrade-Szwarckopf, Carbon, 42 (2004) 1713-1721.

[43] E. Lim, C. Jo, M.S. Kim, M.H. Kim, J. Chun, H. Kim, J. Park, K.C. Roh, K. Kang, S. Yoon, J. Lee, Adv. Funct. Mater., 26 (2016) 3711-3719.

[44] C.M. Wu, P.I. Pan, Y.W. Cheng, C.P. Liu, C.C. Chang, M. Avdeev, S.K. Lin, J. Power Sources, 340 (2017) 14-21.

[45] K. Tang, R.J. White, X. Mu, M.M. Titirici, P.A. van Aken, J. Maier, ChemSusChem, 5 (2012) 400-403.

[46] H. Lindström, S. Södergren, A. Solbrand, H. Rensmo, J. Hjelm, A. Hagfeldt, S.-E. Lindquist, J. Phys. Chem. B, 101 (1997) 7717-7722.

[47] J. Ding, H. Wang, Z. Li, A. Kohandehghan, K. Cui, Z. Xu, B. Zahiri, X. Tan, E.M. Lotfabad, B.C. Olsen, D. Mitlin, ACS Nano, 7 (2013) 11004-11015.

[48] D. Qin, S. Chen, J. Solid State Electrochem., (2016) 1-8.

[49] T. Yang, X. Niu, T. Qian, X. Shen, J. Zhou, N. Xu, C. Yan, Nanoscale, 8 (2016) 15497-15504.

[50] Y. Li, Y.-S. Hu, M.-M. Titirici, L. Chen, X. Huang, Adv. Energy Mater., (2016) 1600659.

[51] Y.Z. Zhang, L. Chen, Y. Meng, J. Xie, Y. Guo, D. Xiao, J. Power Sources, 335 (2016) 20-30.

[52] H. Li, F. Shen, W. Luo, J. Dai, X. Han, Y. Chen, Y. Yao, H. Zhu, K. Fu, E. Hitz, L. Hu, ACS Appl. Mater. Inter., 8 (2016) 2204-2210.

[53] N. Sun, H. Liu, B. Xu, J. Mater. Chem. A, 3 (2015) 20560-20566.

[54] Z.Q. Yuan, L.L. Si, X.B. Zhu, J. Mater. Chem. A, 3 (2015) 23403-23411.

[55] L.F. Xiao, Y.L. Cao, W.A. Henderson, M.L. Sushko, Y.Y. Shao, J. Xiao, W. Wang, M.H. Engelhard, Z.M. Nie, J. Liu, Nano Energy, 19 (2016) 279-288.

[56] L.H. Yin, Y.X. Wang, C.C. Han, Y.M. Kang, X. Ma, H. Xie, M.B. Wu, J. Power Sources, 305 (2016) 156-160.

[57] X.M. Zhu, Q. Li, S. Qiu, X.L. Liu, L.F. Xiao, X.P. Ai, H.X. Yang, Y.L. Cao, JOM, 68 (2016) 2579-2584.

6.6 Supplementary information

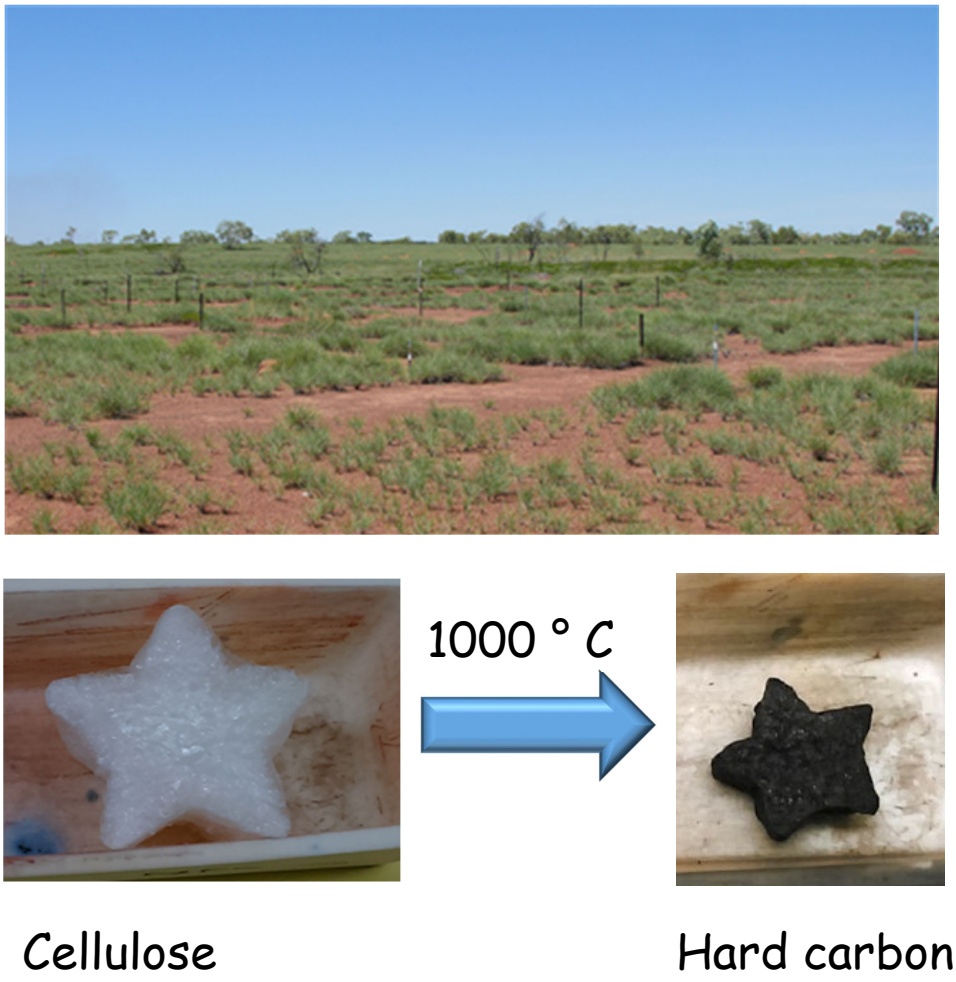

Figure S6.1 Picture of spinifex grass (top) hummocks growing in the grassland in Camooweal, Queensland, Australia (19.9° S, 138.1° E). Cellulose and hard carbon structures obtained after processing (below).

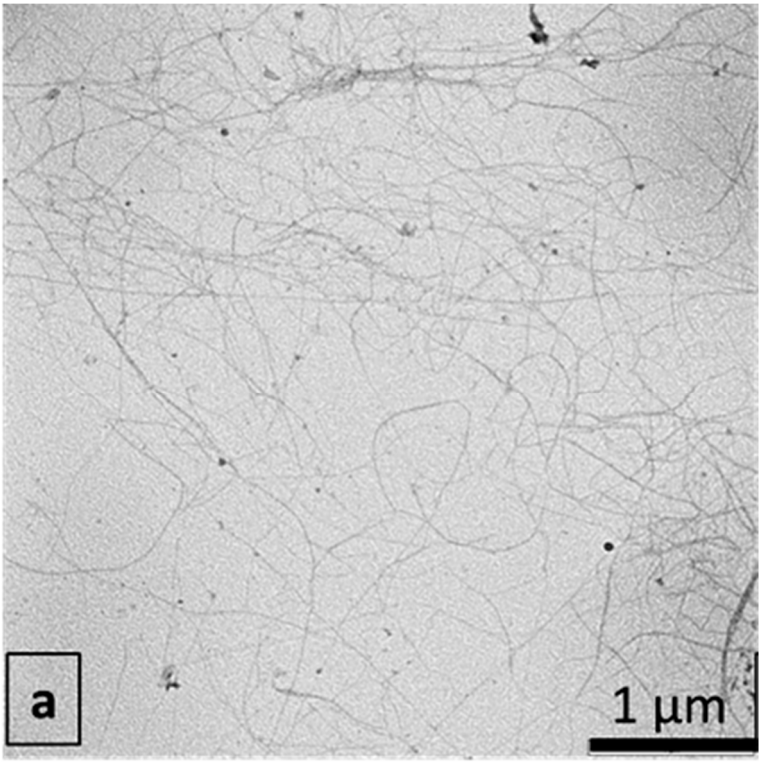

Figure S6.2 TEM images of suspension of bleached spinifex grass derived cellulose nanofibers.

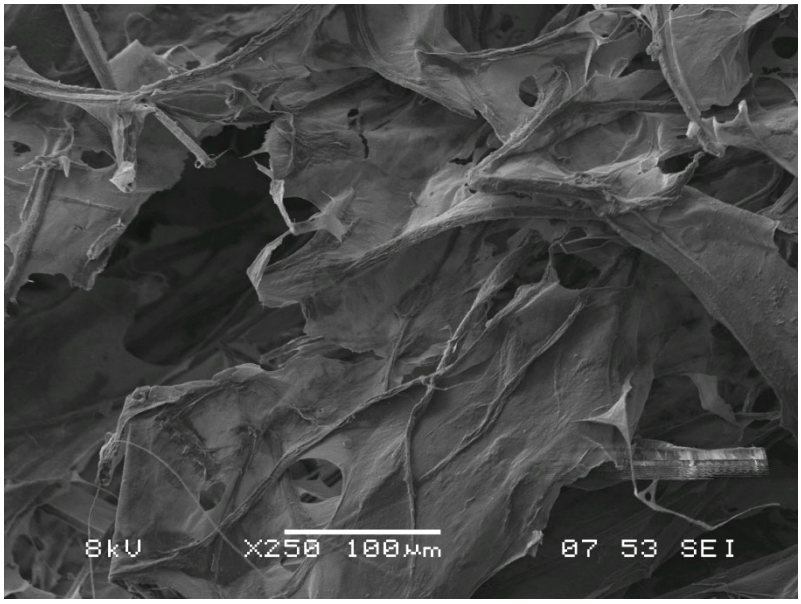

Figure S6.3 FESEM images of spinifex grass-derived nanocellulose sheets after freeze-drying.

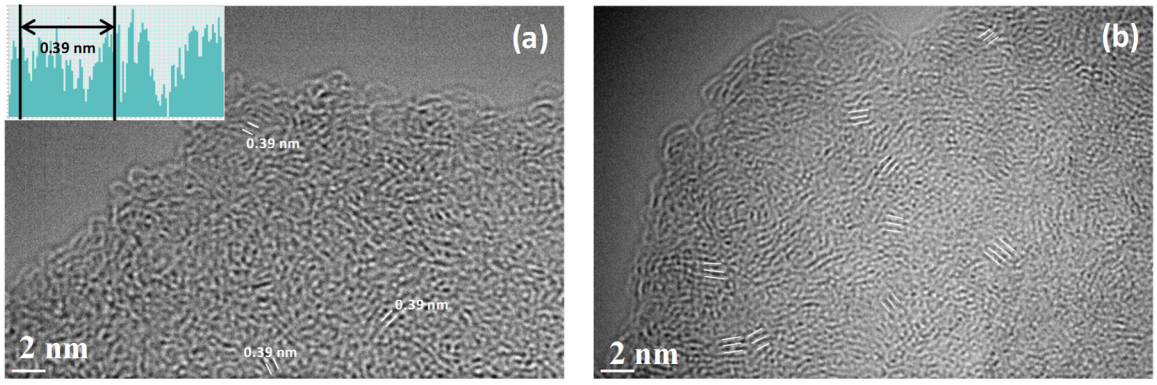

Figure S6.4 High-resolution TEM of NDC (inset: interlayer *d*-spacing of graphite (002) plane).

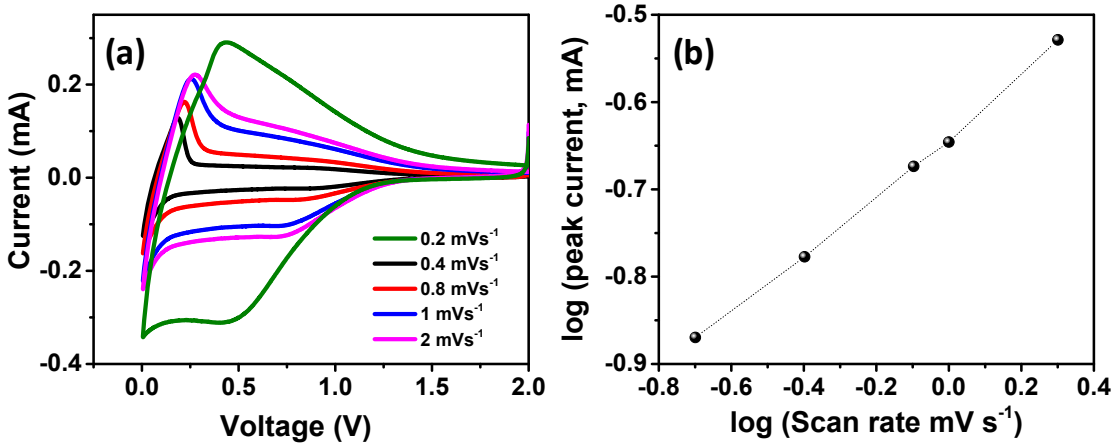

Figure S6.5 Kinetic analyses of NDC electrode tested against sodium: (a) CV cures at different scan rates and (b) log (scan rate)-log (peak current) profiles.

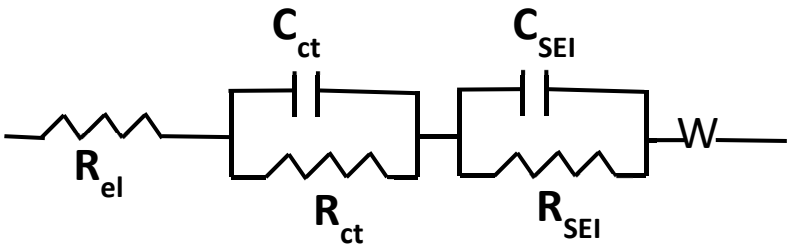

Figure S6.6 Equivalent circuits used to simulate the electrochemical impedance spectra results.

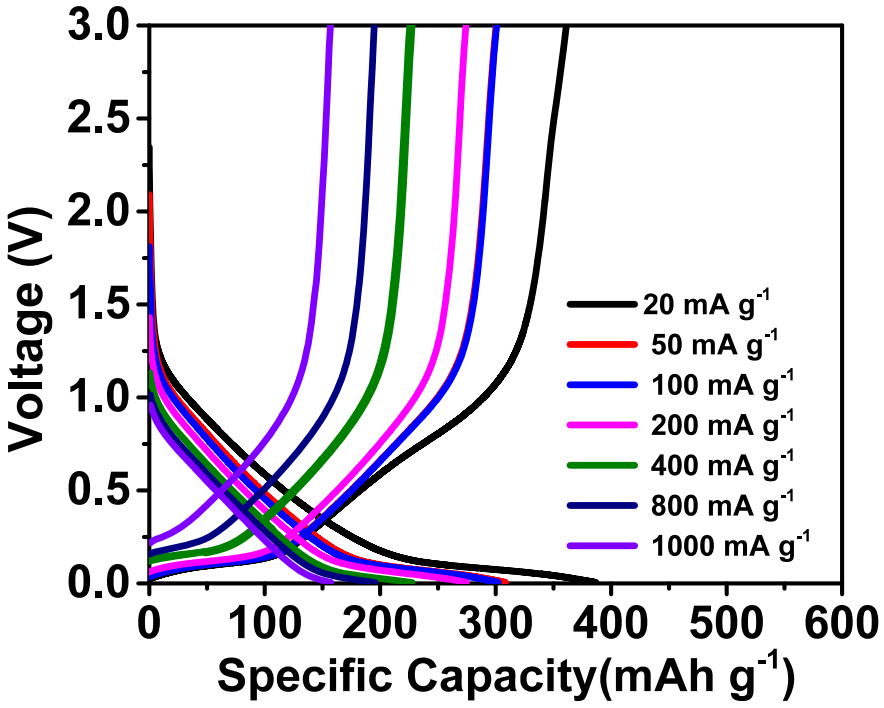

Figure S6.7 Charge-discharge curves at different rates for NDCs tested against sodium.

Chapter 7. Nitrogen-containing biomass-derived carbon for enhancing sodium-ion storage capacity

-Published as *R R Gaddam et al.* Capacitance-enhanced sodium-ion storage in nitrogen-rich hard carbon*, Journal of Materials Chemistry A*, 2017, 5, 22186-22192.

7.1 Introduction

Sodium-ion batteries (NIBs) are promising alternatives to the lithium-ion battery (LIB) technology because of sodium's natural abundance and low cost [1-3]. Graphite has been used successfully as an anode in LIBs, but is unfavourable for sodium-ion insertion due to the larger atomic radius of sodium than lithium (1.02 *vs.* 0.76 Å) [4-6]. However, hard carbon materials, have been shown to exhibit good sodium-storage performance due to the presence of turbostratic nanodomains [5]. Despite the availability of a range of hard carbon materials, high-capacity carbon anodes with good stability against cycling and high rate capability need to be developed.

From a molecular perspective, introducing heteroatoms into hard carbons can enable surface redox reactions, generate topological defects and form disordered carbon structures, thus, potentially enhancing sodium-ion storage capacity [7]. In particular, nitrogen doping can alter the electronic structure of hard carbons, due to the formation of different nitrogen species such as graphitic nitrogen (also referred to as quaternary nitrogen), pyridinic nitrogen, and pyrrolic nitrogen [8-10], and this may change the sodium-ion storage capabilities [11]. Previously, it has been demonstrated that nitrogen-doped carbon nanosheets with a high percentage of pyridinic groups (~46%) delivered a superior sodium-ion storage capacity [12]. Yan et al. [13] have observed that a hard carbon anode containing pyrrolic and graphitic nitrogen that was derived from biomass 'okara' exhibited a long life and high charging rates in NIBs. Recently, Wang et al. [11] reported a predominantly capacitive contribution controlled the processes in an anode material comprising nitrogen-rich graphene with pyridinic, pyrrolic and graphitic nitrogen groups. Despite the available reports detailing the performance of nitrogen-rich carbon materials for NIBs, further studies are required to analyse the origin of capacitive contribution, and the influence of nitrogen content on the enhanced electrochemical performance including cycle life.

In this work, a nitrogen-rich hard carbon (*N*-HCS) was prepared from biomass via a hydrothermal approach followed by low-temperature pyrolysis. As an anode for NIBs, the *N*-HCS delivered a specific discharge capacity of 520 mA h g^{-1} at 20 mA g^{-1}, with a long cycle-life. At a high current of 1 A g^{-1}, the electrode delivered a capacity of ~204 mA h g^{-1} after 1000 cycles. The experimental results suggested that the presence of nitrogen can significantly enhance the interaction between sodium ions and the hard carbon.

7.2 Experimental methods

7.2.1 Material synthesis

Dried raw mango powder obtained from an Asian store in Brisbane, Australia, was dissolved in 15 mL of dilute H_2SO_4 (Aldrich) while stirring at room temperature for 30 min. Here, the dilute sulphuric acid solution was prepared by mixing 5 mL of concentrated H_2SO_4 (AR, ≥ 98%, Sigma Aldrich) with 10 mL of distilled water. The mixture was hydrothermally treated in an autoclave at 170 ºC for 25 h. The product was separated, washed with water and ethanol, and freeze-dried overnight. The hard carbon sample that was obtained was then thermally treated at 900 ºC for 2 h in a nitrogen atmosphere. Subsequently, the sample was oxidised to introduce defects and oxygen-containing groups to the hard carbon as follows [14, 15]. Briefly, 400 mg of the as-prepared carbon was dissolved in a mixture of 25 mL sulphuric acid and 0.5 g sodium nitrate (≥ 99.0%, Sigma Aldrich) while it was stirred overnight. Then, 2 g of $KMnO_4$ (≥ 99.0%, Sigma Aldrich) was added, followed by dropwise addition of 150 mL of distilled water still while stirring overnight in an ice bath. Subsequently, hydrogen peroxide (30 % (w/w) in H_2O, Aldrich) was added into the above mixture until gas bubble evolution ceased. The solid was filtered off, washed with copious amount of water, ethanol and hydrochloric acid (reagent grade, 37%, Sigma Aldrich) and freeze-dried overnight to yield a sample designated as HCS. To introduce nitrogen functionalities including an amide group (denoted N-C=O), HCS was further treated with ethylenediamine (≥ 99%, Sigma Aldrich) in methanol at room temperature as reported previously [13, 16]. After washing with methanol, a nitrogen-rich sample, designated as *N*-HCS, was obtained.

7.2.2 Material characterization

X-Ray diffraction (XRD) was recorded on Bruker D8 Advance X-ray diffractometer with Ni-filtered Cu Kα radiation (λ = 1.54056 Å, 40 kV, 30 mA) at a scan rate of 2º min^{-1}. Nitrogen sorption isotherms were measured on a Tristar II 3020. All samples were degassed at 150 ºC for 6 h prior to the measurement. Transmission electron microscopy (TEM) measurements were carried out on a JEOL 2100 at an acceleration voltage of 200 kV. Field emission scanning electron microscope measurements were taken on JEOL 7001. X-ray photoelectron spectroscopy (XPS) spectra were acquired on a Kratos Axis ULTRA X-ray photoelectron spectrometer with a 165-mm hemispherical electron energy analyzer and a monochromatic Al Kα (1486.6 eV) radiation at 225 W (15 kV, 15 mA). Raman spectra were collected using a Raman Spectrometer (Renishaw) with a 514 nm laser.

7.2.3 Electrochemical testing

The working electrode was prepared by mixing 70% active material (HCS or *N*-HCS), 20% carbon black and 10% polyvinylidene fluoride (PVDF) in N-methyl pyrrolidone (NMP), which was coated onto a Cu-foil and then dried in a vacuum oven overnight at 60 ºC. The working electrode, glass fibre, electrolyte and Na metal counter electrode were assembled into a 2032-type coin cell filled in an Ar-filled glove box. 1 M $NaClO_4$ in an equal volume ratio of ethylene carbonate (EC) and propylene carbonate (PC) mixed with 0.3 wt% of fluoroethylene carbonate (FEC) was used as the electrolyte. Galvanostatic charge-discharge measurements were performed on a Neware battery tester CT3008. Electrochemical impedance spectroscopy (EIS) and cyclic voltammetry (CV) measurements were carried out on a CHI 660D electrochemical workstation.

7.3 Results and Discussion

The FESEM images of both HCS and *N*-HCS shown in **Figure 7.1** reveal a predominantly spherical morphology. The pre-treatment with sulphuric acid solution promoted the breakdown of the biomass into smaller molecules like monomeric sugars [17, 18]. The hydrothermal carbonisation treatment enabled these molecules to nucleate and grow to form spherical particles in order to minimize their surface energy [19]. The obtained sample was then annealed at 900 ºC in nitrogen atmosphere, followed by an oxidation step for introducing oxygen-containing groups, which are believed to be essential for introducing amide groups when treated with ethylenediamine. Further, smaller carbon particles alongside the larger spheres could be seen in the FESEM images (**Figure 7.1**). These smaller particles could be formed from the monomeric sugars that did not undergo transformation larger spheres.

The TEM images in **Figure S7.1** of the samples show a rougher surface morphology of HCS (**Figure S7.1**) as compared to that of *N*-HCS (**Figure 7.1c**). The high-resolution TEM images of *N*-HCS (**Figure 7.1d**) clearly display a graphitic microstructure along with turbostratic domains typically observed in hard carbons. A interlayer *d*-spacing of ~0.39 nm was obtained for *N*-HCS which is larger than that of natural graphite. Further, the scanning transmission electron microscope (STEM) images **(Figures 7.1e-h**) show the presence of carbon, nitrogen and oxygen well dispersed throughout the *N*-HCS. On the other hand, however, the absence of nitrogen was clearly observed for the sample HCS (**Figure S7.2**).

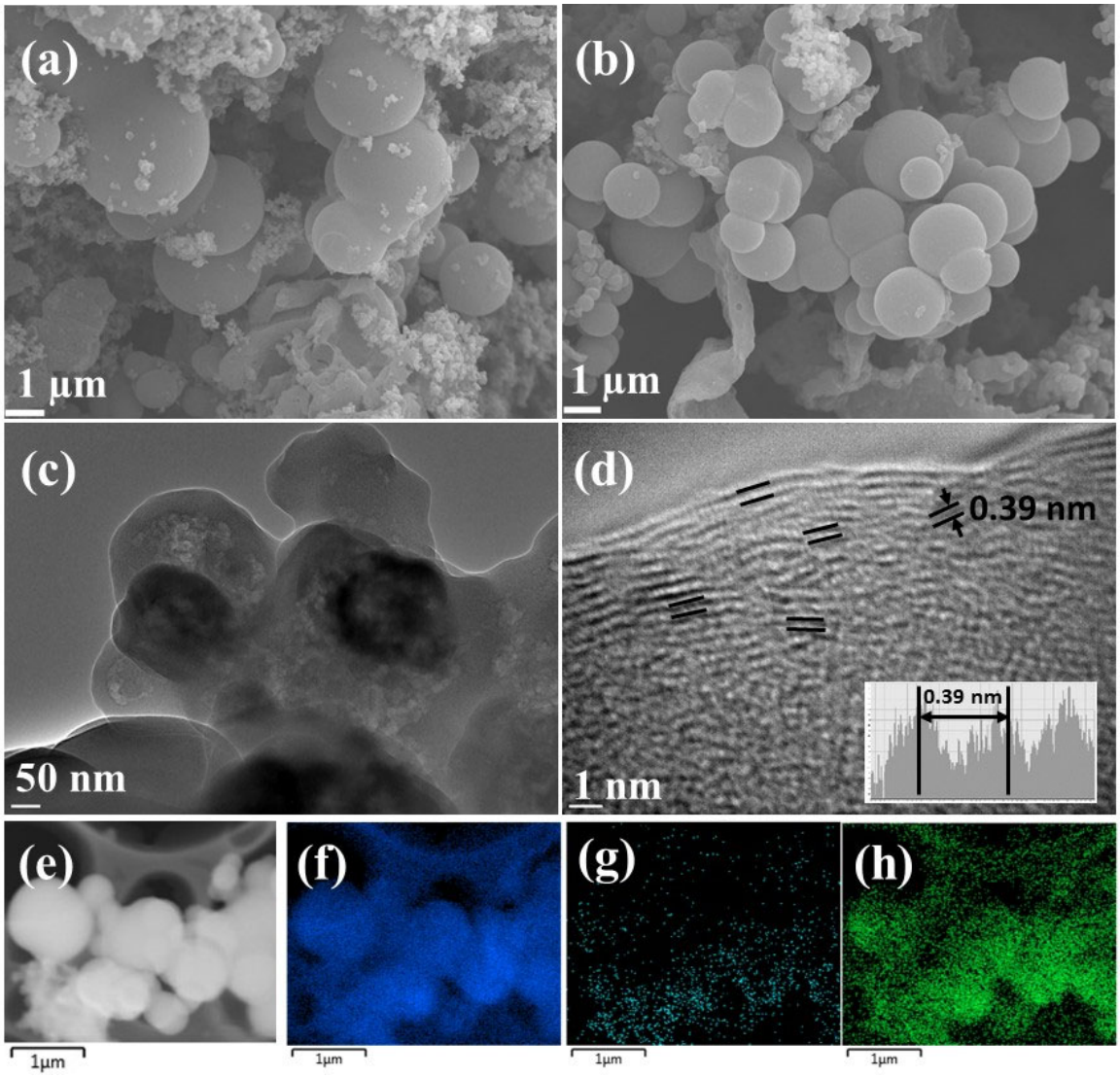

Figure 7.1 FESEM images of (a) HCS and (b) *N*-HCS. TEM images of (c) HCS and (d) *N*-HCS; (e) the Scanning transmission electron microscope (STEM) image of *N*-HCS. Energy dispersive X-ray elemental colour mapping images of (f) carbon, (g) nitrogen and (h) oxygen in *N*-HCS.

The X-ray diffraction (XRD) patterns of both samples exhibit two prominent peaks at ~22 and ~42 degrees two theta which can be attributed to the crystallographic planes of (002) and (100) of graphitic domains in the hard carbon (**Figure 7.2a**) [20]. Although no significant change in the peak patterns were observed after treatment with ethylenediamine, an increase in the *d*-spacing of *N*-HCS (d_{002} = 0.39 nm) compared to that of HCS (d_{002} = 0.37 nm) was noticed. The higher interlayer spacing in *N*-HCS could facilitate sodium-ion storage. The Raman spectra (**Figure 7.2b**) of both HCS and *N*-HCS display a prominent G peak around ~1610 cm^{-1} and a D-peak at ~1353 cm^{-1}. The G-peak (graphite band) corresponds to the first order scattering of the E2g vibration mode of sp^2 carbon atoms.[21] The D-peak (defect band) corresponds to

disorder in the A1g breathing mode of the six fold aromatic ring near the basal edge. The I_D/I_G intensity ratio of HCS and *N*-HCS are ~0.75 and ~0.86 respectively (**Table S7.1**). An increase in the peak intensity ratio of D to G band in the case of *N*-HCS is indicative of structural distortion induced by the presence of nitrogen and edge defects [22]. Further, nitrogen adsorption and desorption studies carried out (**Figure 7.2c**) indicated a specific surface area of ~16 m^2/g for *N*-HCS, whereas HCS exhibited a specific surface area of ~ 82 m^2/g. The decrease in surface area is probably due to the closer packing of carbons in case of *N*-HCS. Such observations of a reduction in surface area post ethylenediamine treatment have been observed previously [23]. The lower surface area could induce limited solid-electrolyte interphase formation, thereby enhance the coulombic efficiency and show better electrochemical performance [24].

The XPS spectra of HCS and *N*-HCS are shown in **Figure 7.2d**. *N*-HCS displayed a strong C1s signal at 284.6 eV together with an N1s signal at 401.3 eV and the O1s signal at 531 eV. A significant amount of nitrogen (9.06 at. %) could be observed in *N*-HCS. HCS contained 69.81 at. % of carbon and 30.19 at. % of oxygen. Typical high-resolution spectra of C1s and O1s in HCS are presented in **Figure 7.2e and 7.2f**. The C1s spectrum is deconvoluted into dominant components of C-C sp^2, C-COO, C-O-C, C=O and COO at 284.6, 285.5, 286.7, 288.20 and 288.93 eV respectively. Similarly, the O1s spectra can be deconvoluted to OH, O=C, O-C and adsorbed H_2O at 531.17, 531.8, 532.82 and 533.71 eV respectively [25, 26]. The C1s spectra of *N*-HCS (**Figure 7.2g**) reveal the presence of C-C (sp^2), C-C (sp^3), C-O-C/ C-OH, C-N, N-C=O and π-π* at binding energies of 284.6, 285.7, 286.5, 287.7, 288.7 and 290.04 eV respectively [25, 27]. The different chemical states of nitrogen are represented by deconvoluted peaks in the N1s high-resolution spectrum (**Figure 7.2h**) centred at 398.79 eV (pyridinic N, imine or amine labelled N-H in **Figure 7.2h**), 399.81 eV (amides labelled N-C=O in **Figure 7.2h**), 400.95 eV (pyrrolic N) and 401.76 (graphitic N) [23, 28-32]. The O 1s spectra of *N*-HCS (**Figure 7.2i**) comprise OH, N-C=O, C-O-C/C-OH and adsorbed H_2O at binding energies of 530.81, 531.8, 532.9 and 533.9 eV, respectively.

To understand the electrochemical properties of the as-prepared carbons, cyclic voltammetry (CV) studies were carried out at a scan rate of 0.1 mV s^{-1} in the voltage range of 0.005 to 3.0 V. The initial curve in the CV for both HCS and *N*-HCS are quite different from the subsequent curves (**Figure 7.3a and b**). In the first cycle, two prominent reduction peaks at 0.5 V and 0.9 V were observed for both the anodes, which in the subsequent cycles disappeared. These peaks are generally attributed to the degradation of electrolyte and the formation of solid electrolyte

interphase (SEI) on the surface of the electrode [22]. The SEI formation in the initial cycle along with other irreversible sodium-ion interaction with the anode contribute to the initial loss in capacity. The overlapping CV curve after the initial cycle is an indication of excellent stability and reversibility of sodium-ion storage in the as-prepared anode materials. In the low voltage region, the sharp cathodic peak near 0 V and the corresponding anodic peak near 0.2 V was observed. This resembles the CV curve witnessed for lithium-ion interaction with the graphite-based electrode [33]. In the wide potential range, the CV curve exhibits a rectangular shape indicating the existence of capacitive storage behaviour in both the carbons, which predominantly involve physical adsorption on the surface along with some redox reactions with a heteroatom containing functional groups and/or defect sites [34, 35].

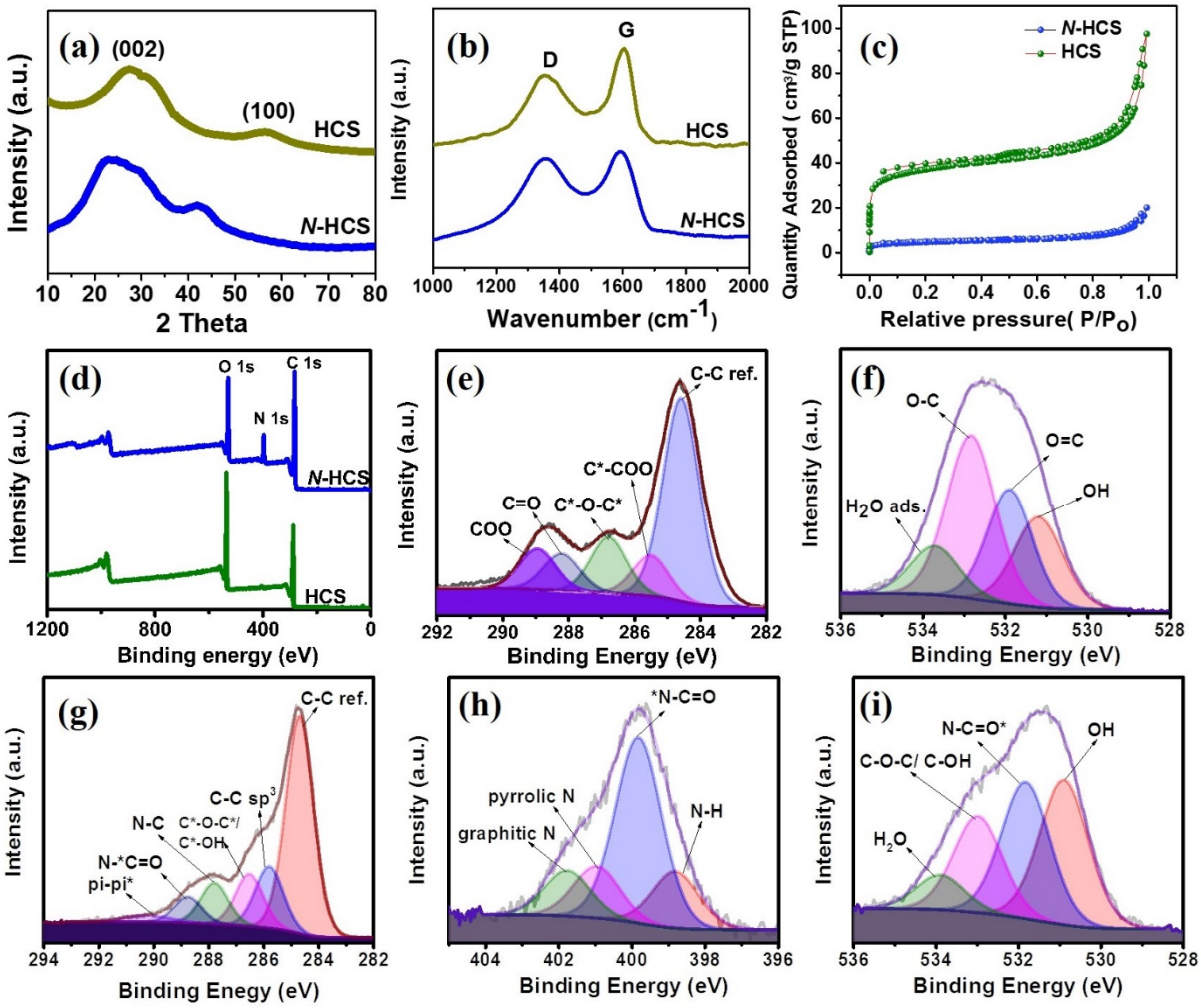

Figure 7.2 (a) XRD patterns, (b) Raman spectra, (c) nitrogen adsorption and desorption isotherms, and (d) XPS survey scans of HCS and *N*-HCS: C1s (e) and O1s (f) spectra of HCS, C1s (g), O1s (h) and N1s (i) spectra of *N*-HCS.

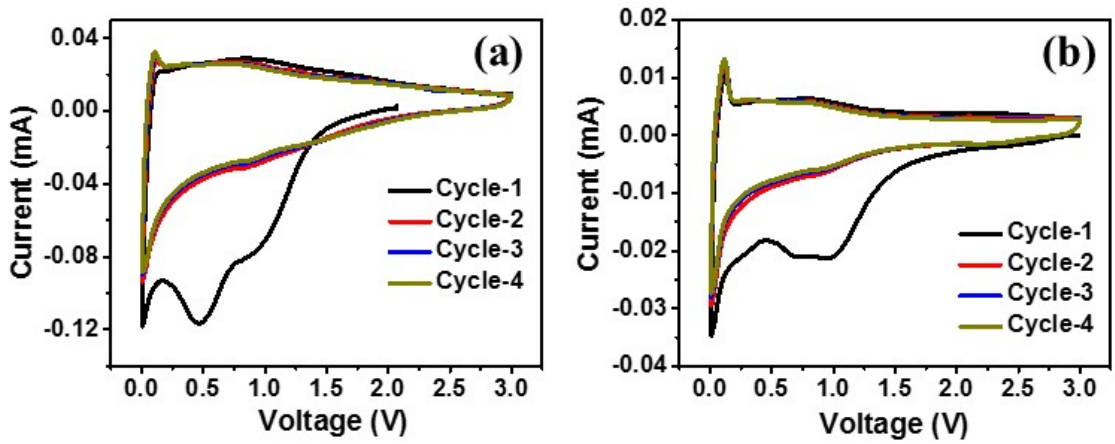

Figure 7.3 Cyclic voltammograms of (a) HCS and (b) *N*-HCS tested against sodium.

The cyclic voltammograms of HCS and *N*-HCS at different scan rates are shown in **Figures 7.4a and 7.4b**. To further determine the capacitive contribution of the carbon samples, we plot log (peak-current, i) against log (scan rate, v) based on the data in **Figures 7.4a and 7.4b**, and the results are given in **Figure 7.4c**. Data described by the equation $I = av^b$, with b value of 1 means an entirely capacitive controlled process, while with b value of 0.5 indicates a diffusion controlled process [36, 37]. Based on the CV curves taken at different rates, the data for *N*-HCS fits the equation with b = 0.79 (**Figure 7.4c**), suggesting the existence of a predominant capacitive contribution to the process. On the other hand, the data for HCS (**Figure 7.4c**), fits the equation with b = 0.23, which indicates a slow diffusion-controlled process [37].

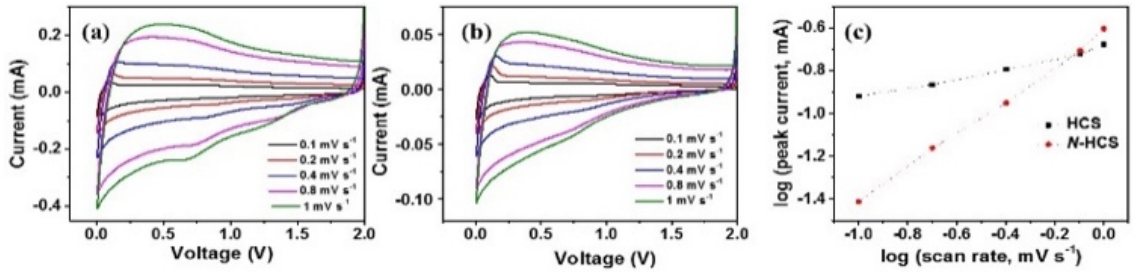

Figure 7.4 Kinetic analysis of electrode tested against sodium: (a, b) CV cures at different scan rates of HCS and *N*-HCS respectively and (c) log (scan rate)-log (peak current) profiles.

The performance of *N*-HCS was also evaluated using EIS before and after cycling. The Nyquist plot for each of the cells showed a semicircle with a large diameter at high frequencies and a straight line at the low-frequency region. The semicircle is related to the sodium-ion transport through the SEI film, and the straight line corresponds to the diffusion of sodium-ions in the active materials.[13] The impedance spectra were modelled with the equivalent circuit depicted

in the inset of **Figures 7.5a and b**. Here, R_{el} represents the electrolyte resistance, C_{ct} signifies the double layer capacitance; R_{ct} is the charge transfer resistance; Z_w is the Warburg element associated with ion diffusion in carbon electrode. The SEI formation at the electrode surface results in a resistance and a capacitance named as C_{SEI} and R_{SEI}, respectively. The numerical values obtained from modelling are provided in **Table S7.2**. The value of R_{ct} for HCS before cycling is 100 Ω and post-cycling it becomes 131.3 Ω. Likewise in the case of N-HCS, R_{ct} before cycling is 20 Ω and post-cycling it becomes 27 Ω. The charge-transfer resistance is much less in the case of *N*-HCS as compared to HCS. This indicates better electrode-electrolyte interactions in nitrogen-rich carbons, which also explains the stable cycling performance observed.

The galvanostatic charge-discharge studies of HCS and *N*-HCSs (**Figure 7.5c**) were carried out in the voltage domain of 0.005 to 3 V. *N*-HCS displayed a specific discharge capacity of 1164 mA h g^{-1} and a specific charge capacity of 445 mA h g^{-1} in the first cycle. The observed irreversible capacity in the first cycle is attributed to the formation of SEI along with irreversible reactions between sodium and surface functional group [22, 38]. The charge-discharge curves become more stable in the subsequent cycles and the Coulombic efficiency reach to near 100 %. The sloping curve observed in the charge-discharge curve is caused by the reversible insertion of sodium in the voids and vacancies present in the as-prepared carbon [39-41]. HCS show a specific discharge capacity of 1036 mA h g^{-1} and a specific charge capacity of 339 mA h g^{-1} in the first cycle. In the 2nd cycle, *N*-HCS and HCS delivered a specific discharge capacity of 520 and 380 mA h g^{-1}. *N*-HCS has more capacity retention than that of HCS. Similar to that observed for *N*-HCS the coulombic efficiency stabilises in the later cycles. The charge-discharge curves at various current densities from 20 to 1000 mA g^{-1} are provided in **Figure S7.3**. The near sloping lines with variable slope could arise from diffusion controlled and capacitive controlled charge storage mechanisms [42]. The shapes of the charge-discharge curve remained the same even when cycled at high current rates indicating the stability of the as-prepared hard carbons.

In addition to the high specific capacity, *N*-HCS displayed a superior rate capability with reversible specific charge capacities of 427, 308, 268, 238, 208, 172 and 162 mA h g^{-1} and discharge capacities of 520, 333, 277, 242, 209, 173 and 162 mA h g^{-1} at current densities of 20, 50, 100, 200, 400, 800 and 1000 mA g^{-1}, respectively (**Figure 7.5d**). A significant amount of specific capacity was still retained when the current density was reversed to 20 mA g^{-1}, representing a superior rate performance, unlike HCS. HCS, when tested against sodium,

demonstrated specific charge capacities of 313, 249, 221, 190, 153, 120 and 104 mAh g^{-1} and discharge capacities of 380, 256, 224, 191, 153, 120 and 104 mAh g^{-1} at current densities of 20, 50, 100, 200, 400, 800 and 1000 mA g^{-1}, respectively. The obtained rate performance was one of the best amongst the carbonaceous materials reported in the literature (**Table S7.3**) [7, 43-45]. The long-term cycling performance of HCS and *N*-HCS was evaluated at a current density of 1 A g-1 (**Figure 7.5e**). A specific capacity of 204 mA h g^{-1} was retained at the 1000^{th} cycle, indicating an excellent durability of *N*-HCS for NIBs. The HCS electrode, however, delivered a specific capacity of 113 mA h g^{-1} at the 1000^{th} cycle when cycled at the same current rate, showing the importance of the presence of nitrogen in capacitive energy storage. The superior performance of sample *N*-HCS can be attributed to the enhanced interlayer spacing, along with the presence of heteroatoms, particularly nitrogen atoms [34].

The mechanism of sodium-interaction with *N*-HCS was investigated using the ex-situ X-ray diffraction (Ex-XRD), ex-situ Raman spectroscopy and ex-situ TEM as represented in **Figures 7.6a-c**. For the all the ex-situ characterizations, the coin-cells were disassembled in a glovebox, washed with propylene carbonate, dried and tested immediately. Ex-XRD in **Figure 7.6a**, showed a completely amorphous profile for the as-prepared *N*-HCS electrode tested against sodium, without any distinct peaks when discharged and charged. The absence of peaks belonging to the crystallite phase indicates the formation of highly amorphous products and a chemically stable SEI [46]. Further, the ex-situ Raman spectroscopy (**Figure 7.6b**) of the fresh, the charged and discharged electrode indicated a progressively ordered structure during discharging and subsequent disorder during the reverse process [47].

Ex-situ TEM (**Figure 7.6c**) was further used to investigate the structural changes and the sodium storage mechanism in the *N*-HCS. Both the discharged and charged sample show no prominent increase in the *d*-spacing in comparison with the pristine sample, this indicates the absence of an obvious sodium-intercalation within the graphitic layers [24]. The progressive ordering and disordering in Raman could be due to sodium adsorption between graphite galleries, defect sites and voids. Therefore, from the ex-situ characterizations of the electrode, we observe that the sodium ion storage in the *N*-HCS carbon might involve sodium-adsorption on disordered graphene sheets along with those sites containing significant heteroatom content. Reported computational studies [48] have shown that the presence of amide containing functional groups in *N*-HCS is primarily responsible for the enhancement in sodium-ion storage.

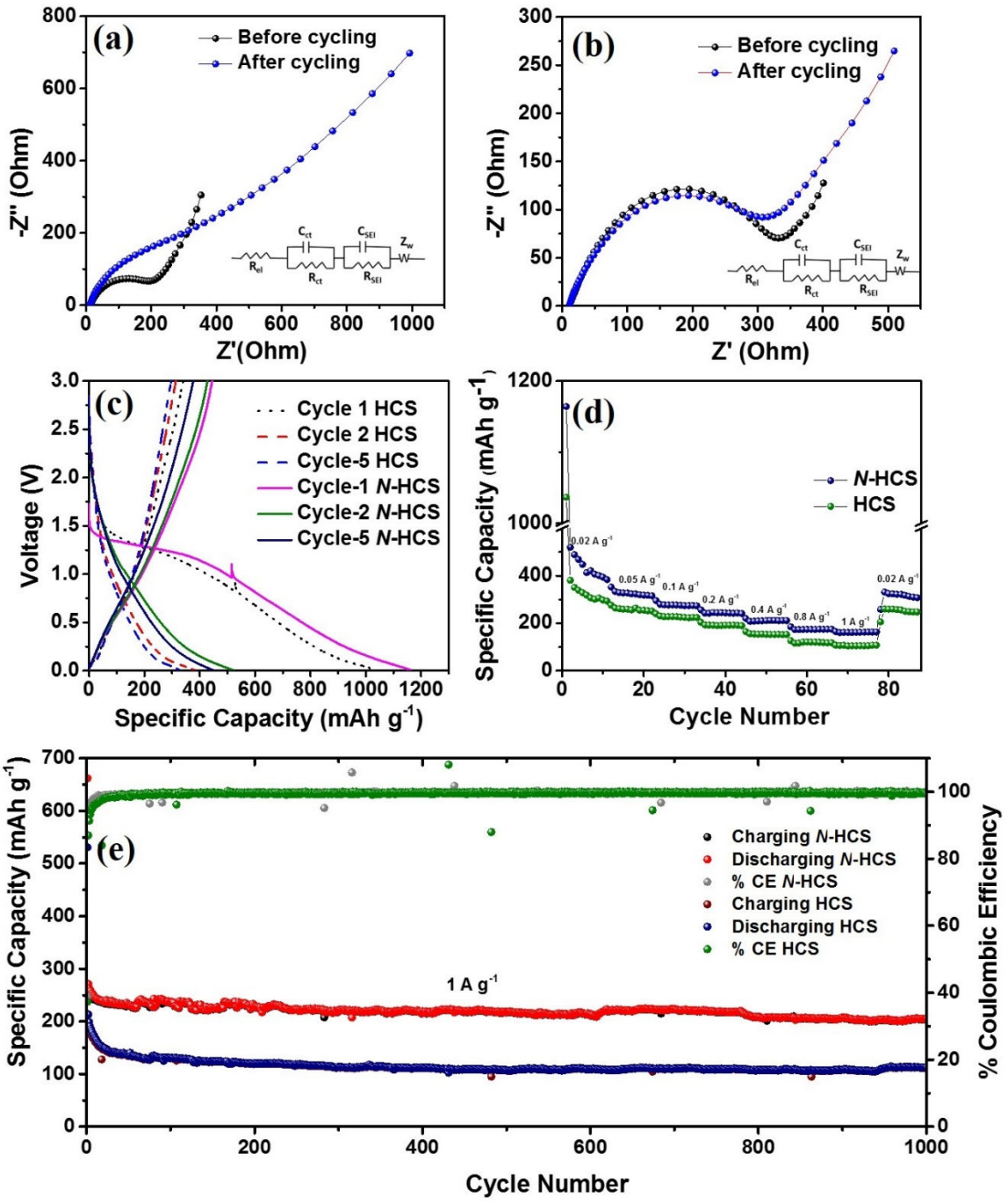

Figure 7.5 (a,b) EIS of HCS and *N*-HCS; (c) Galvanostatic charge/discharge curve, (d) rate capability and (e) cycling stability of *N*-HCS and HCS against Na/Na^+.

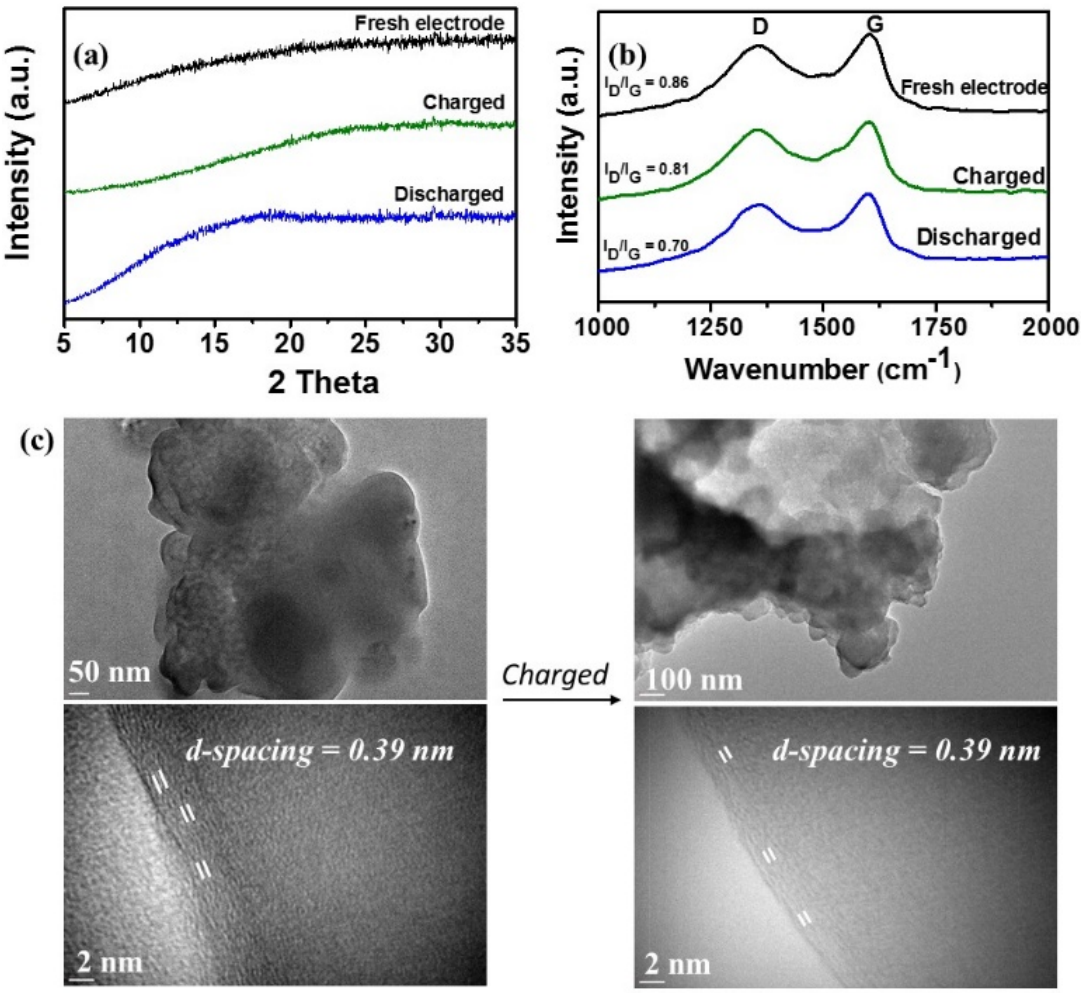

Figure 7.6 (a) Ex-situ XRD patterns and (b) ex-situ Raman spectra of N-HCS electrode before and after charging/discharging against sodium ions. (c) TEM images of discharged (left) and charged (right) *N*-HCS electrode.

7.4 Conclusions

A sodium-ion battery fabricated with nitrogen-rich hard carbon as anode exhibited an exceptional cycling stability, as well as a good capacity. The unprecedented performance of such a low-surface area nitrogen-rich hard carbon indicates that the presence of nitrogen and large interlayer spacing can boost the capacity through a predominantly ion-adsorption mechanism. Validating the above statement, hard carbon without nitrogen showed comparatively poor electrochemical performance when tested against sodium. The improved performance opens opportunities for nitrogen-rich hard carbon in other electrochemical energy storage devices.

7.5 References

[1] D. Kundu, E. Talaie, V. Duffort, L.F. Nazar, Angew. Chem. Int. Ed., 54 (2015) 3431-3448.

[2] M.S. Balogun, Y. Luo, W.T. Qiu, P. Liu, Y.X. Tong, Carbon, 98 (2016) 162-178.

[3] W. Luo, F. Shen, C. Bommier, H. Zhu, X. Ji, L. Hu, Acc. Chem. Res., 49 (2016) 231-240.

[4] N. Yabuuchi, K. Kubota, M. Dahbi, S. Komaba, Chem. Rev., 114 (2014) 11636-11682.

[5] M.-S. Balogun, Y. Luo, W. Qiu, P. Liu, Y. Tong, Carbon, 98 (2016) 162-178.

[6] A.H. Farokh Niaei, T. Hussain, M. Hankel, D.J. Searles, J. Power Sources, 343 (2017) 354-363.

[7] Z. Wang, L. Qie, L. Yuan, W. Zhang, X. Hu, Y. Huang, Carbon, 55 (2013) 328-334.

[8] D. Yan, C. Yu, X. Zhang, W. Qin, T. Lu, B. Hu, H. Li, L. Pan, Electrochim. Acta, 191 (2016) 385-391.

[9] M. Hankel, D.J. Searles, Phys. Chem. Chem. Phys., (2016).

[10] Y. Hu, X. Sun, Chemically Functionalized Graphene and Their Applications in Electrochemical Energy Conversion and Storage, Advances in Graphene Science, InTech, Rijeka, 2013, pp. Ch. 0.

[11] D. Li, L. Zhang, H. Chen, J. Wang, L.-X. Ding, S. Wang, P.J. Ashman, H. Wang, J. Mater. Chem. A, 4 (2016) 8630-8635.

[12] S. Vadahanambi, H.-H. Chun, K.H. Jung, H. Park, RSC Adv., 6 (2016) 38112-38116.

[13] T. Yang, T. Qian, M. Wang, X. Shen, N. Xu, Z. Sun, C. Yan, Adv. Mater., 28 (2016) 539-545.

[14] W.S. Hummers Jr, R.E. Offeman, J. Am. Chem. Soc., 80 (1958) 1339-1339.

[15] N.A. Kumar, H.-J. Choi, Y.R. Shin, D.W. Chang, L. Dai, J.-B. Baek, ACS Nano, 6 (2012) 1715-1723.

[16] N.H. Kim, T. Kuila, J.H. Lee, J. Mater. Chem. A, 1 (2013) 1349-1358.

[17] R. Katahira, J.B. Sluiter, D.J. Schell, M.F. Davis, J. Agric. Food. Chem., 61 (2013) 3286-3292.

[18] V.S. Chang, M.T. Holtzapple, Appl. Biochem. Biotechnol., 84 (2000) 5-37.

[19] M. Sevilla, A.B. Fuertes, Carbon, 47 (2009) 2281-2289.

[20] P. Sennu, V. Aravindan, M. Ganesan, Y.-G. Lee, Y.-S. Lee, ChemSusChem, 9 (2016) 849-854.

[21] N.R. Kim, Y.S. Yun, M.Y. Song, S.J. Hong, M. Kang, C. Leal, Y.W. Park, H.-J. Jin, ACS Appl. Mater. Inter., 8 (2016) 3175-3181.

[22] J. Xu, M. Wang, N.P. Wickramaratne, M. Jaroniec, S. Dou, L. Dai, Adv. Mater., 27 (2015) 2042-2048.

[23] N. Cai, P. Larese-Casanova, J. Environ. Chem. Eng., 4 (2016) 2941-2951.

[24] Y. Li, Y.-S. Hu, M.-M. Titirici, L. Chen, X. Huang, Adv. Energy Mater., 6 (2016) 1600659.

[25] B. Yao, C. Li, J. Ma, G. Shi, Physical Chemistry Chemical Physics, 17 (2015) 19538-19545.

[26] R.R. Gaddam, E. Jiang, N. Amiralian, P.K. Annamalai, D.J. Martin, N.A. Kumar, X.S. Zhao, Sustainable Energy & Fuels, 1 (2017) 1090-1097.

[27] N.A. Kumar, R.R. Gaddam, M. Suresh, S.R. Varanasi, D. Yang, S.K. Bhatia, X.S. Zhao, J. Mater. Chem. A, 5 (2017) 13204-13211.

[28] L. Tang, R. Ji, X. Li, K.S. Teng, S.P. Lau, J. Mater. Chem. C, 1 (2013) 4908-4915.

[29] X. Wang, C.-G. Liu, D. Neff, P.F. Fulvio, R.T. Mayes, A. Zhamu, Q. Fang, G. Chen, H.M. Meyer, B.Z. Jang, S. Dai, J. Mater. Chem. A, 1 (2013) 7920-7926.

[30] N. Daems, X. Sheng, I.F.J. Vankelecom, P.P. Pescarmona, J. Mater. Chem. A, 2 (2014) 4085-4110.

[31] G. Beamson, D. Briggs, High resolution XPS of organic polymers, Wiley1992.

[32] K. Artyushkova, D. Habel-Rodriguez, T.S. Olson, P. Atanassov, J. Power Sources, 226 (2013) 112-121.

[33] Y. Cao, L. Xiao, X. Ai, H. Yang, Electrochem. Solid-State Lett., 6 (2003) A30-A33.

[34] N.A. Kumar, R.R. Gaddam, S.R. Varanasi, D. Yang, S.K. Bhatia, X.S. Zhao, Electrochim. Acta, 214 (2016) 319-325.

[35] H.L. Wang, W.H. Yu, J. Shi, N. Mao, S.G. Chen, W. Liu, Electrochim. Acta, 188 (2016) 103-110.

[36] D. Xu, C. Chen, J. Xie, B. Zhang, L. Miao, J. Cai, Y. Huang, L. Zhang, Adv. Energy Mater., 6 (2016) 1501929.

[37] V. Augustyn, J. Come, M.A. Lowe, J.W. Kim, P.-L. Taberna, S.H. Tolbert, H.D. Abruña, P. Simon, B. Dunn, Nat. Mater., 12 (2013) 518-522.

[38] L. Fu, K. Tang, K. Song, P.A. van Aken, Y. Yu, J. Maier, Nanoscale, 6 (2014) 1384-1389.

[39] P. Thomas, D. Billaud, Electrochim. Acta, 47 (2002) 3303-3307.

[40] H. Pan, Y.-S. Hu, L. Chen, Energy Environ. Sci., 6 (2013) 2338-2360.

[41] D.A. Stevens, J.R. Dahn, J. Electrochem. Soc., 148 (2001) A803.

[42] S. Li, J. Qiu, C. Lai, M. Ling, H. Zhao, S. Zhang, Nano Energy, 12 (2015) 224-230.

[43] H.g. Wang, Z. Wu, F.l. Meng, D.l. Ma, X.l. Huang, L.m. Wang, X.b. Zhang, ChemSusChem, 6 (2013) 56-60.

[44] H. Liu, M. Jia, N. Sun, B. Cao, R. Chen, Q. Zhu, F. Wu, N. Qiao, B. Xu, ACS Appl. Mater. Inter., 7 (2015) 27124-27130.

[45] L.L. Tian, S.B. Li, M.J. Zhang, S.K. Li, L.P. Lin, J.X. Zheng, Q.C. Zhuang, K. Amine, F. Pan, ACS Appl. Mater. Inter., 8 (2016) 26722-26729.

[46] J. Xu, I.-Y. Jeon, J. Ma, Y. Dou, S.-J. Kim, J.-M. Seo, H. Liu, S. Dou, J.-B. Baek, L. Dai, Nano Res., (2017) 1-14.

[47] E.M. Lotfabad, J. Ding, K. Cui, A. Kohandehghan, W.P. Kalisvaart, M. Hazelton, D. Mitlin, ACS Nano, 8 (2014) 7115-7129.

[48] R.R. Gaddam, A.H.F. Niaei, Marlies Henkel, Debra Searles, N.A. Kumar and X.S. Zhao, J. Mater. Chem. A, 5 (2017) 22186-22192.

7.6 Supplementary information

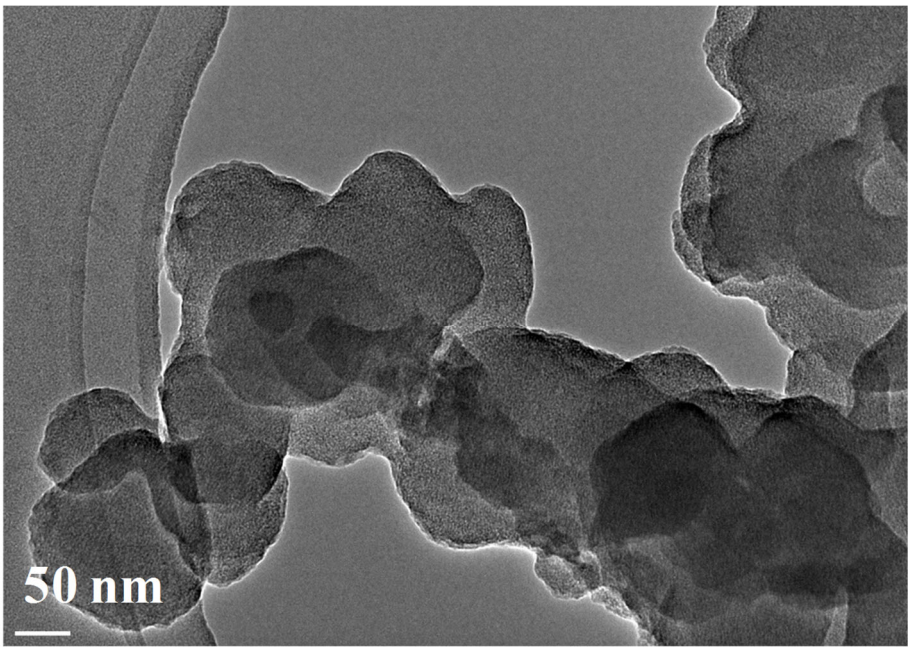

Figure S7.1 Transmission electron microscope image of HCS.

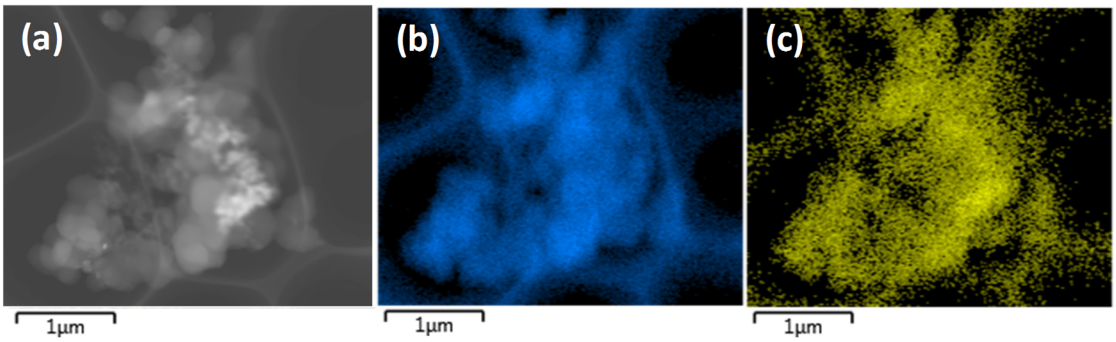

Figure S7.2 Energy dispersive X-ray mapping of HCS: (a) electron image, (b) carbon, and (c) oxygen.

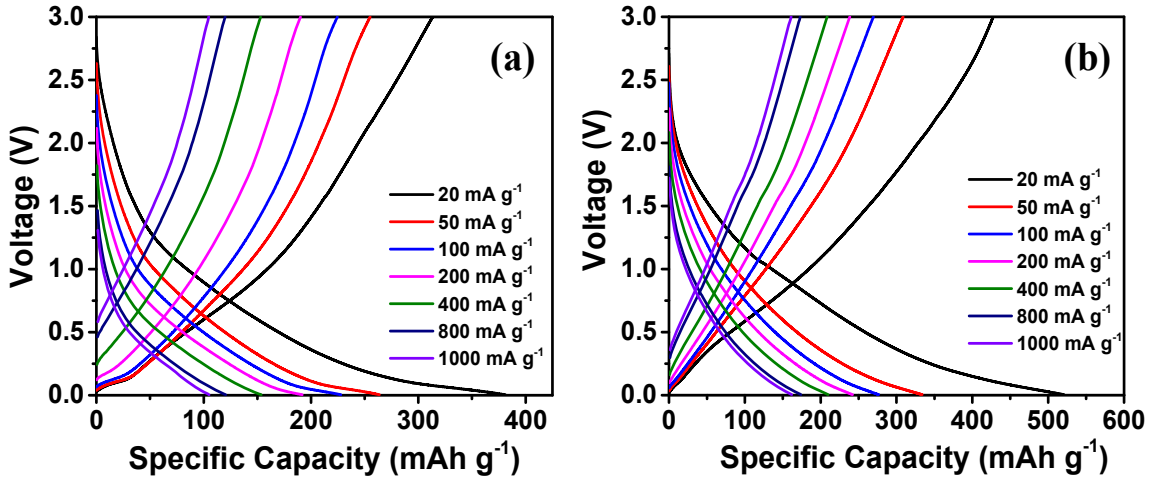

Figure S7.3 Charge-discharge curves at different rates for (a) HCS and (b) *N*-HCS tested against sodium.

Table S7.1 Physical and chemical properties of HCS and *N*-HCS

Sample	BET surface area (m^2/g)	Pore volume (cm^3/g)	Elemental composition (at. %)	*d*-spacing	I_D/I_G ratio
HCS	82	0.04	C (69.81), O (30.19)	0.37 nm	0.75
N-HCS	16	0.03	C (72.77), N (9.06), O (18.17)	0.39 nm	0.86

Table S7.2 Kinetic parameters obtained from equivalent circuit fittings of the experimental data for samples HCS and *N*-HCS before and after 5 cycles.

Sample	R_{el} **(Ω)**	R_{ct} **(Ω)**
HCS (before cycling)	14.46	100.5
HCS (after 5 cycles)	10.04	131.3
N-HCS (before cycling)	12.30	20.78
N-HCS (after 5 cycles)	13.40	27.96

Table S7.3 A comparison of the N-rich carbon with those reported in the literature for sodium-ion batteries

Material	Synthesis method	Potential Range (V)	Capacity (mA h g^{-1})	Cycling stability	Rate capability	Ref.
N-HCS	Hydrothermal synthesis followed by pyrolysis	0.005 – 3	520 at 20 mA g^{-1}	~204 mAhg^{-1} obtained after 1000 cycles at 1 A g^{-1}	333 mA h g^{-1} at 0.05 A g^{-1} 277 mA h g^{-1} at 1 A g^{-1}	This work
Nitrogen rich porous carbon	Pyrolysis in Ar atmosphere	0.01 - 3	335 at 100 mA g^{-1}	~130 mA h g^{-1} at 5 A g^{-1} after 1000 cycles was obtained.	256 mA h g^{-1} at 0.2 A g^{-1} 213 mA h g^{-1} at 1 A g^{-1}	[1]
Nitrogen-rich bamboo-like carbon	Pyrolysis in Ar atmosphere	0.01 - 3	270 at 50 mA g^{-1}	Lower than 120 mA h g^{-1} at 0.5 A g^{-1} after 160 cycles was obtained.	167 mA h g^{-1} at 0.1 A g^{-1} 138 mA h g^{-1} at 0.2 A g^{-1}	[2]
Nitrogen-doped carbon/graphene hybrid	Pyrolysis in N_2 atmosphere between 700-800 °C	0.01 - 3	303 at 50 mA g^{-1}	~270 mA h g^{-1} at 50 mA g^{-1} after 200 cycles was obtained.	207 mA h g^{-1} at 1 A g^{-1} 177 mA h g^{-1} at 2 A g^{-1}	[3]
Nitrogen-rich mesoporous carbon	Pyrolysis in N_2 atmosphere at 700 °C	0.01 - 3	338 at 30 mA g^{-1}	~252 mA h g^{-1} at 50 mA g^{-1} after 100 cycles was obtained.	86 mA h g^{-1} at 1 A g^{-1} 48.9 mA h g^{-1} at 2 A g^{-1}	[4]
N-doped porous carbon	KOH activation followed by Pyrolysis in N_2 atmosphere	0.01 – 2.5	274 at 25 mA g^{-1}	Good cycling stability for 100 cycles was observed with 88% capacity retention	58 mA h g^{-1} at 2 A g^{-1} 37 mA h g^{-1} at 4 A g^{-1}	[5]
Nitrogen doped holey carbon nano-sheets	KOH activation followed by Pyrolysis in N_2 atmosphere	0.01 - 3	323 at 100 mA g^{-1}	~80 mA h g^{-1} at 1 A g^{-1} after 400 cycles was obtained.	194 mA h g^{-1} at 0.2 A g^{-1} 139 mA h g^{-1} at 0.5 A g^{-1}	[6]
Nitrogen-doped carbon nanofiber films	Heating in vacuum followed by carbonising in Ar atmosphere	0.01 - 3	377 at 100 mA g^{-1}	~210 mA h g^{-1} at 5 A g^{-1} after 7000 cycles was obtained.	315 mA h g^{-1} at 0.5 A g^{-1} 154 mA h g^{-1} at 15 A g^{-1}	[7]
Nitrogen-doped carbon nanofibers	Pyrolysis in N_2 atmosphere at 600 °C	0.01 - 2	150 at 200 mA g^{-1}	~134 mA h g^{-1} at 0.2 A g^{-1} after 200 cycles was obtained.	139 mA h g^{-1} at 0.5 A g^{-1} 132 mA h g^{-1} at 1 A g^{-1}	[8]

Nitrogen-doped carbon microspheres	Hydrothermal synthesis followed by thermal treatment	0.005 – 3	336 at 50 mA g^{-1}	~104 mA h g^{-1} at 10 A g^{-1} after 12500 cycles was obtained.	148 mA h g^{-1} at 5 A g^{-1} 132 mA h g^{-1} at 1 A g^{-1}	[9]
Nitrogen-doped carbon sheets	Hydrothermal treatment followed by pyrolysis	0.01 – 2	315 at 0.15 C	~247 mA h g^{-1} at 0.3 C after 50 cycles was obtained.	ca.100 mA h g^{-1} at 3 C 32.3 mA h g^{-1} at 30 C	[10]

References

[1] L. Wang, C. Yang, S. Dou, S. Wang, J. Zhang, X. Gao, J. Ma, Y. Yu, Electrochim. Acta, 219 (2016) 592-603.

[2] D. Li, L. Zhang, H. Chen, L.X. Ding, S. Wang, H. Wang, Chem. Comm., 51 (2015) 16045-16048.

[3] H. Liu, M. Jia, B. Cao, R. Chen, X. Lv, R. Tang, F. Wu, B. Xu, J. Power Sources, 319 (2016) 195-201.

[4] H. Liu, M. Jia, N. Sun, B. Cao, R. Chen, Q. Zhu, F. Wu, N. Qiao, B. Xu, ACS Appl. Mater. Inter., 7 (2015) 27124-27130.

[5] V. Selvamani, R. Ravikumar, V. Suryanarayanan, D. Velayutham, S. Gopukumar, Electrochim. Acta, 190 (2016) 337-345.

[6] H.G. Wang, Z. Wu, F.l. Meng, D.l. Ma, X.l. Huang, L.M. Wang, X.B. Zhang, ChemSusChem, 6 (2013) 56-60.

[7] S.Q. Wang, L. Xia, L. Yu, L. Zhang, H.H. Wang, X.W. Lou, Adv. Energy Mater., 6 (2016) 1502217.

[8] Z. Wang, L. Qie, L. Yuan, W. Zhang, X. Hu, Y. Huang, Carbon, 55 (2013) 328-334.

[9] D. Yan, C.Y. Yu, X.J. Zhang, W. Qin, T. Lu, B.W. Hu, H.L. Li, L.K. Pan, Electrochim. Acta, 191 (2016) 385-391.

[10] T. Yang, T. Qian, M. Wang, X. Shen, N. Xu, Z. Sun, C. Yan, Adv. Mater., 28 (2016) 539-545.

Chapter 8. Conclusions and recommendations for future work

8.1 Conclusions

This thesis project has successfully utilised biomass as a promising source for hard carbon production for use as high-performance anodes for both lithium-ion and sodium-ion batteries. Also, such carbon materials derived from biomass have shown to possess larger interplanar spacing along with defects that allow efficient intercalation and adsorption of sodium-ions. The electrochemical performance of such biomass-derived carbons as anodes for sodium-ion batteries (NIB), observed from the works presented in this thesis exhibit a performance on par with that of commercial lithium-ion batteries (LIB) based on graphite anodes. In all, the thesis concludes that hard carbons obtained from biomass is a suitable anode for both LIBs and NIBs, and are quite promising to commercialise NIB. Specifically,

In chapter 4, a novel flame deposition approach to produce highly mono-disperse carbon material with superior performance as anodes in both NIBs and LIBs was successfully demonstrated. The electrode showed a cycle discharge capacity of ~277 $mAhg^{-1}$ in NIB and of about 741 $mAhg^{-1}$ in LIB at 100 mAg^{-1} current density. The stable electrochemical performance with good cycling stability and rate tolerance could be observed for both LIBs and NIBs. From this work it was seen that effect of carboxyl groups on the carbon nanoparticles was more pronounced for LIBs than that for NIBs. Overall, this chapter studied the importance of such nanostructured carbon materials for NIBs.

In chapter 5, a similar flame deposition method using camphor as a precursor was used. In this chapter, a one-step electrode preparation protocol was developed. A binder free and conductive additive free carbon nanoparticles were deposited onto nickel foam which served as an anode. The absence of binder could reduce the cost of the electrode while providing superior electrochemical performance. The electrode showed superior electrochemical performance for both LIBs and NIBs. Such design strategies and the use of nanostructured carbon material could inspire the future design for rechargeable batteries.

In chapter 6, a widely available spinifex grass was used as a precursor material. From the spinifex nanocellulose, hard carbons were synthesised using pyrolysis approach. This hard carbon showed superior cycling stability and high rate performance. This is attributed to the nanovoids and turbostratic nanodomains present in the as-prepared hard carbon. A specific capacity of ~300 mAh g^{-1} was obtained for over 400 cycles. Such a synthesis strategy for carbon materials shows promise for large-scale production and application as a high-performance anode for NIBs.

In chapter 7, the possibility to further improve the performance of such hard carbon materials was investigated. Enriching the carbon with nitrogen was considered, which in turn promoted superior electrochemical performance as compared to the hard carbon without nitrogen. The nitrogen-rich hard carbons contained a significant amount of amide functional groups which was responsible for better sodium-ion storage which is reflected in the battery's superior cycling and rate performance. Therefore, the work successfully investigated the effect of nitrogen enrichment on the performance of hard carbon materials.

8.2 Challenges and future perspectives

The performance of anodes is still a bottleneck for NIB commercialisation. Hard carbons from biomass though promising still face some challenges with large-scale production. In addition, the microstructure of such hard carbon materials varies depending on the synthesis protocol, treatment methods and the type of precursor used. Therefore, proper selection and identification of precursor are quite important. In case of carbon materials some principal challenges of controlling the microstructure, enhancing the energy density by using dopants, large-scale chemical/physical manipulation of biomass and developed nanofabrication techniques need be overcome to address the present-day energy challenges.

It is to be noted that biomass-derived carbon materials have not yet been able to reach the industrial standards, therefore further research should be devoted to developing biomass-derived carbon materials of industrial standards [1]. Generally, carbon materials are known for their high electrical conductivity, surface area and corrosion resistance for which they find a wide range of applications. Especially in NIBs, the effect of various parameters in synthesis and post-synthesis that affect the electrochemical performance is not fully understood. For instance, from the research work showcased in the thesis, it could be seen that nitrogen doping in the carbon does affect the performance and some investigations have been made in regard to this. However further investigations in more real-time battery applications need to be considered.

Also, another possible research direction would be to use a different kind of solvent for the electrolytes and study their performance. Researchers have shown that electrolyte affects the performance of the battery [2]. However, the exact mechanism of sodium-ion interaction with the hard carbon in different solvents has not yet been fully demystified. Further studies related to such mechanisms will provide insights on the way material design and electrolyte design need to be made. Yet another direction for research would be to abstain from using organic

solvents and shift to a safer aqueous electrolyte for NIBs. However, even in this case, there are voltage and performance limitations that need to be considered. Overall, the challenge of finding an appropriate precursor for hard carbon with a good electrolyte composition by understanding the underlying mechanism of sodium-ion storage in such a system will need to be addressed through future research.

8.3 References

[1] J. Górka, C. Vix-Guterl, C. Matei Ghimbeu, C, 2 (2016) 24.

[2] A. Ponrouch, D. Monti, A. Boschin, B. Steen, P. Johansson, M.R. Palacín, J. Mater. Chem. A, 3 (2015) 22-42.